



**HAL**  
open science

# Nanoporous alumina : electrokinetic properties and polyelectrolyte adsorption

Ali Vakilinejad

► **To cite this version:**

Ali Vakilinejad. Nanoporous alumina : electrokinetic properties and polyelectrolyte adsorption. Material chemistry. Sorbonne Université, 2023. English. NNT : 2023SORUS414 . tel-04391200

**HAL Id: tel-04391200**

**<https://theses.hal.science/tel-04391200>**

Submitted on 12 Jan 2024

**HAL** is a multi-disciplinary open access archive for the deposit and dissemination of scientific research documents, whether they are published or not. The documents may come from teaching and research institutions in France or abroad, or from public or private research centers.

L'archive ouverte pluridisciplinaire **HAL**, est destinée au dépôt et à la diffusion de documents scientifiques de niveau recherche, publiés ou non, émanant des établissements d'enseignement et de recherche français ou étrangers, des laboratoires publics ou privés.



# Sorbonne Université

École doctorale de Chimie Physique et Chimie Analytique de Paris Centre (ED-388)  
Laboratoire Physicochimie des Electrolytes et Nanosystèmes Interfaciaux

## **Nanoporous alumina : Electrokinetic properties and polyelectrolyte adsorption**

Ali VAKILINEJAD

Directrice de thèse : Emmanuelle DUBOIS

Soutenance le 4 Octobre 2023 devant un jury composé de:

Prof. Bruno LARTIGES (Université de Toulouse) ..... Rapporteur  
Dr. Jérôme COMBET (Institut Charles Sadron, Strasbourg) ..... Rapporteur  
Dr. Jérôme DUVAL (Université de Lorraine) ..... Examineur  
Prof. Alexa COURTY (Sorbonne Université) ..... Examinatrice  
Dr. Nicolas JOUAULT (Sorbonne Université) ..... Co-encadrement de thèse  
Dr. Emmanuelle DUBOIS (Sorbonne Université) ..... Directrice de thèse

## Acknowledgement

I am sincerely grateful to my supervisors, Dr. Emmanuelle and Dr. Nicolas Jouault for donating this valuable opportunity to me to conduct this thesis research work under their valuable supervision. Definitely, this thesis would not be accomplished without their assistance and continuous help. In particular, I would like to thank Dr. Nicolas Jouault for standing beside me and backing me up throughout my thesis from all scientific and technical aspects and even helping me with administrative works. I truly owe him the majority of my success in this work and words are not adequate to express my full gratitude to him. Emmanuelle's maternal kindness along with her seriousness taught me many valuable concepts that propelled me in my work and I will remember them throughout my life.

I would like to express my sincere thanks to Dr. Laurent Michot, the director of the Physicochimie des Electrolytes et Nanosystèmes interfaciaux (PHENIX) laboratory for approving my admission for this thesis work and giving me the opportunity to work in this reputation laboratory. Furthermore, another special thank is expressed to him along with Dr. Marie Jardat for joining the supervision team and supporting me not only scientifically, but also mentally and emotionally when the work was facing obstacles. I sincerely appreciate their commitment to my success in this work.

I treasure Prof. Bruno Lartiges and Dr. Jérôme Combet for accepting to report on my thesis. Besides, I express my sincere gratitude to Dr. Jérôme Duval and Prof. Alexa Courty both for being members of my thesis follow up committee and their acceptance to be members of jury. I really appreciate the feedbacks that I received during my committees from these two recent persons.

My recognition goes to Dr. Didier Lairez for building up the house-made streaming potential setup and also his commitment to stay beside us for operating the setup, troubleshooting and also developing the interface software.

I truly appreciate Mr. David Monetro's help in SEM imaging and EDX characterization. I am really thankful to him for his nice commitment to obtain accurate images and analysis of the samples and also providing me with the data files without any delay. His valuable instruction on operating the SEM microscope is unforgettable.

Hereby I express my sincere thanks to Dr. Clément GUIBERT from the Laboratoire de Réactivité de Surface (LRS), Sorbonne University for instructing me on the tangential flow commercial setup. His collaboration in data treatment is also appreciated.

I am thankful to many of my colleagues at the PHENIX laboratory whose presence made this journey easier. I would like to thank Ms. Amandine Anfray for her support in the laboratory with providing the chemicals and also calibrating the measurement instruments. Mr. Gerard Guillard is highly appreciated for managing the administrative works and conference registration and trip efficiently. Mr. Jose Gomez is appreciated for his cooperation to build the pieces needed for the instruments. My officemate Ph.D. candidates Mr. Maxime Labat, Mr. Maxime Sorriaux and Ms. Anne-Heloise Folgadam, master interns Ms. Cholë Le Bruchec and Mr. James Durandisse are appreciated for the nice friendship that they maintained with me. I wish them all the best in their thesis work and also their lives. Maxime Labat is thanked in particular for nicely talking to me in French. His presence helped me a lot in making progress in French language. Mr. Jacques Fries and Mr. Felicien Pauly had also very nice contribution in this part. Although as an Iranian my mother tongue is Persian (Farsi), I learnt Arabic by myself due to my own interest. For this, I sincerely appreciate my dear colleagues Ms. Sarrah Mezdari and Lydia Hamitouch for keeping talking to me in Arabic. The closure sense due to knowing a language together in common gave me the sense that we are compatriots. Dr. Kyle Reeves is also thanked for being in the lab and I always enjoyed talking to him and listening to his valuable advices and his beautiful American accent of English. I hereby thank all my dear colleagues in the PHENIX lab and I assert that I will never forget any of them even slightly.

My family has been always my most valuable possession in my life. I really cannot appreciate my father Prof. G. Reza Vakili-Nezhaad (spelling the last name different than me in his publications) in a way that he truly deserves for dedicating whole his life to the success of his children. He was my first professor and supervisor in life and also in academia. It was really heartwarming to me to have his valuable advices in the daily life and also in the academic area where he is a recognized specialist. My mother and my sister Goli are highly recognized for their love and support.

I would like to thank twin brother Mohammad my first and best friend in my life in particular. He came to France and finished his PhD thesis work before me and was a real point of reliance for me along with his wife, my dear sister in law Dr. Malihe Vaezalaei in a way that I never felt alone due to their presence in France. Malihe's sister, Kimia, is appreciated for her help in drawing the sketches of the manuscript. My dear Iranian friends Dr. Saman Vafadar, Dr. Mahammadreza Mosaferi and Dr.

Erfan Asgari are truly appreciated for their presence beside me and supporting me like their own brother. I express my sincere gratitudes to my dear friend Mr. AmirHossein Zeraati Aliabadi who always supported me with his true friendship and made the tough days of write-up nicer by moving to Paris to continue his PhD thesis. My dear friend Dr. Saeed Sadeghi Arjmand is particularly acknowledged for the sincere friendship that he donated to me since before my thesis. I was continuously learning diverse concepts from our conversations since he is truly one of the best mathematicians that I have met so far. I wish him all the best throughout his professional and personal life.

At last but not at least, I would like to sincerely appreciate Dr. Naoufal Bahlawane who supervised my master 2 internship at Luxembourg Institute of Science and Technology (LIST). I will never ever forget his nice support during my internship and the process of applying for my thesis. I wish him all the best of luck in his career and life.

My most special appreciation comes at last point and is expressed to my beloved fiancée, Hasti. She completely changed my life by entering it in the second half of my thesis. The indescribable love, beauty and calmness that she donated to my life facilitated triumphing over all difficulties and obstacles. Hasti released me from all ambiguities. May God keep our destinies coincident for good.

Once again, I sincerely appreciate all people who had contribution to my success in my thesis work.

# Contents

1	Chapter 1: Synthesis and characterization of nanoporous anodic aluminum oxide membranes...	6
1.1	Introduction.....	6
1.2	State of the art of the AAO membranes: synthesis, morphology and composition.....	6
1.3	Synthesis procedure.....	16
1.3.1	Electropolishing.....	16
1.3.2	Two-step anodization.....	17
1.3.3	Detachment of AAO from the aluminum substrate.....	20
1.4	Characterization of the anodic aluminum oxide membranes.....	25
1.4.1.1	Sulfur content in the third layer.....	29
1.4.1.2	Anions incorporation in the 2 <sup>nd</sup> and 3 <sup>rd</sup> layer.....	29
1.4.1.3	Dissolution time of the 3 <sup>rd</sup> layer.....	30
1.4.2	Characterization of through-hole AAOs: influence of the different experimental parameters.....	32
1.4.2.1	Structural characterization of through-hole AAOs.....	32
1.4.2.2	Elemental characterization of through-hole AAOs.....	36
1.5	Conclusions.....	42
2	Chapter 2: Electrical surface properties of nanoporous alumina membranes.....	44
2.1	Introduction.....	44
2.2	State of the art of the surface charge studies of the AAO membranes.....	44
2.3	Streaming potential (SP) and streaming current (SC) experiments.....	47
2.4	Electrophoretic mobility (EM) experiments.....	60
2.5	The aims of the current research work.....	60
2.6	Electrical surface properties of AAO membranes.....	61
2.6.1	IEPs of the different probed surfaces: outer, pore wall and ground surfaces.....	61
2.6.2	Influence of the amount and nature of “contaminants” within AAOs.....	63
2.7	Effect of buffers on the electrical surface properties of AAO membranes.....	67
2.8	Influence of nanochannel curvature.....	69
2.9	The case of EM.....	70
2.10	How can we reconcile the tangential and transverse results?.....	72
2.11	Conclusions.....	76

3 Chapter 3: The Behavior of Polyelectrolyte Chains Under Confinement in the Nanochannels of AAO membranes .....	78
3.1 Introduction.....	78
3.2 State of the art of the polyelectrolyte macromolecules inside nanoporous media.....	78
3.3 Methods to monitor the polyelectrolyte diffusion in AAO nanochannels .....	82
3.3.1 In situ monitoring.....	82
3.3.2 <i>Ex situ</i> monitoring.....	86
3.4 The in-situ experiments with styrene sulfonate monomers inside the nanochannels of the AAO membranes .....	87
3.5 Results and discussion.....	88
3.5.1 The diffusion rate and kinetics of adsorption .....	88
3.5.1.1 Effect of AAO thickness .....	89
3.5.1.2 Effect of PE concentration .....	94
3.5.1.3 Effect of ionic strength .....	97
3.5.1.4 Effect of pH.....	105
3.6 In-Situ and Ex-Situ measurements.....	110
3.7 Strength of the interactions between the NaPSS macromolecules and the AAO nanochannel surface.....	113
3.8 The nature of the interactions between the NaPSS Macromolecules and AAO nanochannels surface.....	118
3.9 Coverage of the nanochannels with small monomers .....	121
3.10 Conclusion.....	124
<b>General conclusions.....</b>	<b>126</b>
Appendix .....	130
References .....	141

## Introduction

Interfaces between two phases are very often governing the properties of the materials, especially in nanomaterials, for which the ratio of the surface over the volume is high. Among nanomaterials, the nanoporous ones, with pores in the range 1-100 nm, have attracted much attention from researchers since decades in numerous fields such as reactions catalysis, adsorption, phase separation and many other applications. A very interesting system is the nanoporous anodic alumina oxide (nAAO), already used for applications, as filtration membranes, confining medium, sensors or templates. As many questions are still open on this porous alumina, many academic studies are nevertheless still performed. Moreover, due to the tunability of their geometry, they can be considered as model porous systems. Indeed, they are produced as thin films that become membranes if detached from the substrate and consist of parallel nanochannels perpendicular to the surface of the membrane, which are ordered and not inter-connected. The geometric parameters of the channels can be tuned by the conditions used during the preparation process. In an aqueous based electrolyte, the oxide surface is charged, the sign and value of this charge depending on the ions nature and concentration.

These nAAO are thus nice systems to look at the confinement of species, the size of which is of the order of the channels, such as polymer. Such a confining medium can change their structure and their dynamics, therefore impacting their properties compared with the bulk situation. Although of wide interest in many questions as filtration, sequencing DNA, sensors..., the case of charged polymers, i.e. polyelectrolytes, has been seldom addressed. As polyelectrolytes bear charges on each monomer or part of the monomers, their behaviour depends on the concentration and nature of charged species inside the medium. The interaction of polyelectrolytes and nAAO can thus be impacted by the size of the nanochannel as well as by the charges on the walls of these nanochannels.

If the system is nice in principle, its practical study is rather difficult due to the orders of magnitude. Indeed, the membranes are typically 20-40 micrometers thick, with a porosity from 5 to 35%. Therefore, the total surface of the channels is around few  $\text{m}^2/\text{g}$  and the volume of the pores in one  $\text{cm}^2$  of membrane is between 0.1 and 1 microliter. The amount of polymer inside the pores and/or on the walls is therefore very small, which govern the choice of the techniques to analyse such systems.

The study of nAAO itself is therefore already challenging. A previous study at PHENIX focused on the empty AAO matrix to better understand its structure and composition before trying to insert polymers. Coupling several techniques, mainly Scanning Electron Microscopy, Small Angle Neutron Scattering and flow measurements through the membranes, a precise knowledge of the nAAOs was obtained. When the membrane was dipped into a polyelectrolyte solution, it was proven that the polymer entered the channels and adsorbs on the walls by combining Small Angle Neutron Scattering and Neutron reflectivity. Such measurements are however technically difficult and necessitate a large scale facility. Streaming potential was tested and appeared to be an accessible laboratory technique to study the adsorption and kinetics of a species inside these channels as the total amount of matter is not a limitation. A single pore can indeed be probed by streaming potential. This technique was used here with the aim to study the adsorption of polyelectrolytes in nAAOs under different conditions of confinement and interactions, modulated with the pH and ionic concentration.

The present manuscript is divided in three chapters. The first one focuses on the preparation of the nAAOs and on the determination of their characteristics. Different synthesis conditions are used which allow tuning the diameter of the pores, the distance between pores, the thickness of the nAAO, the composition in the walls and the porosity. The detachment from the film to obtain a membrane is analysed and the obtained membrane are then studied by Scanning Electron Microscopy, Energy Dispersive X-ray Spectroscopy and Infra Red Spectroscopy. This first step is crucial in order to know and tune the confining medium. Chapter 2 then deals with the charge properties of the membranes studied by electrokinetic techniques, which are also essential to know before introducing polymer inside the nanochannels. The values of the point of zero charge from literature are scattered and the values determined for the different types of surfaces have never been measured on the same membranes to our knowledge. There is thus no possible comparison although these two types of surfaces can differ, in particular due to the inhomogeneity of the composition of the porous matrix. Here the charge of the pore walls is studied by transverse streaming potential while the charge of the external surfaces of the membranes is studied by tangential streaming potential. The internal walls are also studied after grinding of the material to better understand the results by streaming potential and compare to literature. In Chapter 3, the membranes are in contact with a polyelectrolyte, here sodium polystyrenesulfonate, a strong polyelectrolyte that has been widely studied in literature and is therefore well known. Its interaction with the nanochannels is analysed mainly by transverse streaming potential, which enables following the kinetic of the process. Different types of membranes are used to understand the origin of the adsorption, and the parameters that influence its kinetics.

## List of Abbreviations

nAAO – Nanoporous Anodic Aluminium Oxide

SEM – Scanning Electron Microscope

EDX – Energy Dispersive X-Ray spectroscopy

FTIR – Fourier Transform Infrared spectroscopy

EDL – Electrical double layer

SE – Streaming experiments

SP – Streaming potential

SC – Streaming current

EM – Electrophoretic mobility

IEP – Isoelectric point

PZC – Point of zero charge

NaPSS – Sodium polystyrene sulphonate

PE – Polyelectrolyte

# 1 Chapter 1: Synthesis and characterization of nanoporous anodic aluminum oxide membranes

## 1.1 Introduction

In this chapter, we will describe the electrochemical synthesis and characterization of open-through nanoporous anodic aluminum oxide (AAO) membranes. Variable characteristic sizes and composition can be obtained by the modulation of several synthesis parameters and we will present the dependence of the morphological and compositional features of the AAO membranes on these synthesis parameters.

## 1.2 State of the art of the AAO membranes: synthesis, morphology and composition

Nanoporous anodic aluminum oxide (AAO) are alumina ( $\text{Al}_2\text{O}_3$ ) membranes made of parallel, non-connected and well-ordered nanochannels. In Figure 1-1, a scheme of the AAO membrane is depicted with the most important structural features: pores diameter ( $D_p$ ), nanochannel length which is also the membrane thickness ( $L_p$ ), interpore distance ( $D_{int}$ ) and pore ordering, i.e. the spatial pore arrangement. By looking at the membrane from the top surface, the porosity is defined as the ratio of the pores entrance surface (gray circles) to the total surface of the membrane. All these structural features are tunable by the modulation of the different experimental parameters during the synthesis and it has been of great importance to understand which experimental parameters control the morphological and surface properties of the AAO membranes in order to make them suitable for the different desired applications such as chemical sensing [1], biosensing [2], drug delivery [3]–[5], liquid crystal display (LCD) screens [6], ultrasonic transducing [7] and also protecting the metal surface against corrosion [8].

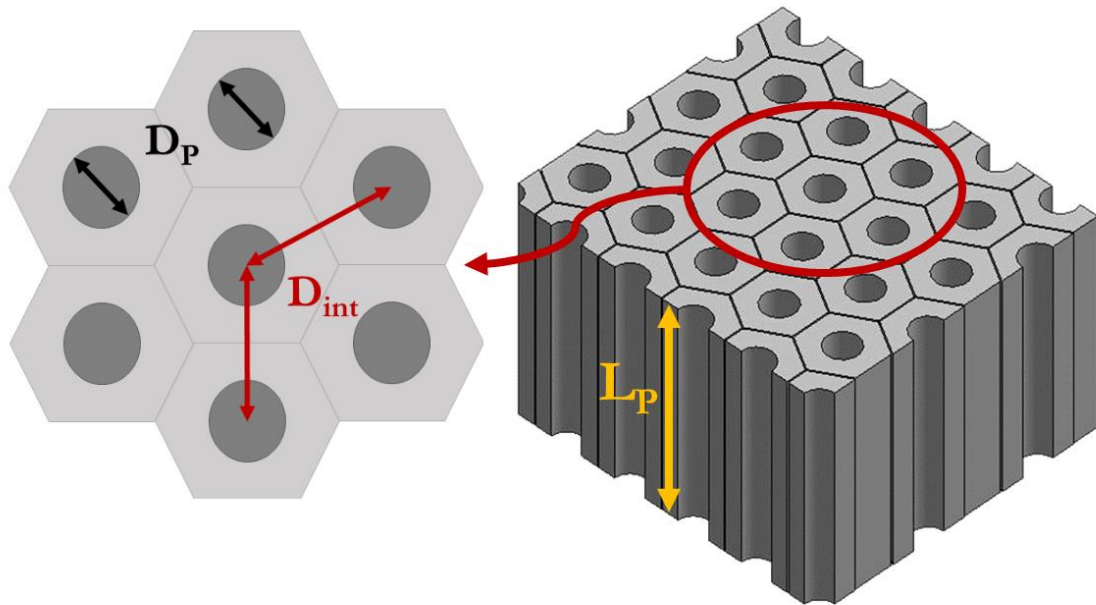


**Figure 1-1** Schematic figure of the AAO membrane with the morphological variables.

AAO are synthesized by an anodization process that convert a metal into a porous oxide by applying a constant voltage between this metal (here Al which plays the role of an anode) and an inert metal (here platinum which plays the role of the cathode) in various acidic solution; the most common being oxalic acid (OA). Many other types of acids have been used for anodizing the aluminum for synthesizing AAO such as sulfuric acid [9]–[11], selenic acid [12]–[14], phosphoric acid [15] and phosphonic acid [16].

During anodization, the oxidation reaction occurs on the aluminum surface which acts as the anode in the cell. The electrical current that passes through the circuit as a result of aluminum oxidation is measured. For studying the anodization reactions quantitatively, current density parameter ( $j$  [ $\text{mA}/\text{cm}^2$ ]) is considered which is the ratio of the electrical current to the surface of the aluminum immersed in the solution and exposed to oxidation reaction.

In the anodization process, the most important parameters that affect the physical properties of the synthesized AAO are the acid solution type, acid concentration, the anodization voltage which is maintained by a direct current (DC) voltage generator and the anodization temperature which is

maintained by a thermal liquid jacket circulation around the anodization cell. Among the vast literature on the AAO synthesis, the work of Masuda and Fukuda in 1995 was a breakthrough to produce well-ordered parallel nanochannels by introducing the two-step anodization [17], [18]. A first anodization is performed to produce porous alumina that will be subsequently dissolved. Only the imprints of the dissolved pores remain on the Al from which a second anodization will be carried out. The existence of the imprints drives the formation of well-ordered nanochannels. Then, in the recent decades, many researchers have made vast endeavors to find out the relation between these parameters and the morphological parameters of the AAO membranes. Based on the magnitude of the current density, the anodization process is classified in two categories of mild anodization (MA) and hard anodization (HA). It is worthy to mention that the criterion distinguishing MA from HA is the current density  $j$ : for MA in OA  $j$  is around  $5 \text{ mA}\cdot\text{cm}^{-2}$  at 40 V while it's around  $30 - 250 \text{ mA}\cdot\text{cm}^{-2}$  for HA at 110 – 150 V). Some researchers also have used accelerated mild anodization (AMA) in oxalic acid which is an intermediate between MA and HA for anodization. In this method, the current density magnitude falls in between HA and MA (for example  $20 \text{ mA}\cdot\text{cm}^{-2}$ ) which makes the rate of production of AAO higher than in MA and also prevents the breakdown of electrical current compared to HA where the electrical field through the AAO barrier layer exceeds the dielectric strength of the AAO due to high voltage, and the electrical current passes directly through AAO and increases sharply.

Inter-pore distance of the membranes is found to change linearly with the anodization voltage [19]–[22] and it is also found to be independent on the other variables like the temperature and the duration of anodization [22]. But, an optimal temperature gradient can lead to better arrangement of the nanochannels without affecting the interpore distance [23]. The pore diameter is also of a great importance which might depend on the pH of the electrolyte anodization solution [24] and increases with anodization potential in a specific acid solution [21], [22], [25] and decreases with the acid concentration [21]. Another parameter affecting  $D_p$  is the time that the membrane passes in the etching solution [26]: the longer the time, the higher the diameter. Inter-pore  $D_{int}$  and the pore diameter  $D_p$  influence directly on the porosity of the membrane. After discussing the factors affecting the  $D_{int}$  in AAO membranes, it is worthy to mention the reasons for which it has always been interesting to researchers to tune the morphological properties of anodic aluminum oxide membranes. The porosity of the AAO membrane can change with the  $D_{int}$ . And the porosity affects the optical properties of the AAO membrane such as reflectance [27], [28] birefringence [29] and also dielectric functions [30].

In some cases, researchers have realized that by mixing two sorts of acids and changing the molar ratio of these two acids along with the anodization voltage, the  $D_{int}$  can be tuned ranging from 100 to 750 nm [31].

Now it can be beneficial to survey the effect of the different acids most commonly used namely oxalic, sulfuric and selenic acid. For the case of the most well-known acid for the aluminum anodization which is oxalic acid, a wide range of anodization parameters have been changed. For examples, in case of using the oxalic acid, by staying in mild anodization (MA) and utilizing the voltage 40 V, the  $D_{int}$  was reported to be around 100 nm while in the same research work it is reported to change from 220 to 300 nm by changing the anodization voltage from 120 to 150 V which is in the range of hard anodization (HA) [20]. The  $D_{int}$  that they obtained were 90 – 130 nm for the voltage ranges of 35 to 50V [32]. In brief words, the  $D_{int}$  that has been reported for the AAO membranes synthesized by MA ranges from 30 nm (low voltages oxalic acid) up to 500 nm in case of anodization with phosphoric acid with anodization voltages 160 – 195 V [24], [33] and this characteristic depends mainly on the anodization voltage and increases linearly with this voltage and can increase by the viscosity of the electrolyte solution as well [34]. The interpore distance for the case of using selenic acid for MA is reported to be approximately 110 nm in the voltages 46 to 48 V [12], [14]. In brief words, the  $D_{int}$  increases linearly with voltage and the slope of this linearity is 2.5 in mild anodization for oxalic, sulfuric, phosphoric and selenic acid but this slope is not valid in hard anodization and becomes lower [35].

The current density  $j$  is also an important parameter and its evolution with time provides information about the AAO formation. An example of current density versus time curve is shown in Figure 1-2 for the first and second anodization in 0.3 M sulfuric acid solution at a constant voltage of 25 V. The different regions of the 1<sup>st</sup> anodization curve of this figure can be explained as follows [36],[37].

**(I)** At the very beginning, a sharp decrease is observed in the current. At this step, a very thin layer of alumina is formed on the surface of aluminum and this thin layer decreases the conductivity of aluminum. The concavities that exist on the surface of the aluminum because of roughness, give raise to the electrical current at some points.

**(II)** After the formation of thin alumina layer on the surface, the oxide formation in the roughness concavities continues. According to the work of Cheng and Ngan [38] the electrical field gradient is

concentrated in concavities. Thus, due to a higher electrical field gradient in the concave regions, the oxide is formed with a higher rate in these regions compared to the flat regions and the pores start to form in concavities. The small concavities continue to penetrate into aluminum and form pore channels. Since the roughness of the surface is random, the roughness concavities are randomly distributed on the aluminum surface. Hence, the geometry of these pores is not governed by the anodization parameters such as the voltage. By virtue of the electrical field gradient at the bottom of these concavities that penetrate into the aluminum, the driving force for the ions is supplied to migrate from the electrolyte solution/oxide interface through the oxide formed in segment **I**. Consequently, an increase in the electrical current is observed because of the oxidation reactions.

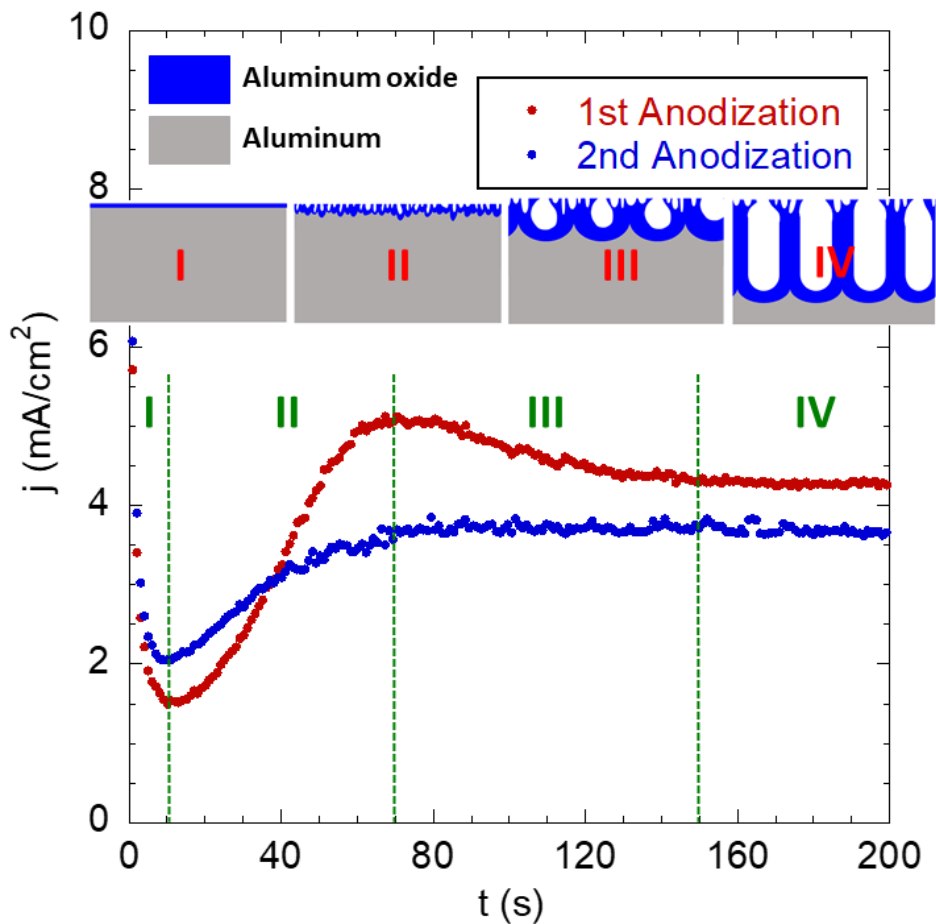


**Figure 1-2** Different sections of the 1<sup>st</sup> anodization current measurement curve and comparison with the 2<sup>nd</sup> anodization. Anodization of the membrane SA(0.3)-12<sup>1</sup> at temperature 18 °C.

(III) By increasing the anodization time, the bottoms of the deeper pores formed in segment II grow faster than the surrounding pores and their bottom parts grow on the horizontal direction as well. At some point, the shape of the growing pores becomes like a water drop with wide bottom and small top opening. The electric field grows the pores and adjusts their thickness seeking field distribution uniformity within the oxide barrier layer. The ions migrate through the oxide barrier layer because of the electric field and the oxidation reactions continue. Electric field distribution for ions migration through the alumina is innate. Hence, the field distribution within the barrier layers that have different thicknesses because of different anodization voltages is similar. Accordingly, we have different pore

<sup>1</sup> In assigning codes to the membranes, we have the following rule:

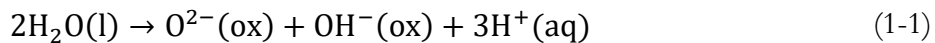
**Acid abbreviation (Acid concentration in mol/L)-number of the membrane synthesized in the specific acid**  
 The abbreviations of the acids that we used in our studies are OA for the oxalic acid, SA for the sulfuric acid and SeA for the selenic acid solution. For example, OA(0.3)-1 denotes the membrane number one that has been synthesized in the oxalic acid with the concentration 0.3M.

distributions in different voltages. The electric field controls the geometry of the pores bottoms and their penetration into aluminum for maintaining the field distribution uniformity within the barrier layer. At some point, the bottom surface of the pores reaches a maximum and intersects with the growing bottom of the pores in surroundings. When the contact surface between the oxide layer and the aluminum is maximized, a peak is observed in the electrical current. Since in the second anodization the pores imprint already exist on the aluminum surface, this peak is not observed.

**(IV)** Afterwards, the pore walls start to form and the walls elongate. Due to the increase of the length, there will be a sharp decrease in the electric field in the direction of the pores wall growth. According to this fact, the main site of the oxide formation remains on the bottom of the pores at the barrier layer. By penetration of the pore into the aluminum and the growth of the walls, the drop like shape of the pore changes to U-shape. By commence and continue of this step, the geometry of the pores bottoms equilibrates and a decrease is observed in the current density in the j-t curve. The processes taking place in the four time segments of the j-t curve are depicted schematically in Figure 1-2.

So far, many theories and models have been proposed and developed to explain the formation of self-ordered AAO. Besides, many reviews have been done on this wide bibliography. In a book published by Losic et al [36], a review was done on the different mechanism proposed which were clearly explained and gathered together from our point of view. It is endeavored to describe the mechanism at this step using the mechanisms proposed in the literature. In the steady state of oxide formation, these reactions can occur at the regions that are schematically depicted in Figure 1-3:

- In the presence of an electric field, we have heterolytic dissociation of water at the **interface between the outer layer and the electrolyte solution**:



The  $\text{O}^{2-}(\text{ox})$  ions migrate from the outer layer/electrolyte interface towards the inner layer/Al interface and the  $\text{OH}^{-}(\text{ox})$  ions migrate towards the inner layer/outer layer interface.

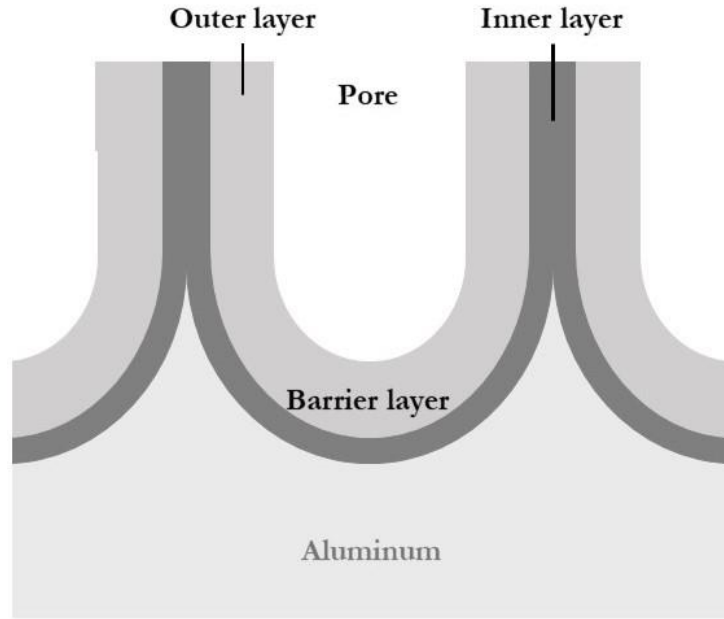
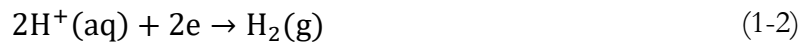


**Figure 1-3** Schematic view of the anodic aluminum oxide nanochannel formation.

- The other part of the  $H^+(aq)$  produced ions migrate towards cathode by virtue of the electric field where they are reduced and released in the form of hydrogen gas:



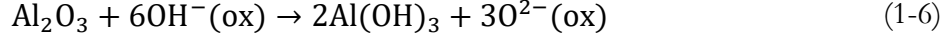
- At the **inner layer/metal interface**:  $O^{2-}(ox)$  ions migrate towards the inner layer/metal interface through the barrier layer and the Al oxides and thickens the barrier layer:



- At the outer layer/electrolyte interface, there is also the direct ejection of  $Al^{3+}$  ions to the electrolyte solution



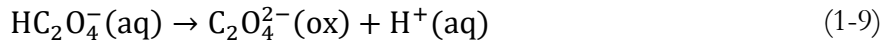
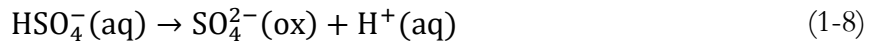
- At the **outer layer/inner layer interface**: Losic et al [36] suggested that the  $OH^-(ox)$  ions formed at the outer layer/electrolyte interface, migrate to the outer layer/inner layer interface and a reaction takes place at this interface that maintains the constant ratio between the thicknesses of these layers:



During the anodization process, we measure the electrical current passing through the circuit. By dividing the electrical current (mA) by the surface of the alumina immersed in the electrolyte solution ( $\text{cm}^2$ ), we reach to the current density of the anodization process which is denoted by  $j$  ( $\text{mA}/\text{cm}^2$ ). This total current density is made up of different contributions [36], [39]. If we consider the total current density as  $j_T$ , then we have:

$$j_T = j_i + j_e \quad (1-7)$$

where  $j_i$  is the ionic current density and  $j_e$  is the electronic current density. The ionic current density can be considered as the summation of the oxidation current density ( $j_o$ ) and incorporation current density ( $j_c$ ).  $j_o$  represents the  $\text{O}^{2-}$  ions that diffuse inwards and have a direct relationship with the AAO formation. On the other hand,  $j_c$  can be explained by the diffusion of the acid radical anions which are considered also as the contaminating species and do not have contribution to formation of the AAO according to the work of Zhu et al [40]. The dissociation reactions of the acids that we have utilized in our work that can contribute to  $j_c$  part of the of the ionic current density are as follows for the sulfuric and oxalic acid [41]:



These anions incorporate in the structure of the alumina and release electrons in the oxide conduction band. The electric field accelerates these electrons and leads to production of more electrons as in an avalanche mechanism. This process contributes to the  $j_e$  which does not contribute to AAO formation.

For the selenic acid, the cathodic reaction are as follows [13]:



Since the reactions of the selenic acid happen on the positive electrode which is the platinum in our anodization cell, the radical species of this acid do not incorporate in the structure of the AAO to the extent of oxalic and sulfuric acids.

By the chemical reactions mentioned and the formation of oxide at the barrier layer, the nanochannels are grown and elongated. The mechanisms through which the nanochannels are formed and grown has remained questioning to the researchers in order to understand the mechanism completely and proposing theoretical models describing the growth of the channels. For example, the field assisted alumina dissolution is one of the proposed models which has been rejected by the researchers since they realized that there is no dissolution of the oxygen from the oxide to the solution [42]. Another recent model is the combination of the oxide viscous flow and the ions migration by electric field [43]. Oxygen evolution is also one of the models that describes the formation of self-ordered AAO nanochannels [44]. The other model is the electrohydrodynamic convection describing the formation mechanism of the self-ordered AAO [41], [45], [46]. But, there are  $Al^{3+}$  ions directly ejected into the electrolyte solution [47]. Another model is the stress driven flow of the oxide due to the incorporation of the electrolyte anions in the oxide structure and adsorption on the oxide [48]. Indeed, because of the high electric field maintained through the bottom surface of the oxide during anodization, some anions of the acid solution migrate through the barrier layer and are incorporated in the structure of the AAO [49]. This anion contaminations can be seen as impurities in the alumina structure that affect the physical properties of the AAO such as the refractive index [50]–[52]. Some researchers have theoretically proposed mathematical models for this incorporation. Their models assert that the region of the AAO channels walls close to the surface is more contaminated with the incorporating anions [53], [54], also confirmed by experimental works [50], [51], [55]. Fan et al showed the maximum percentage of the carbon element at 20 nm distance from the pore surface in an AAO membrane synthesized in 0.3 M oxalic acid solution [55]. The percentage of the impurities can vary up to 12 % of the aluminum percentage based on the anodization parameters such as voltage and acid concentration [52].

In this research work, we have synthesized AAOs using three different acids for anodization: oxalic, sulfuric and selenic acids. Additionally, for the case of oxalic acid, we also varied the concentration of the acid in order to study this effect on the composition and morphological properties of the synthesized AAOs.

## 1.3 Synthesis procedure

### 1.3.1 Electropolishing

Aluminum (Al) sheet with the purity of 99.999 % and the thickness of 0.32 mm was purchased from GoodFellow, UK. Before the anodization, the aluminum sheet undergoes an electropolishing step to remove the surface contaminations and reduce the surface roughness by removing an external surface layer. The electrochemical cell used is schematically shown in Figure 1-4. The Al sheet is set as the anode and a platinum foil is used as a cathode. We used a direct current (DC) Aim'TTi<sup>®</sup> CPX400DP generator for maintaining the desired potential between our electrodes. The cell is filled with a mixture solution made of perchloric acid (purchased with 70% aq purity, Alfa Aesar, Germany) and ethyl alcohol (purchased with 99.8 % purity from Carlo Erba, Germany) and the temperature was set at the desired value using the water bath.

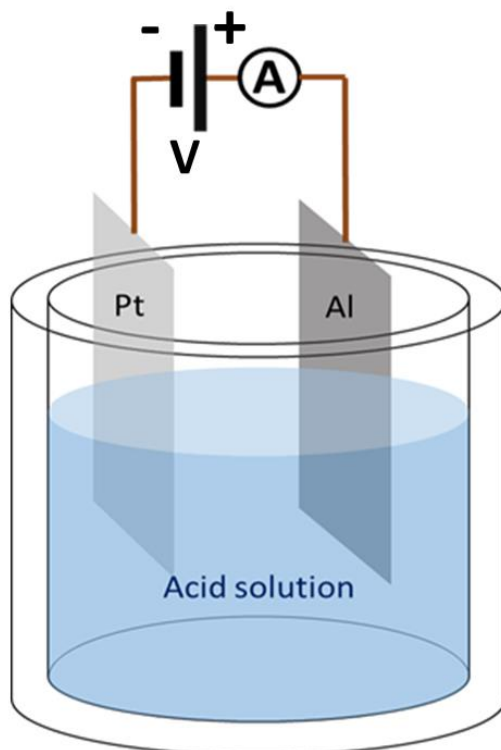


**Figure 1-4** Schematic picture of the anodization cell.

Many electropolishing conditions can be found in the literature [56]–[58]. We previously noticed that for some cases the electropolishing gives rise to a surface roughness (white spots visible on the Al surface). Thus, the optimal conditions (temperature, voltage, and solution composition) for electropolishing used here was determined previously (internship of Chloë Le Bruchec): it was found in their work that by setting the volumetric composition of perchloric acid:ethyl alcohol as (1:4), the voltage at 30 V and the temperature around 0 °C without stirring the issue of roughness appearance on the Al surface can be solved. In about 30 s, the contaminated layer removal is achieved and the Al sheet has a mirror-like appearance, indicating the small surface rugosity. The theory of electropolishing process is still unclear since there is combination of electrochemical reactions and also materials removal from the surface [57]. According to the Pendyala et al [56], the surface roughness of the aluminum in electropolishing is governed by the microsmoothing and anodic leveling, i.e. making the surface level of the aluminum uniform. Both of these mechanisms are controlled by ions diffusion. Since stirring the liquid bath accelerates the diffusion, it leads to the formation of more surface roughness by being aligned with these two roughening mechanisms. For this reason, we succeeded to avoid the surface roughness by stopping the stirring of the solution. According to the work of the same researchers, the Al surface roughness increases with the electropolishing time. Accordingly, by increasing the anodization voltage, we reduced the time as well. It is also observed that the quality of the electropolishing reduced with ageing of the electrolyte solution due to the dissolved metal ions [58], suggesting that the use of fresh perchloric acid / ethyl alcohol solution for each set of electropolishing is important to avoid the formation of an additional roughness on the aluminum surface.

### 1.3.2 Two-step anodization

As mentioned in the first section, the two steps anodization to produce well-ordered AAOs was initially proposed by Masuda and Fukuda [18]. The description of this process is shown in Figure 1-5. The same electrochemical cell schematically shown in Figure 1-4 was used for the two steps anodization. The electropolished pure Al sheet is connected to the positive output of the direct current (DC) AimTTi® CPX400DP generator and the platinum sheet is connected to the negative output and a constant voltage is applied between these two electrodes. The current density  $j$  is recorded over time during the two anodization steps by an AimTTi® multimeter. Thus, the aluminum is the anode electrode on which the oxidation reaction takes place and the reduction reaction occurs on the surface of the platinum sheet. The temperature of the electrolyte solution is maintained on the desired value

by adjusting the temperature of the liquid jacket circulating around the anodization cell. We used three acids in our research work for anodization which were namely oxalic acid (purchased 99% pure, Aldrich, USA), sulfuric acid (purchased 95 to 97% pure, Merck, Germany) and selenic acid (Purchased 40 wt%, Aldrich, US). The cell temperature and the applied voltage will depend on the acid type used. The anodization voltage is 40, 25 and 45 V for oxalic, sulfuric and selenic acid solutions respectively. For the oxalic and sulfuric acid solution the temperature is set on 18 °C while for the selenic acid solution it is 9 or 0 °C. Once the aluminum sheet is anodized in the electrolyte solution at the desired voltage for approximately two hours, a porous alumina layer is formed with disordered nanochannels (see Figure 5, top). Then the aluminum piece is placed in phosphochromic acid solution (1.8 wt% CrO<sub>3</sub> (VWR, EU) + 6 wt% H<sub>3</sub>PO<sub>4</sub> (85% pure, Acros Organics, Czech Republic)) at 50 °C for 2 hours with stirring in order to fully dissolved the first porous alumina. Only the imprints of the dissolved nanochannels remain on the Al surface (see Figure 1-5, middle). Afterwards, the aluminum piece is taken for a second anodization during which the aluminum oxide nanochannels are formed on the imprinted pattern (see Figure 1-5, bottom). The conditions of the second anodization are chosen identical to those of the first one in terms of temperature, voltage and electrolyte. The duration of the second anodization is chosen in order to reach the desired AAO thickness (nanochannel length  $L_P$ ).

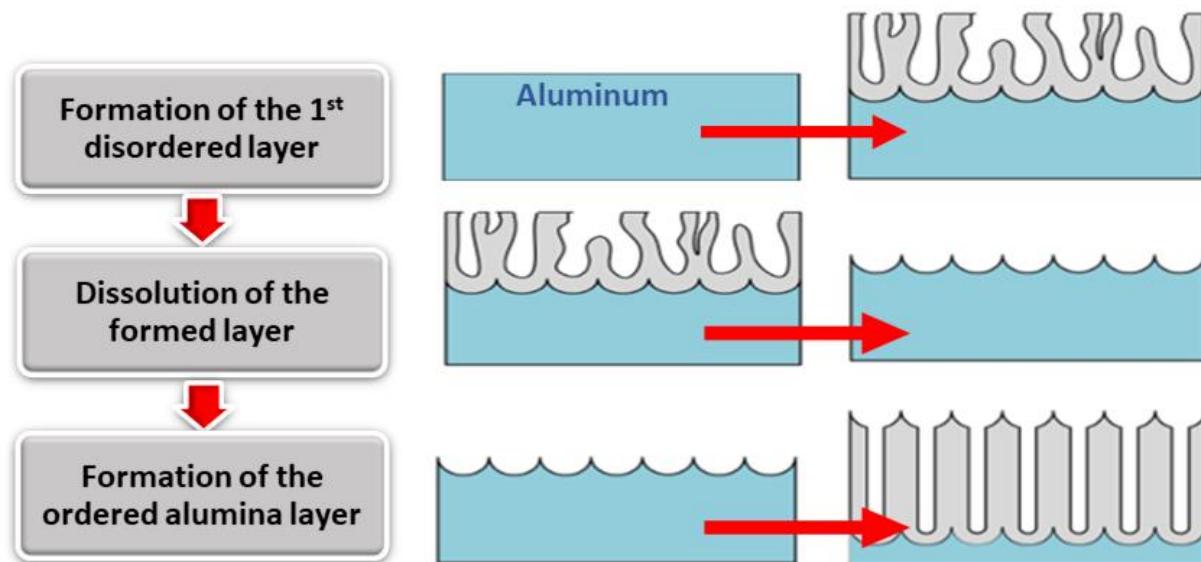


**Figure 1-5** Schematic description of the two-step anodization process for synthesizing self-ordered nanoporous aluminum oxide (AAO).

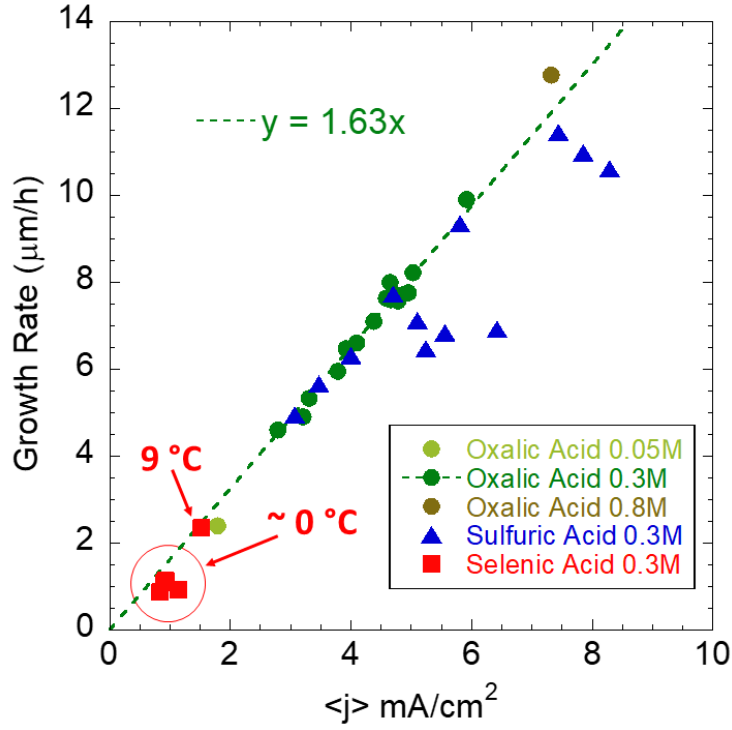


**Figure 1-6** Growth rate ( $\mu\text{m/h}$ ) versus average current density  $\langle j \rangle$  for the second anodization carried out with different acidic electrolytes (OA, sulfuric and selenic) and different concentrations.

The evolution of the growth rate with the average current density  $\langle j \rangle$  for the second anodization carried out with different acidic electrolytes is shown in Figure 1-6. We can see that interestingly, the data fall on a straight line with a slope (named the growth rate coefficient) of  $1.63 \pm 0.05 \mu\text{m}\cdot\text{cm}^2/\text{mA}\cdot\text{h}$  for the 0.3 M OA solutions. By using the Faraday's law this slope can be calculated as:

$$\text{Slope} = \eta_a \frac{M_{\text{alumina}}}{\rho_{\text{alumina}} z F} \quad (1-12)$$

With  $\eta_a$  the anodization efficiency,  $M_{\text{alumina}}$  the molar mass of alumina,  $\rho_{\text{alumina}}$  the density of the alumina,  $z$  the number of electrons to produce alumina (here  $z=2 \times 3=6$ ) and  $F$  the Faraday constant. If one takes a typical value for  $\eta_a$  of 0.77, the molar mass of pure alumina ( $=102 \text{ g/mol}$ ), and a density of  $3 \text{ g/cm}^3$  a value of slope of  $1.63 \mu\text{m}\cdot\text{cm}^2/\text{mA}\cdot\text{h}$  is found.

It can be seen that the growth rate versus average current density fall in linear behavior except for some of the anodizations in sulfuric acid which are denoted by blue triangles in Figure 1-6. These deviations from the fitted line for these points have happened due to the deviations of the measured

current from the steady line due to decrease in the electrical current during anodization by using the acid solution for synthesizing more membranes. We observed that by continuing using the sulfuric acid, the average current density of the anodization is reduced compared to anodization with freshly made acid at the same temperature and voltage. Regarding the growth rate analysis, we had the same approach for the sulfuric and selenic acid membranes and we found the growth rate coefficient to be  $1.43 \pm 0.19$  and  $1.17 \pm 0.27$   $\mu\text{m/h}$  respectively. Thus, we may conclude that the growth coefficient can be a function of the type and concentration of the acid solution.

### 1.3.3 Detachment of AAO from the aluminum substrate

After the 2-step anodization, the porous alumina should be detached from the Al surface in order to obtain through-hole AAO membranes for our electrokinetic studies. We have used the detachment protocol introduced previously by Yanagishita et al [59], [60]. Other methods that have been proposed for detachment are exemplified along with their drawbacks in comparison with the method we chose. The drawbacks consist of lack of uniformity in the bottom diameters of the pores in aluminum substrate dissolution method [61], lack of control on the cracking in the voltage pulse method [62]. There is also the disadvantage of surface roughening of aluminum in some methods like electrolysis at high current in a mixed electrolyte [62]. The chosen detachment procedure is more convenient to produce through-hole alumina membranes with uniform pores diameters distribution and certainty of the opening of the nanochannels. The detachment steps are depicted schematically in Figure 1-7.

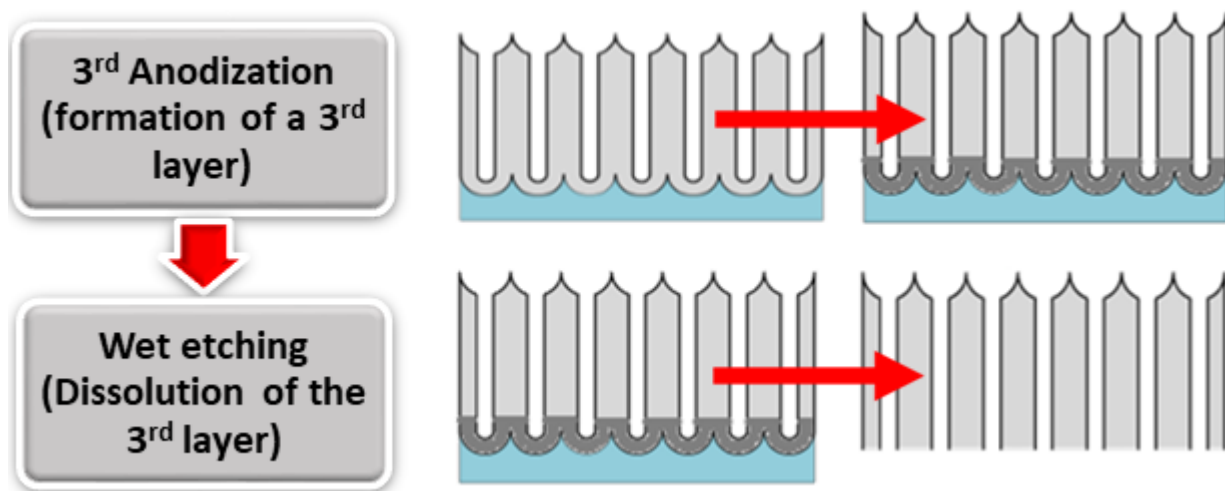


**Figure 1-7** Steps of the detachment process for obtaining through-hole AAO membranes. Method proposed by Yanagishita et al [59], [60].

First, a third anodization is performed in a very concentrated sulfuric acid solution ( $\sim 13$  M) under a voltage similar to the previous anodization steps at low  $T$  ( $\sim 0$  °C) in order to produce a highly soluble layer of around  $3$   $\mu\text{m}$  which is presumably the optimal thickness [59]. We call the AAO layer that is formed during this anodization step the “third layer” in this manuscript. The current density  $j$  recorded during the third anodization is shown in Figure 1-8 for different AAO membranes synthesized in three different acids at  $0.3$  M with similar thickness of  $20$   $\mu\text{m}$  after the 2<sup>nd</sup> anodization. Although the third anodization is always carried out in sulfuric acid at  $\sim 13$  M, the shapes of the curves are different from each other apparently, and it can be due to the differences in pore diameters that we will detail later.

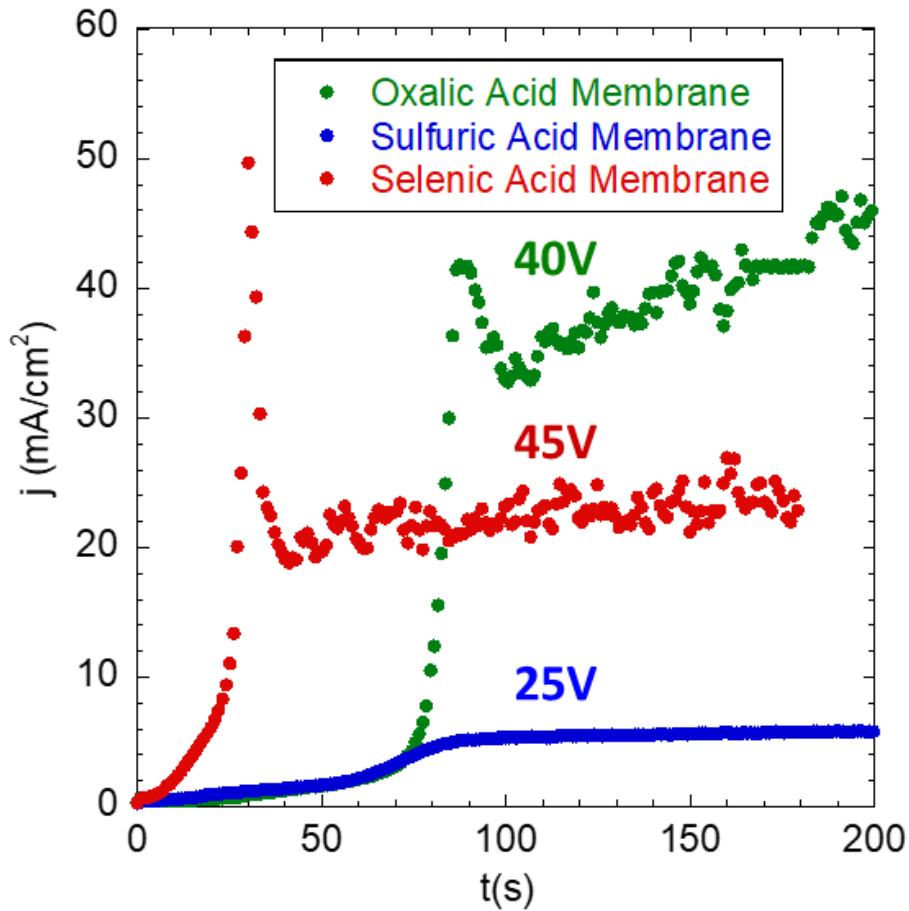


**Figure 1-8** Current density  $j$  versus time recorded during the third anodization for the membranes OA(0.3)-8 (green), SA(0.3)-12 (blue) and SeA(0.3)-6 with the similar  $L_p$  of  $20$   $\mu\text{m}$ .

Since the viscosity of the concentrated sulfuric acid is high, and this high viscosity increases in the low temperature of the anodization, it can be concluded that the main mechanism that controls the third

anodization is the diffusion mass transfer. Since all of these three membranes have the same thickness, we expect to see higher current densities for the higher voltage. But, we observe the lower current density for the case of selenic acid membrane in comparison to oxalic acid membrane. In Figure 1-9, we can see the growth rate of the third layer versus the average current density  $\langle j \rangle$  in the third anodization for the membranes synthesized at different acid types.

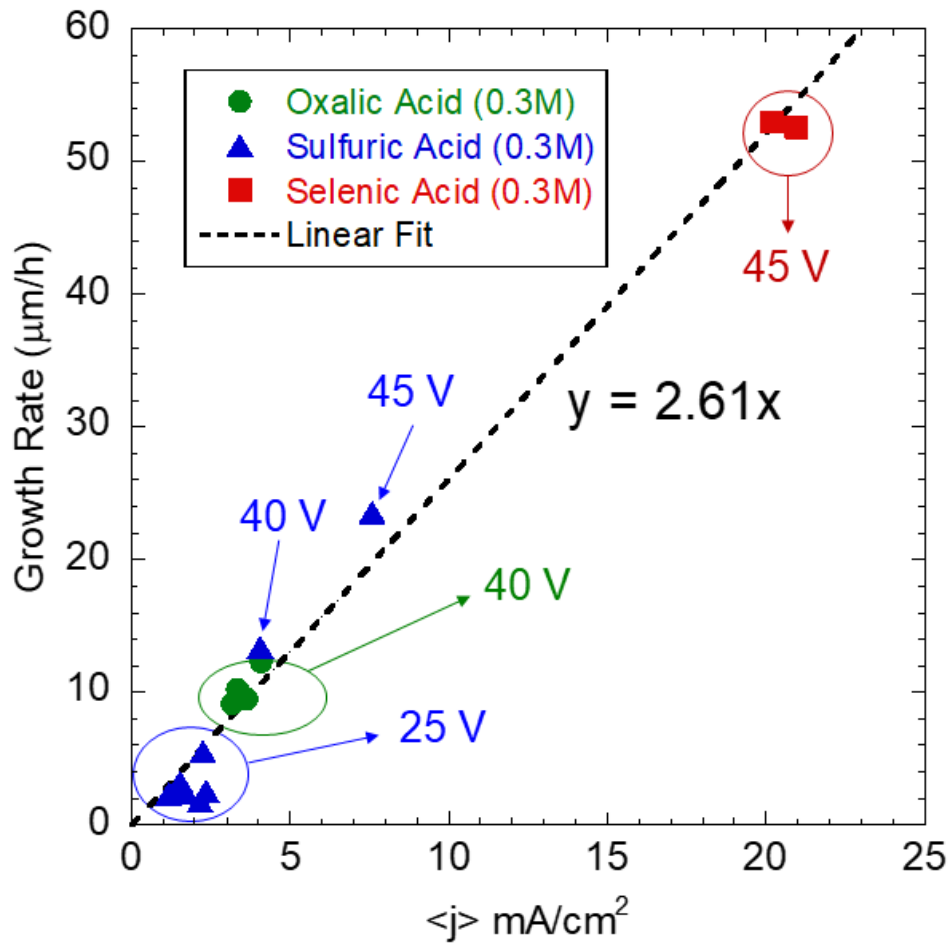


**Figure 1-9** Growth rate of the third layer AAO versus the average current density for the membranes synthesized in three different acids with the same concentration along with the linear fit on the data points.

By a linear fit on the points of Figure 1-9, we obtain a slope of 2.61  $\mu\text{m}\cdot\text{cm}^2/\text{mA}\cdot\text{h}$  which is considerably lower than the slope of the growth rate versus average current density in the second anodization. It shows that in the same current density, the time required for a targeted membrane thickness formation in the 3<sup>rd</sup> anodization is approximately 0.6 of the time needed during second anodization.

Scanning Electron Microscope (SEM) images were recorded with a Hitachi SU-70 FESEM (Field Emission Scanning Electron Microscope - Schottky type gun) at high voltage electron beam of 3 kV and were acquired by a secondary electron (SE) detector located inside the electronic column (Upper detector for Hitachi), which provided nanoscale characterization with a typical limit of separation of 1 nm. We could achieve imaging of surface morphology, without any coating as we used a low current primary beam. Figure 1-10 shows the cross-section SEM image of an AAO membrane after the third anodization in which both the second layer and third layer are visible with the real image and the scheme.

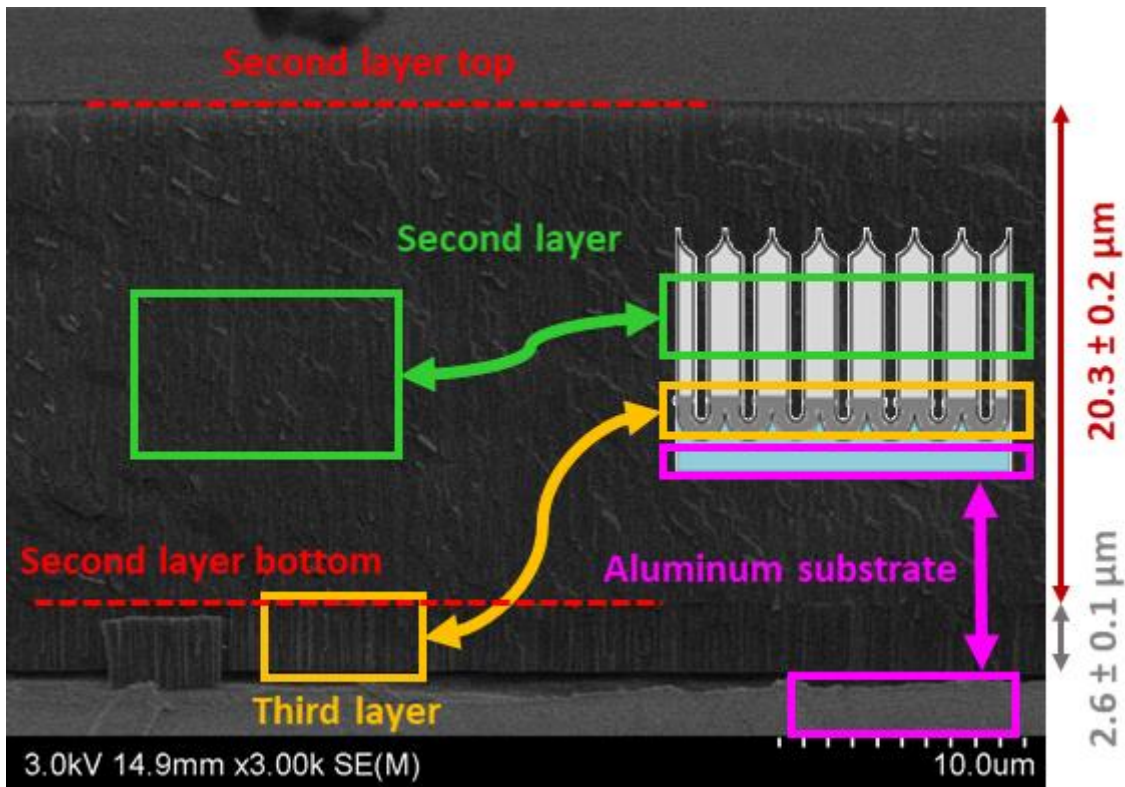


**Figure 1-10** SEM image of SeA(0.3)-6 after the third anodization. The main membrane formed in the second anodization which is about to be separated from the aluminum substrate is referred as “second layer” and the alumina layer formed beneath in concentrated sulfuric acid solution during the third anodization is referred as the “third layer”.

After the third layer formation, we proceed to wet etching to detach the AAO from the Al substrate. The membrane is immersed in the phosphochromic solution at 30 °C with stirring. Since the third layer is formed in a concentrated sulfuric acid solution, it is much more contaminated by sulfate anions that have substituted  $O^{2-}$  ions in the alumina structure and is thus dissolved considerably faster than

the alumina second layer above. Since the phosphochromic acid is destructive to the AAO layer formed in the second anodization, the lower time the AAO remains in the phosphochromic acid, the more favorable is will be in term of pore diameter increase. Thus, the aluminum piece is frequently removed from the acid solution, rinsed and checked if the membrane can be detached. In case it cannot, the sample is re-immersed in the phosphochromic solution for some more time. The time for dissolving the third layer is different for the membranes synthesized with different acid types. This time was about 20 to 30 min for oxalic acid, 45 to 50 min for the sulfuric acid and around 75 min for the selenic acid membranes. Finally, in Figure 1-11, the detached AAO membrane from the Al surface is schematically depicted with the different regions that will be referred in this manuscript. In assigning codes to the membranes, we have the following rule:

***Acid abbreviation (Acid concentration in mol/L)-number of the membrane synthesized in the specific acid***

The abbreviations of the acids that we used in our studies are OA for the oxalic acid, SA for the sulfuric acid and SeA for the selenic acid solution. For example, OA(0.3)-1 denotes the membrane number one that has been synthesized in the oxalic acid with the concentration 0.3M.

In the next section we will proceed to presenting the experimental results of the membrane synthesis stepwise in terms of morphology and the experimental variables affecting them.

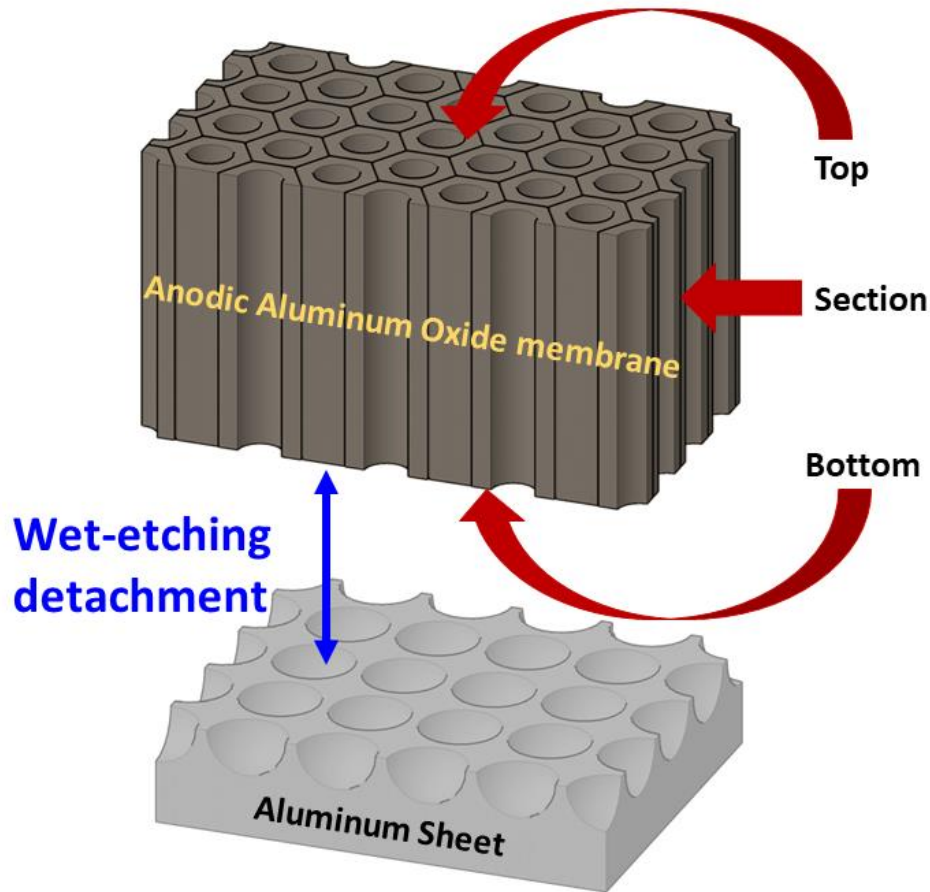


**Figure 1-11** Scheme of the AAO membrane detached from the aluminum substrate surface and the different aspects of this kind of membrane

## 1.4 Characterization of the anodic aluminum oxide membranes

At this step, we go through a deep characterization of our synthesized AAO membranes from compositional and also morphological points of view. The detachment process is critical to produce through-hole AAOs for the following electrokinetic studies of polyelectrolyte behavior in nanoporous medium. Thus, the first part in this section is dedicated to the better understanding of this detachment process (third anodization followed by wet etching) by investigating the composition of the third layer. The analysis of the elemental composition was performed by Energy Dispersive X-ray Spectrometry (EDX) thanks to an Oxford X-Max 50 mm<sup>2</sup> detector fitted to the SU-70 FESEM. Oxford's AZtec

software was used for the acquisition. We chose a low voltage condition (5 kV) as the poor conductivity of our samples objected the use of high currents resulting from high voltages.

Then, once the AAO is detached, we pass through a detailed morphological characterization of the through-hole membranes by SEM and we discuss the effect of different parameters affecting the AAO characteristic sizes. The AAO elemental composition is also studied by Energy Dispersive X-ray Spectrometry (EDX) and FTIR experiments, giving more insights into the ions incorporation in the AAO structure as a function of the experimental parameters and its effects the AAO refractive index.

First, after the third anodization and before wet etching, we analyzed the composition of the second and third layer. For these samples, the EDX spectrometry is conducted from the cross section. The main aim of these set of spectroscopies was to evaluate three points: first the ratio of oxygen over aluminum to see to what extent it is close to the pure aluminum which is theoretically 1.5. The second was the extent to which the 3<sup>rd</sup> layer is contaminated with sulfur. The sulfur contamination of this layer is the key factor in dissolution of this layer in the wet etching and detachment of the membrane. Since the contamination with sulfur is the main factor for the 3<sup>rd</sup> layer to be dissolved in the phosphochromic acid, the S/Al ratio is plotted in Figure 1-13b. The third factor to be studied by the analysis of EDX data is the extent of contamination of the 2<sup>nd</sup> and 3<sup>rd</sup> layers by the elements of the acids in which the membranes are synthesized in which are namely C for the oxalic acid, S for the sulfuric acid and Se for the selenic acid. These contaminations can explain how much the radical anions of the acids have incorporated in the membrane structure by mechanisms such as substitution with the O<sup>2-</sup>. In Figure 1-12 the examples of raw EDX spectra of the membranes synthesized in oxalic, sulfuric and selenic acid are presented.

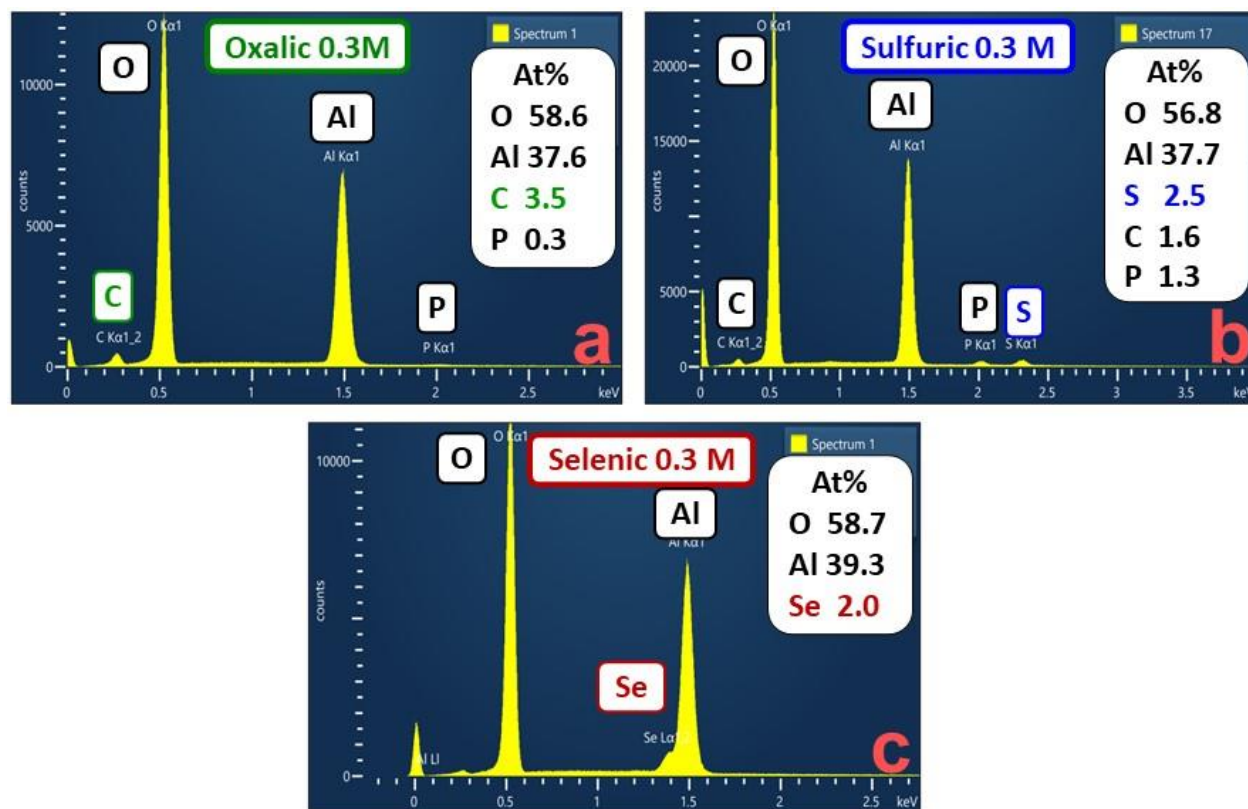


**Figure 1-12** examples of raw EDX spectra of the membranes synthesized in **a)** oxalic **b)** sulfuric and **c)** selenic acid solutions with 0.3 M concentration.

We present the results in terms of the ratio of the percentage of the elements over the percentage of aluminum. In Figure 1-13 we can see the ratios of the element percentages over aluminum versus average current density for the membranes before detachment. The 3<sup>rd</sup> anodization of two of the sulfuric acid membranes has been done in a voltage different from the second anodization. These voltages have been 40 V for the SA(0.3)-6 and 45 V for the SA(0.3)-8. The data points of these two membranes have been denoted in Figure 1-13 a, b, c with their third anodization voltages.

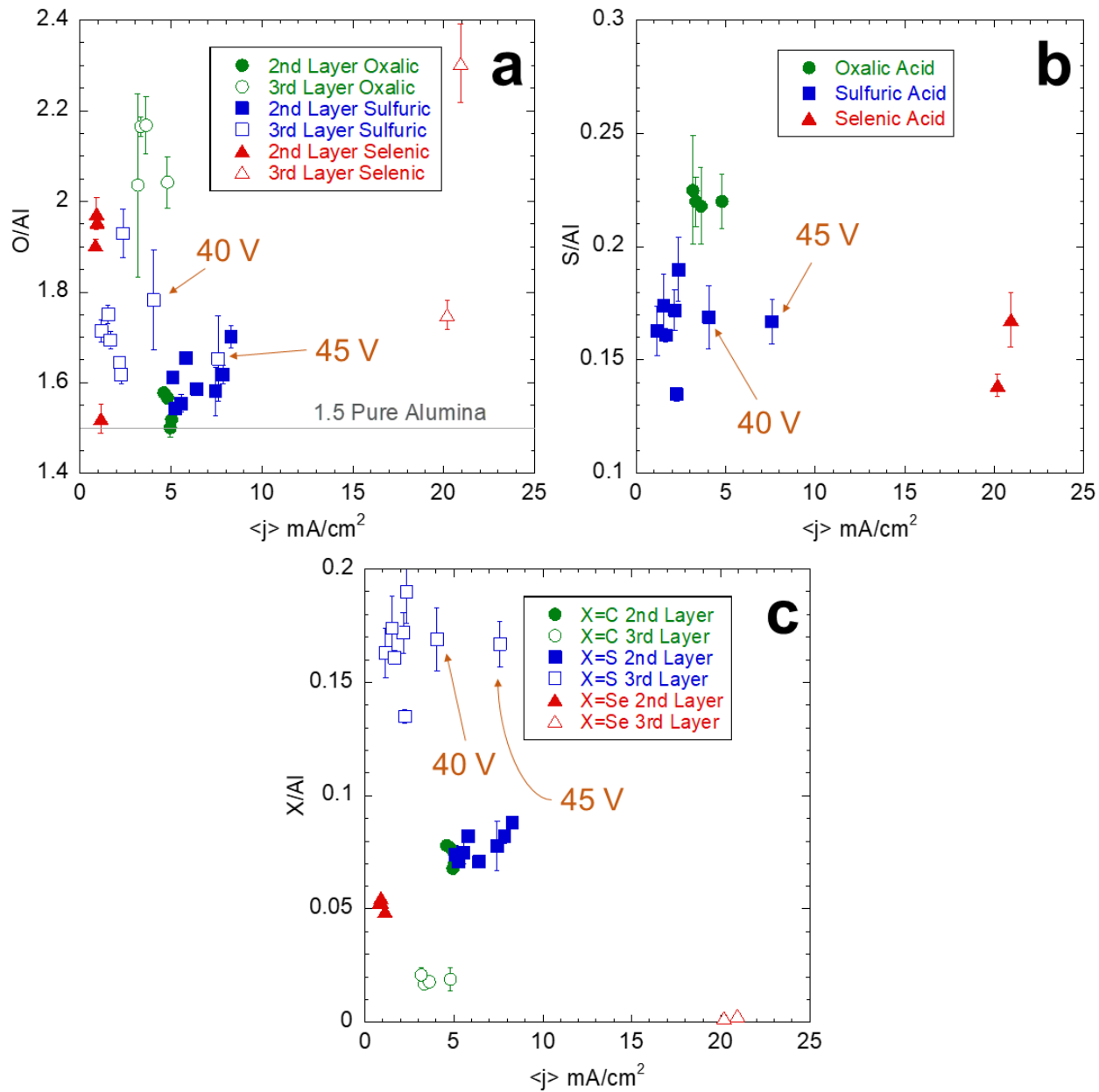


**Figure 1-13** EDX results analysis of the membranes synthesized in different acids with the same concentration of 0.3 M before detachment<sup>1</sup> **a)** Oxygen over alumina in the 2<sup>nd</sup> and 3<sup>rd</sup> layers **b)** sulfur over aluminum in the 3<sup>rd</sup> layer **c)** the ratio of the specific element existing in the acid solution in which the membranes are synthesized which is C for the carbon in oxalic acid (green points), S for the sulfur in sulfuric acid (blue points) and Se the selenium in selenic acid (red points).

<sup>1</sup> Membranes analyzed in this figure are OA(0.3)-1 to 4, SA(0.3)-1 to 8 and SeA(0.3)-3 to 6.

#### 1.4.1.1 Sulfur content in the third layer

It was aimed to use the EDX spectroscopy results to study the reasons of failure of the wet etching from the elemental spectroscopy point of view. The detachment of oxalic acid synthesized membranes was the easiest compared to the membranes synthesized in the two other acids. This is in line with what we observe in this figure. The S/Al is the highest in the 3<sup>rd</sup> layer formed beneath the oxalic acid synthesized membranes (green marks). Although the S/Al is a key factor in solubility of the third layer and detachment of the membrane, for the membranes SA(0.3)-6 and SA(0.3)-8 we failed to detach the membrane. It can be due to the difference between the third anodization and second anodization voltages of these two membranes. Because of the voltage, the pores arrangement in the third layer has been different from that of the second layer. Accordingly, the channels of the second and third layer had not been aligned and this fact makes the diffusion of the phosphochromic acid and dissolution of the third layer complicated.

Despite the higher voltage for the selenic acid membranes, the S/Al ratio in the third layer of these membranes does not exceed that of the oxalic and sulfuric acid membranes. Besides, for two samples of the sulfuric acid membranes, we increased the voltage of the third anodization to 40 and 45 V. But, still we do not observe this ratio to exceed that of the 3<sup>rd</sup> layer of the oxalic acid membranes though the number of pores per unit area is around 2.5 times higher that of the oxalic acid membranes. Thus, it shows that the extent of contamination of the third layer by sulfuric radical anions in the third anodization is not led mainly by the voltage of the third anodization. Thus, it can be concluded that the main factor that can control the sulfur contamination and accordingly the success of the wet etching and detachment is the morphology of the pores. In the next sections, we will go through the morphology of the membrane pores.

#### 1.4.1.2 Anions incorporation in the 2<sup>nd</sup> and 3<sup>rd</sup> layer

Figure 1-13 indicated the relations between the ratio of the elements over aluminum and the average current density during the anodization of the aluminum for synthesizing the membrane. First of all, the O/Al ratio seems to be different from the conventional aluminum oxide. The values do not show dependence on the current density since in Figure 13a there are no considerable differences between the O/Al in the 3<sup>rd</sup> layer of the selenic acid synthesized membranes compared to the 3<sup>rd</sup> layer of the other membranes. While we can see that the average current density of the 3<sup>rd</sup> layer formation

for selenic acid is around 20 mA/cm<sup>2</sup> and for the oxalic and sulfuric acid membranes ranges from nearly 2 to 10 mA/cm<sup>2</sup>. Hence, the O/Al ratio can be dependent on the type and concentration of the acid used for the anodization and consequently the type of the radical ions included in the structure of the synthesized alumina membrane. It is observed that the 3<sup>rd</sup> layer that is formed in the concentrated sulfuric acid solution, the O/Al ratio deviates higher from the 1.5 value which corresponds to the pure aluminum oxide. Furthermore, in Figure 1-13a, the O/Al in the 2<sup>nd</sup> layer for one of the selenic acid synthesized membranes is highly closer to 1.5 compared to the two others. It can be related to the lower concentration of the selenic acid in the solution because a part of the selenic acid in the solution is consumed during the anodization of the two previous selenic acid membranes. The S/Al ratio in Figure 1-13c (for the blue data points of sulfuric acid synthesized membrane where X = S) confirms more the dependence of contamination extent on the acid concentration. It is observed that despite the higher average current density in forming the 2<sup>nd</sup> layer and the same voltages, the S/Al ratio is considerably higher in the 3<sup>rd</sup> layer. The only difference between formation of the 2<sup>nd</sup> and 3<sup>rd</sup> layer of this membrane is the acid concentration which is higher for forming 3<sup>rd</sup> layer.

Thus, we can conclude that the incorporation of the ionic species in the AAO structure is dependent on the acid concentration. Because in the same acid concentration and types at different voltages, the extent of incorporation of the acid species did not show considerable differences. Because we observed that the deviations of the Al/O ratio from 1.5 (corresponding to pure alumina) increased with increasing the anodization acid concentration rather than the anodization voltage. S/Al ratio in for the sulfuric acid membranes in Figure 1-13c also confirms this.

#### 1.4.1.3 Dissolution time of the 3<sup>rd</sup> layer

Another important parameter that should be considered in the detachment of the AAO membranes in wet etching is the dissolution time of the third layer in phosphochromic acid. In the 3<sup>rd</sup> anodization, same thickness of the third layer was targeted for all of the membranes. But, the time that the different membranes needed to remain in the phosphochromic acid solution for their 3<sup>rd</sup> layer to be dissolved was different. For oxalic acid membranes, this time was around 20 minutes. While for the sulfuric acid membranes this time was 45 to 50 minutes and for selenic acid synthesized membranes this time exceeded 75 minutes. We observed that the sulfuric acid contamination in the third layer of the oxalic acid membranes is higher than the third layer of sulfuric and selenic acid synthesized membranes. But, according to Figure 1-12b, this contamination is not considerably different between sulfuric and selenic acid membranes. The difference can be due to the pore diameters difference. We

do not have SEM images of the surface of sulfuric and oxalic acid membranes surfaces before detachment. For some of our selenic acid membranes, the morphological properties have been calculated before detachment by the SEM images taken from the top surface of the membrane. These data are presented in Table 1-1.

It can be seen from Figure 1-14 that shows the SEM images from the top surface of the selenic acid synthesized membrane that the pore diameters of the selenic acid membranes are smaller than those of the sulfuric acid membranes. This can make the diffusion of the phosphochromic acid through the nanochannels and dissolution of the 3<sup>rd</sup> layer more complicated.

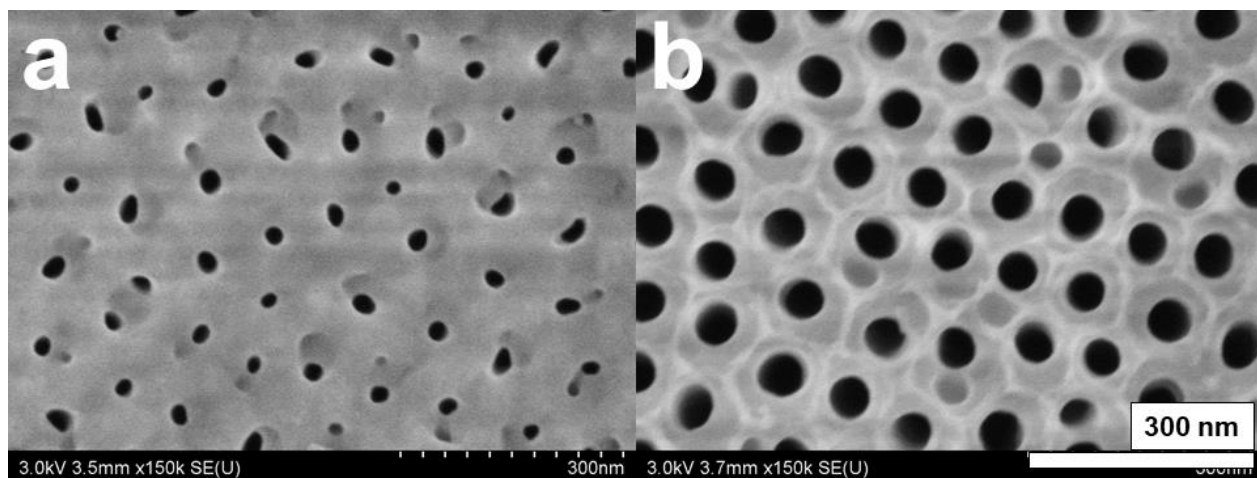


**Figure 1-14** SEM images of the top surface of the SeA(0.3)-6 membrane **a)** before and **b)** after wet-etching and detachment from the aluminum substrate.

**Table 1-1** Morphological properties of the membranes synthesized in selenic acid 0.3M solution.

<b>Code name-(side)</b>	<b>Average pores diameter (nm)</b>	<b>Pores density (cm<sup>-2</sup>)</b>	<b>Porosity (%)</b>
<b>Before wet-etching and detachment</b>			
<b>SeA(0.3)-3-(Top)</b>	22 ± 4	1.14 × 10 <sup>10</sup>	4.6
<b>SeA(0.3)-4-(Top)</b>	20 ± 3	1.25 × 10 <sup>10</sup>	4.1
<b>SeA(0.3)-5-(Top)</b>	24 ± 3	1.23 × 10 <sup>10</sup>	5.8
<b>SeA(0.3)-6-(Top)</b>	23 ± 3	1.2 × 10 <sup>10</sup>	5

### 1.4.2 Characterization of through-hole AAOs: influence of the different experimental parameters

In this section, once we have the AAO membranes detached, we proceed to characterizing them from morphology and composition aspects. It is aimed to obtain the detailed information about the pore diameters, number of pores per unit area (pore density) plus anodization variables that affect these characteristics. After studying the morphology, we proceed to study the composition of the membranes to have insights about the distribution of the different chemical species at different regions of the membrane.

#### 1.4.2.1 Structural characterization of through-hole AAOs

On some membranes, the EDX spectroscopy was done after the detachment in order to understand the elemental distribution at different regions of the membrane. The latter was intended to be utilized to explain the differences observed in the surface charge characteristics between the different areas of the membrane such as the top surface, the bottom surface and the nanochannels surface.

At this step we present the morphological specifications of the AAO membranes in Tables 5 to 7 in Appendix. The specifications such as the average pores diameter, pore density (Number of the pores per 1 cm<sup>2</sup>) and the porosity of the AAO membranes have been calculated by treating the SEM images by the ImageJ<sup>®</sup> software. The morphology of these membranes has been studied after detachment

from the top and bottom surface SEM images. Hence, the morphological properties mentioned above are presented for the top and bottom surfaces separately. In Figure 1-15 we show an example of top and bottom surfaces of the detached membranes synthesized in oxalic acid at 0.3 M with three different magnifications of the SEM microscope. It is aimed to give examples of the morphology of the top and bottom surfaces of the membranes synthesized in the most well-known acid and concentration with different magnifications in this figure.

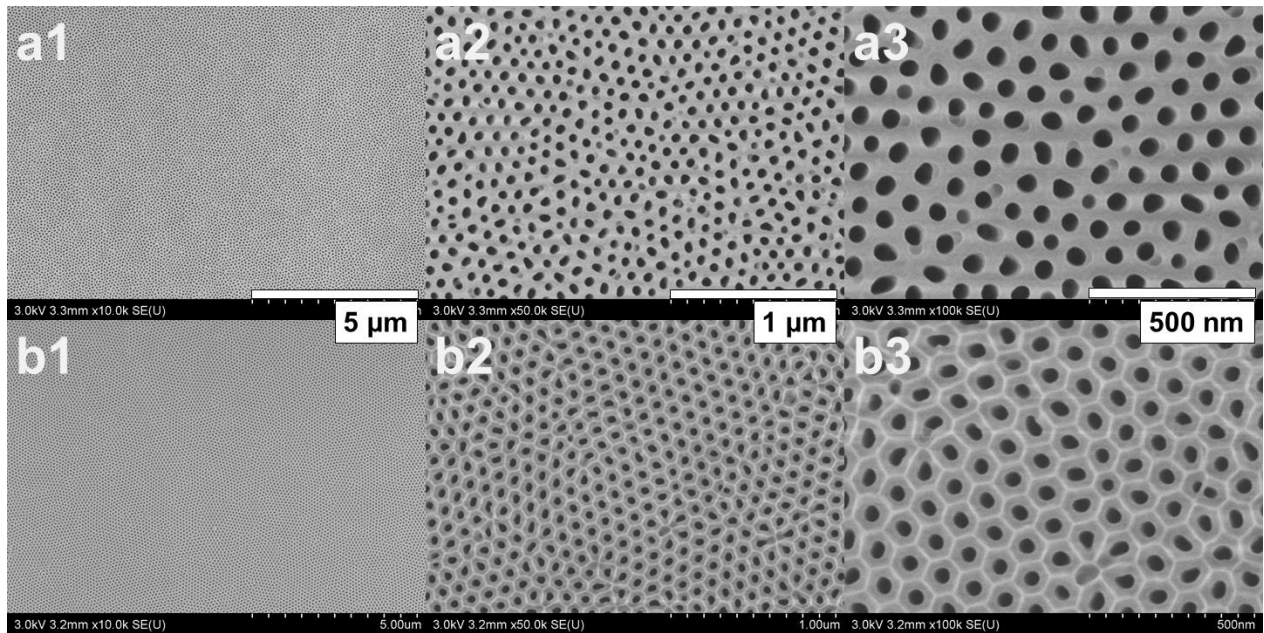


**Figure 1-15 a)** Top and **b)** bottom surface images of the OA(0.3)-16 membrane after detachment with **1)**  $10^4$  **2)**  $5 \times 10^4$  and **3)**  $10^5$  magnifications. For example, a1 shows the top surface image with  $10^4$  magnification.

In Figure 1-16, the SEM images of three membranes have been indicated from three aspects of top, bottom and section. These images are the examples of the SEM images that we have utilized for characterizing our membranes. The membranes whose images are presented in Figure 1-16 are the OA(0.3)-16, SA(0.3)-10 and SeA(0.3)-6.

By using the SEM images and analyzing the images for other membrane samples, we have obtained the average pore diameters and also pores density of the membranes after detachment. The values are presented in Tables 5 – 7 in the appendix. The pores densities were found to depend on the anodization voltage and also the acid concentration. Because the pores density of the membranes synthesized in 0.05 M oxalic acid solution was around  $9 \times 10^9$  while this value was  $1.2 \times 10^{10} \text{ cm}^{-2}$  for the membranes

synthesized in 0.8 M and  $1.05 \times 10^{10}$  for the 0.3 M concentration. For discussing the pore diameters distribution of the membrane, they are presented for the top surface and bottom surface. In Table 1-2 the average values of the morphological properties of the membranes synthesized in oxalic and sulfuric acids are presented. It can be concluded that the pore density reduces with the voltage and acid concentration.

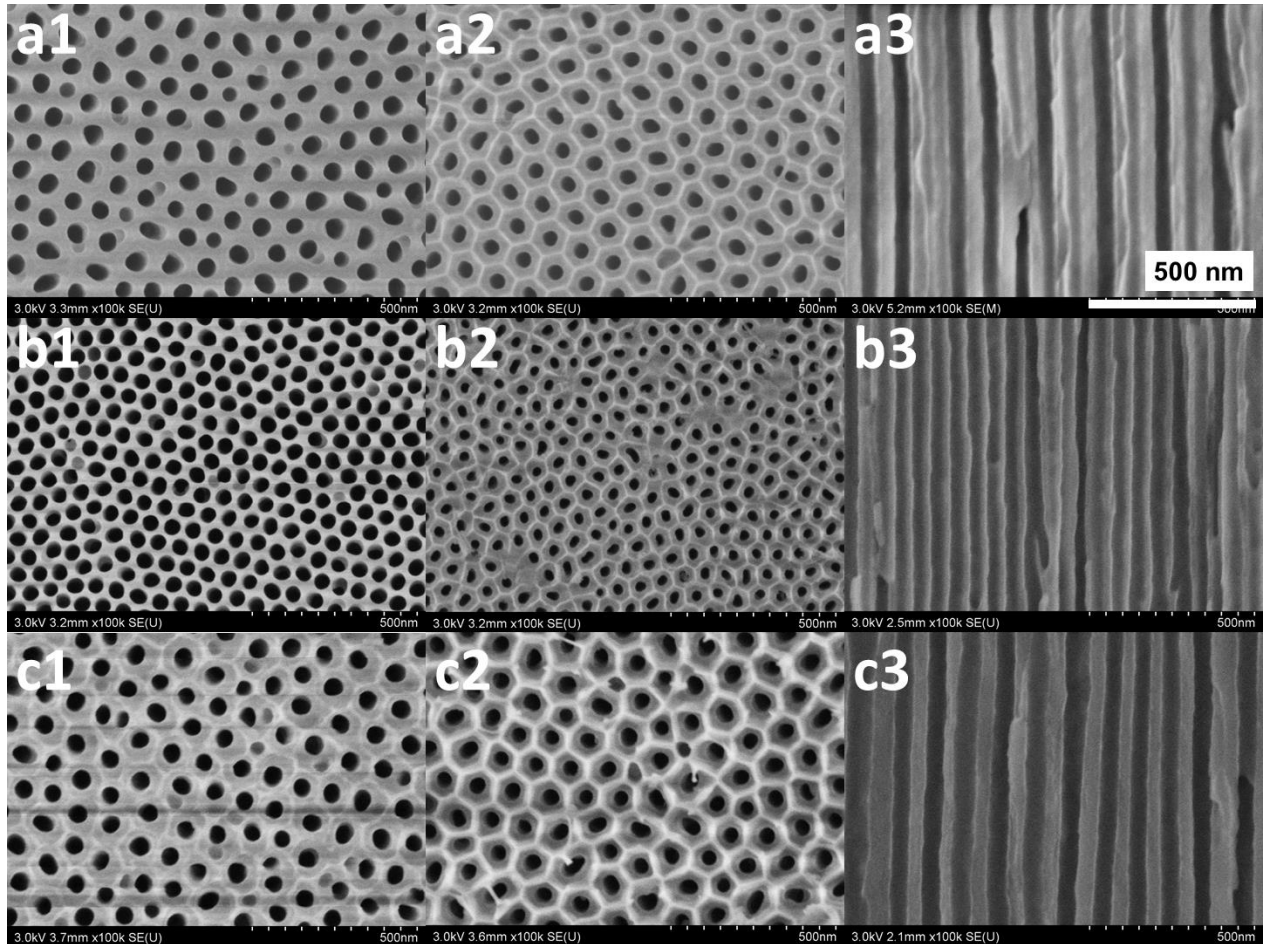


**Figure 1-16** SEM images of the membranes synthesized in **a)** oxalic **b)** sulfuric and **c)** selenic acid 0.3M solutions from **1)** top **2)** bottom and **c)** cross-section viewpoints. For example, a1 is the top surface image of the membrane synthesized in oxalic acid 0.3 M.

Important points were observed in the morphological studies on the hole-through membranes synthesized. First of all, it can be seen that the porosity and the pore diameter of the top surface of the membranes is higher than the bottom surface. This is mainly due to the exposure of the top surface to the acid solutions during the third anodization and wet-etching processes. This is in accordance with

the findings of the previous researchers regarding the fact that the alumina dissolves in the acidic and alkaline solutions [63]. Besides, the chemical resistance of these membranes is highly dependent on the presence of the incorporate ions and their amount in their structure [64]. Thus, we can see that the difference between the pore diameters of the top and bottom surface is higher in the membranes synthesized in 0.8 M oxalic acid solution compared to the membrane synthesized in 0.05 M oxalic acid solution due to the higher rate of dissolution in acid. The membranes of different thicknesses synthesized in the same kind and concentration of acid solution show more differences between the top and bottom surface pore diameters. This can be according to the fact that the mechanism of wet-etching is controlled by the diffusion due to the diameters size of the membranes channels which are less than 100 nm. For examples refer to the Table 6 in appendix showing the morphological feature of sulfuric acid synthesized membranes. Thus, the membranes possessing longer nanochannels should remain longer in the phosphochromic acid for the wet-etching to succeed (SA(0.3)-9 and 10 remained longer in phosphochromic acid solution compared to SA(0.3)-11 and 12).

**Table 1-2** morphological properties of the membranes synthesized in different acid types and concentrations.

<b>Acid - Concentration</b>	<b>Side</b>	<b>Average pores diameter (nm)</b>	<b>Average Pores density (cm<sup>-2</sup>)/10<sup>10</sup></b>	<b>Average Porosity (%)</b>
<b>Oxalic Acid – 0.05M</b>	Top	62 ± 8	0.868	26
	Bottom	53 ± 8	0.988	23
<b>Oxalic Acid – 0.3M</b>	Top	52 ± 6	1.05 ± 0.05	23 ± 5
	Bottom	44 ± 2	1.04 ± 0.07	15 ± 2
<b>Oxalic Acid – 0.8M</b>	Top	56 ± 5	1.21	31
	Bottom	48 ± 3	1.10	21
<b>Sulfuric Acid – 0.3M</b>	Top	42 ± 6	2.55 ± 0.09	35 ± 7
	Bottom	32 ± 5	2.48 ± 0.19	18 ± 5
<b>Selenic Acid – 0.3M</b>	Top	52 ± 6	1.01 × 10 <sup>10</sup>	22.2
	Bottom	44 ± 7	9.9 × 10 <sup>9</sup>	15.4

### 1.4.2.2 Elemental characterization of through-hole AAOs

The elemental characterization of the detached AAO membranes are done in order to have insights about the elemental compositions of these membranes. In Figure 1-17, we have presented the elements ratio based on the EDX results for the detached membranes.

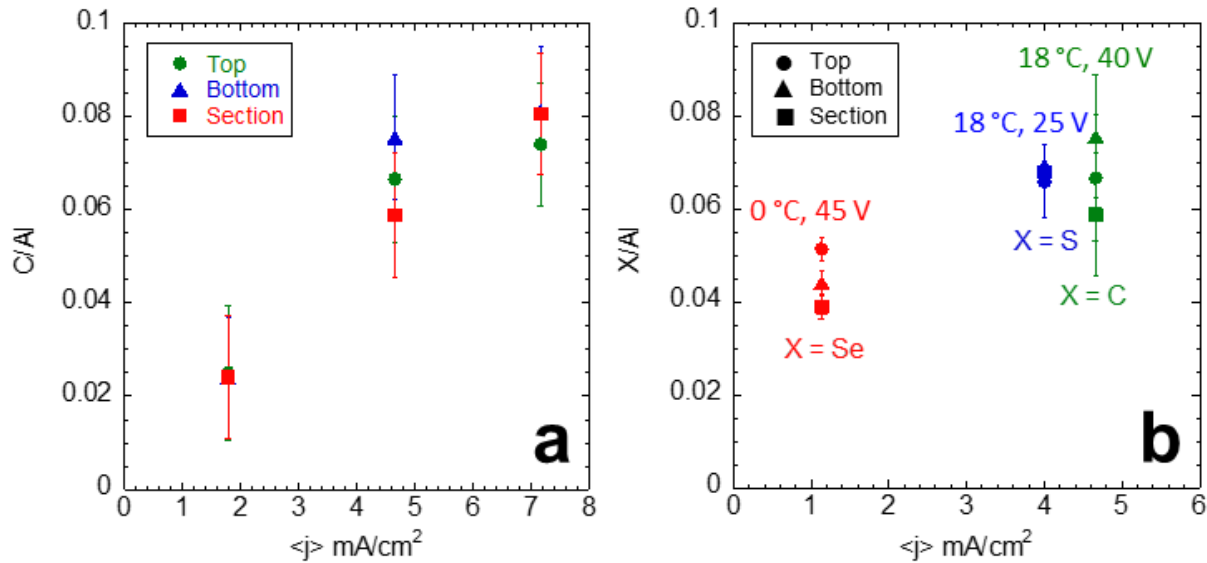


**Figure 1-17** Elemental ratios of elements over Al obtained from EDX analysis after wet etching and detachment plotted as a function of anodization current density ( $\langle j \rangle$  mA/cm<sup>2</sup>). **a)** Ratio of C over Al in the membranes synthesized with different concentrations of oxalic acid **b)** X over Al ratio for oxalic (green), sulfuric (blue) and selenic (red) 0.3M acids<sup>1</sup>.

In Figure 1-17a we can see that the extent of the contamination is dependent on the acid concentration. Because it shows the C/Al ratios at top, bottom and cross-section of the membranes synthesized by anodization at different oxalic acid concentrations which are 0.05, 0.3 and 0.8 M. The amount of carbon contamination from the external sources has been subtracted from our data. The anodization voltage is 40 V same for all of them. Another point that is concluded from Figure 1-17 is that the extent of contamination is the same at different regions of a detached membrane piece and the differences are within the error bars. It is observed in graph Figure 1-17b that the ratio of the main element of the radical anion of the acid to aluminum depends on the average current density during the anodization. It cannot be only a function of voltage because the anodization voltage in selenic acid

<sup>1</sup> Membranes analyzed in this figure are OA(0.05)-1, OA(0.3M)-16, OA(0.8)-2, SA(0.3)-10, SeA(0.3)-6.

is higher than the other two acids although we have the lowest X/Al for the case of selenic acid membrane. The concentration is also the same for the three acid types and it is 0.3 M. Thus, the reason can be sought in other factors such as the anodization temperature (around 0 °C) for this acid type or the morphology of the pores. Besides, the sidary reactions of selenic acid occurs on the cathode and we see a layer of selenium forming on the surface of the platinum cathode. But, for the other acid types the sidary reactions takes place on anode and the resultant radical anion ( $\text{SO}_4^{\cdot-}$  or  $\text{C}_2\text{O}_4^{\cdot-}$ ) competes with the  $\text{O}^{2-}$  to make bonds with  $\text{Al}^{3+}$ . For this reason, we have potentially lower contamination of the AAO by the anodic radical for the case of selenic acid.

One of the methods used for the characterization of the synthesized membranes was the Fourier transform infrared (FTIR) spectroscopy (Tensor27, Bruker) conducted in transmission mode. The aim was to gain more insights into the chemical groups existing within the AAOs membranes. Besides, it was also aimed to evaluate the differences in composition between the alumina membranes synthesized in different acid solutions or different concentrations. In Figure 1-18 the infrared transmittance versus the wave number is depicted for the AAOs synthesized in three different acids at a given concentration of 0.3 M. In Figure 1-19, the goal is to compare the differences between the spectra of the membranes synthesized in different acid concentrations.

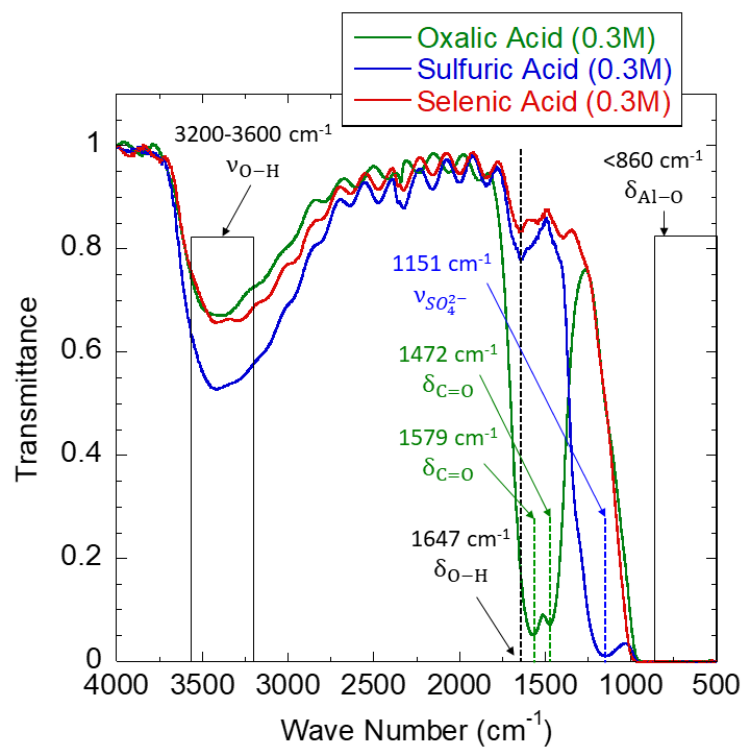


**Figure 1-18** Fourier transform infrared spectra of the OA(0.3)-16, SA(0.3)-12 and SeA(0.3)-6 membranes all synthesized in 0.3 M acid concentration with similar thicknesses (~ 20 μm).

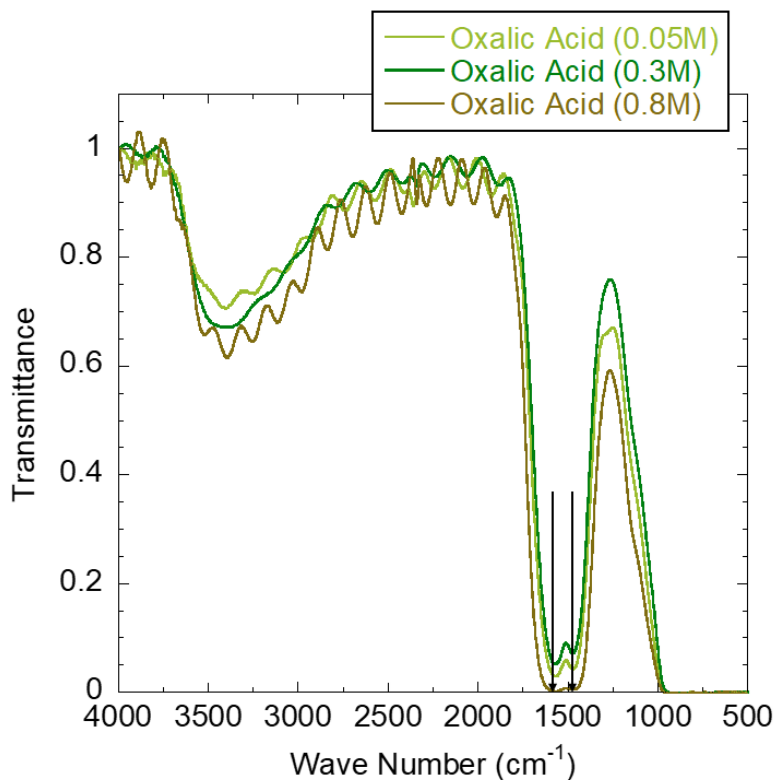


**Figure 1-19** FTIR spectroscopy of the OA(0.05)-1, OA(0.3)-16 and OA(0.8)-2 membranes.

From Figure 1-18 we can see evidently the incorporate species in the anodic alumina membranes synthesized. We can see that all of the membranes showed an adsorption band between 3200 and 3600  $\text{cm}^{-1}$  which corresponds to the water stretching vibration [65]. Besides, the sulfuric and selenic acid synthesized membranes show the adsorption band at around 1647  $\text{cm}^{-1}$  which corresponds to water deformation [52]. The incorporate oxalic species in the aluminum oxide membrane can be proved by the symmetric and asymmetric C=O bonds stretching in shown in the wave numbers 1472 and 1579  $\text{cm}^{-1}$ . For the selenic acid synthesized membrane, according to the EDX data, lower contamination is expected by the acid species since the selenic acid decomposition of the selenic acid occurs on the cathode electrode in contrast with the other two acids which decompose on the anode side. In case of contamination with the selenic acid radical anions, we expect to observe adsorption in the fundamental wave numbers corresponding to selenite ( $\text{SeO}_4^{2-}$ ) groups whose symmetric stretching vibration is shown between 790 to 806  $\text{cm}^{-1}$  [66]. Even in case of having the adsorption due to these groups and Se-O bonds, they are dubious due to the saturation of the transmittance curve according to the Al-O bond vibrations. For the sulfuric acid synthesized membranes, a very low transmittance is observed in the wavenumber 1151  $\text{cm}^{-1}$  which is more probable to be ascribed to the  $\text{SO}_4^{2-}$  ligand complexed with a metal [67] rather than free  $\text{SO}_4^{2-}$  anion. Hence, the incorporation of the sulfuric acid radical anions in the structure of the AAO synthesized in sulfuric acid is also shown. Thus, the FTIR spectroscopy on our membranes acts as a proof complementary to EDX spectroscopy for showing the contamination of the membranes by the radical anions of the acid solutions used for the AAO synthesis. In particular, we observed this for the oxalic and sulfuric acid synthesized AAO membranes and it is obvious in Figure 1-19 that the transmittance in the wave number corresponding to the C=O vibrations reduced with the increase of OA concentration, confirming the higher incorporation of the oxalate radicals in the AAO structure.

In order to have another evaluation on the composition and structure of the AAO membranes synthesized, the FTIR spectra can also be used for the determination of the alumina refractive index. Refractive index of the materials is measured for obtaining the optical features of the materials since these features give insight to the structure and composition of the materials. In general, refractive index has been measured in all states of materials either solid, liquid and gas. The overall approach of the refractive index measurement is radiating a ray beam to the material and then analyzing the transmission spectrum. By fitting the transmission spectrum on known models, it is feasible to obtain the refractive index from which it is possible to discuss about the structure and composition of the

materials. In our work, the beam passed through the membrane sample is in the infrared range. The approach used for this calculation is explained in the work of Zhang et al [68] based on Maxwell-Garnette theory. Based on this theory, in case we assume the dielectric coefficient of the porous alumina as  $\epsilon_{\text{eff}}$ , the dielectric coefficient of the alumina frame as  $\epsilon_{\text{AlOx}}$  and  $\epsilon_{\text{Air}}$  as the dielectric coefficient of the air that is trapped in the nanoporous structure in the nanochannels, there is a correlation between these dielectric coefficients as shown by equation (1-13):

$$\epsilon_{\text{eff}} = \frac{\epsilon_{\text{air}} + 2\epsilon_{\text{AlOx}} + 2f(\epsilon_{\text{air}} - \epsilon_{\text{AlOx}})}{\epsilon_{\text{air}} + 2\epsilon_{\text{AlOx}} - f(\epsilon_{\text{air}} - \epsilon_{\text{AlOx}})} \quad (1-13)$$

$$\epsilon = n^2 \quad (1-14)$$

where  $n$  is the refractive index. In equation 1-13,  $f$  is the filling fraction of air which is considered as the porosity. As we see in the FTIR graphs, there are oscillations in the transmittance and these oscillations can be explained by Fabry-Perot interferences phenomena. For this concept, it should be assumed that both  $\text{Al}_2\text{O}_3/\text{air}$  interfaces are partly reflective. Besides, the thickness of the thin film on which we conduct the spectrometry, is in the order of the wavelength of the beam passing through them. Therefore, the amplitude of the oscillations decrease when the thickness of the film increases. Each of the periods of these oscillations occur on a specific wave number. There is the following correlation between the wave numbers of the two consequent peaks or valleys,  $\Delta\nu_i = \nu_i - \nu_{i-1}$ , the thickness of the porous film ( $d$ ) and the effective refractive index of the porous film ( $n_{\text{eff}}$ ):

$$n_{\text{eff}} = \frac{1}{2d\Delta\nu_i} \quad (1-15)$$

Thus, by considering the consequent oscillation in the FTIR spectrum and using the equation 1-15, we reach to the dielectric coefficient of the membrane, and since we assume that the dielectric coefficient of the air is equal to 1, we reach to the refractive index of the alumina ( $n_{\text{AlOx}}$ ) through  $\epsilon_{\text{eff}}$ . In Table 1-3 we present the refractive index  $n_{\text{alox}}$  of some of our membranes. Since we observed the oscillations in the interval of  $1750$  to  $4000 \text{ cm}^{-1}$  which corresponds to the wavelengths of  $5.26$  to  $2.5 \mu\text{m}$ , we report the refractive indexes as the average of all of the refractive indexes obtained from the consequent peaks

and valleys in this interval and also the porosity of the top and bottom surface. For discussing the effects of the anodization parameters such as the voltage and the acid type and concentration, we should have in mind the value of the refractive index of the pure aluminum oxide in the literature in the same wavelength interval. For the polycrystalline aluminum oxide, Harris et al have reported the refractive index of  $1.68 \pm 0.03$  in the same wavelength interval that we have calculated the refractive index [69]. This higher value compared to the values that we have obtained arises from the crystallinity of their alumina samples while it is known that the structure of the aluminum host in the nanoporous AAO is amorphous [70], [71]. In the previous section the incorporation of the acidic anion species in the structure of the alumina was proven. Besides, we saw that by increasing the acid concentration the extent of incorporation increases as we saw more adsorption in the FTIR graph.

**Table 1-3** Refractive index of the aluminum oxide ( $n_{\text{AlOx}}$ ) of the membranes synthesized in different acid solutions calculated from the FTIR diagrams.

<b>Membrane Code Name</b>	<b>Acid Solution</b>	<b>Refractive index (<math>n_{\text{AlOx}}</math>)</b>
OA(0.05)-1	Oxalic Acid 0.05M	$1.43 \pm 0.25$
OA(0.3)-11	Oxalic Acid 0.3M (Aged)	$1.59 \pm 0.2$
OA(0.3)-14	Oxalic Acid 0.3M (Fresh)	$1.47 \pm 0.14$
OA(0.8)-1	Oxalic Acid 0.8M	$1.54 \pm 0.19$
SA(0.3)-11	Sulfuric Acid 0.3M	$1.6 \pm 0.25$
SeA(0.3)-1	Selenic Acid 0.3M (Fresh)	$1.73 \pm 0.06$
SeA(0.3)-6	Selenic Acid 0.3M (Aged)	$1.61 \pm 0.22$

The calculated refractive index values shown in Table 1-3, show a systematic trend when they are compared with the refractive index of the polycrystalline aluminum oxide which is 1.68. It shows that the refractive index of the host aluminum oxide synthesized in oxalic acid solutions, deviates more from the polycrystalline value compared to the sulfuric and selenic acid. Based on our data, we can correlate this deviation and its magnitude to the incorporation of the acids species in the aluminum oxide structure. As we can see, the refractive index of the OA(0.05)-1 can coincide with that of the pure polycrystalline alumina in the upper borders of uncertainty. And we can see that the for the

SeA(0.3)-6, the refractive index of the alumina is closer to the pure polycrystalline and we observed less contamination for this membrane in EDX analysis. In EDX analysis of both non-detached and detached membranes, we saw that the extent of the incorporation of the anionic species of the acid has the trend of oxalic>sulfuric>selenic. And we can roughly observe the same trend in Table 1-3 for the refractive index values in terms of closure to the pure polycrystalline value. Hence, in brief words we can say that the refractive index can be a criterion for evaluation the extent of incorporation of the anionic species of the acids in the host aluminum oxide structure of the AAO membranes. But, more experimental data is needed for confirming this assertion and to propose a correlation between the contamination of the aluminum oxide with anionic species of the acid and the refractive index.

## 1.5 Conclusions

In this chapter 1, we aimed at synthesizing thought hole nanoporous AAO membranes with different structural and compositional properties as a nanoporous confining medium appropriate for transverse streaming potential measurement (see Chapter 2). Structural properties are more precisely the average pore diameter, inter-pore distance, the number of the pores per unit area and the pore length. The compositional features reveal the extent of contamination of the host alumina in the nanoporous alumina membrane. To tune the structure and composition we used three different acid types (namely oxalic, sulfuric and selenic acids) and, for OA, three different concentrations. We observed the pore density to reduce with voltage and increase with the acid concentration. The diameter of the AAO membranes also showed a limited dependence on the concentration of the acid. Additionally, we went through a systematic study on the wet-etching and detachment of the membranes from the aluminum substrate as well. It was observed that the third anodization and also wet-etching become more time consuming and more complicated by decrease in the channel diameters. This observation indicates the diffusion to be the controlling mechanism in both third anodization and wet-etching. Therefore, it is favorable to expose the membrane for a shorter time to the phosphochromic solutions. Thus, until the complete dissolution of the third layer and the membrane detachment, a considerable enlargement of the pores on the top surface which is more in contact with acid is observed.

Thus, we summarize the findings of our research work in this chapter which should be taken into account in the proceeding chapters with the following points:

- 1- The pore diameter of the AAO membranes is dependent on the acid type. The average diameter of the membranes synthesized in the acids that we used in this work had the trend of oxalic acid>sulfuric acid>selenic acid. But, this trend is not valid after detachment according to the long time that selenic acid synthesized membrane remains in the phosphochromic acid solution and the pores are widened.
- 2- The through-hole AAO membranes synthesized in sulfuric acid have smaller pore diameters compared to the detached membranes synthesized in oxalic and selenic acid. These membranes have also a pore density of around 2.5 times higher than the membranes synthesized in the two other acids.
- 3- The chemical characterization of the membranes confirmed the ions incorporation in the AAO structure. The extent of incorporation and contamination depends on the acid concentration and acid the voltage. These contaminations affect the physical properties of the membranes such as the refractive index. The refractive index of the membranes shows considerable deviations from that of the pure aluminum oxide.
- 4- The elements distribution is approximately homogeneous on the membrane surface. The EDX profiles of the top, bottom and the section surfaces are similar.

Now that we have synthesized AAO with different pore  $D_p$  and composition we intend to know if it will influence the charge properties of the AAO. For this reason, we proceed to chapter 2 in which we will present a detailed study on the surface charge of the different surfaces of the AAO membranes (top, bottom, nanochannels and bulk smashed) by electrokinetic techniques.

## 2 Chapter 2: Electrical surface properties of nanoporous alumina membranes

### 2.1 Introduction

In this chapter, the surface charge of the synthesized AAO membranes will be studied on different surfaces of the membrane which are namely top, bottom, nanochannels internal surface and also on the surface of the particles produced from grinding the membrane. The isoelectric point of the mentioned surfaces is sought to be identified and the variables affecting the isoelectric point are discussed.

### 2.2 State of the art of the surface charge studies of the AAO membranes

Because of their unique structural, physical, chemical and surface properties, a wide range of scientific communities now largely employs nanoporous oxide membranes for multiple applications: biosensing [72], nanofiltration [73], nano templating [74], drug delivery [75], catalysis [76], energy storage [77]... Since most of these applications involve local phenomena at the nanochannel surface (adsorption of molecules, chemical reaction...) the fine description of the electrical surface behavior in aqueous solution is thus of primordial interest. For oxides, the existence of an electrical charge is due to the protonation/deprotonation of hydroxyl groups at the surface, which will depend on the local chemical environment. The electrical surface properties are usually quantified through the sign and amplitude of the  $\zeta$ -potential (defined as the electric potential at the hydrodynamic shear plane) and also through the point of zero charge (PZC i.e. pH at which net charge density is zero) or the isoelectric point (IEP i.e. pH at which the  $\zeta$ -potential is zero) of the materials. In Figure 2-1 a scheme of the charged solid – liquid and the different planes is depicted. In this figure, the electrical double layer formed adjacent to a negatively charged solid surface is shown. In this figure, the electrical potential is shown with the Greek letter  $\psi$ . The electrical double layer consists of two layers which are the Stern layer which is stagnant and the diffuse layer which is mobile. The inner Helmholtz plane passes through the centers of the ions that are adsorbed to the surface. The outer Helmholtz plane passes through the centers of

the hydrated ions that are configured adjacent to the inner Helmholtz layer and the charge of the majority of them is opposite to the charge of the surface.

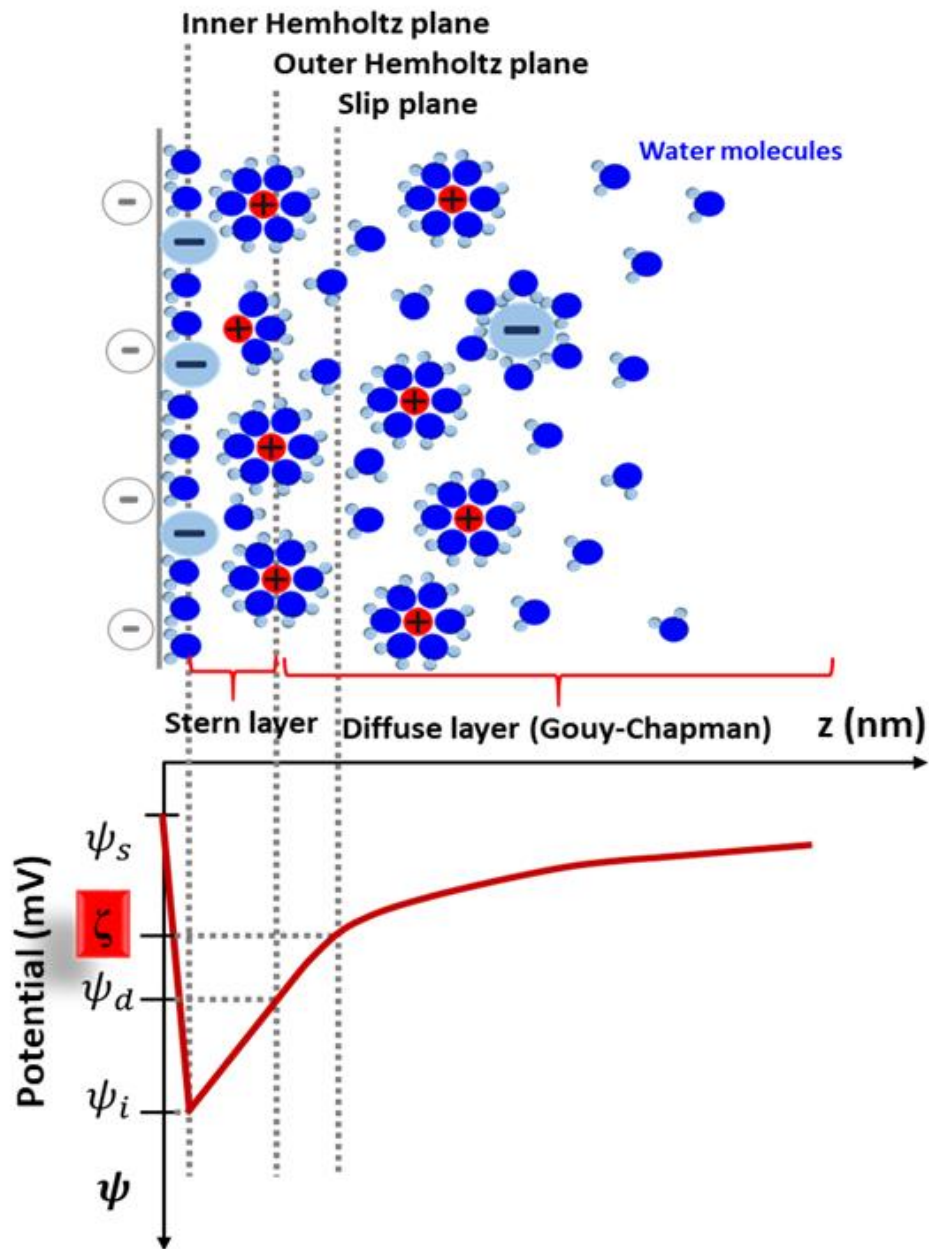


**Figure 2-1** Scheme of the electrical double layer (EDL) formed adjacent to a charged wall and the different layers and planes.

Thus, the Stern layer is the area between the inner and outer Helmholtz planes. After the Stern layer the diffuse layer starts. The hydrodynamic shear plane or the slip plane is in the diffuse layer and it is

located where the liquid starts to have normal viscous behavior compared to the liquid layer bond to the surface which shows elastic behavior [78]. The electric potential at this point is the  $\zeta$ -potential.

PZC is usually obtained by potentiometric titration (which is well adapted for colloidal particles) while IEP is obtained by electrokinetic techniques (streaming current or potential, electro-osmosis) more suitable for nanoporous materials (note that IEP and PZC match when there is no specific ion adsorption at the surface) [79]. Electrokinetic data interpretations rely on electrokinetic theories to determine the  $\zeta$ -potential assuming that the probed surface is planar, ideal (i.e. smooth), nonporous and rigid (i.e. contrary to “soft”). Any deviations from these hypothesis might modify the relationship between the measured values and the  $\zeta$ -potential and consequently the IEP of the surface [80], [81].

Among the classical nanoporous oxide membranes, anodic aluminum oxide (AAO) membranes are largely used and very interesting nanoporous model systems. Literature survey clearly shows the wide interest of these nanoporous systems for the various applications already mentioned above because of their pore morphology, pore density and surface properties [82]. As discussed with details in chapter 1, AAOs are synthesized by a two-step anodization process in an acidic electrolyte that leads to the formation of non-connected, parallel and ordered nanochannels whose characteristic sizes and composition can be finely tuned through the anodization experimental parameters (voltage, nature and concentration of the electrolyte, temperature...) [35], [83]. Typical channel diameter ranges from 10 nm to 200 nm with a narrow size distribution, the channel length can reach up to 100  $\mu\text{m}$  and the pore density can vary from  $10^9$  to  $10^{11}$  pores/ $\text{cm}^2$ , providing selectivity, mechanical stability and interesting high flow rate to AAO membranes. In term of composition, AAOs are heterogeneous: they are made of amorphous alumina ( $\text{Al}_2\text{O}_3$ ) with “contaminants” coming from the electrolyte used during the anodization (for instance oxalate ions when using oxalic acid (OA) or sulfate ions with sulfuric acid). Their quantities mainly depend on the electrolyte concentration and anodization voltage [35]. More precisely, it has been observed that the AAO cell is composed of two regions with different composition: one “contaminants”-rich area whose extent will depend on the “contaminants” nature (the smaller such as sulfates will diffuse deeper within the cell) and one alumina-rich area. These anion contaminations have impacts on the AAO optical properties (refractive index, photoluminescence) but there were no attempts so far to investigate its effects on the AAO electrical surface properties. Two of the most well-known methods for investigating the electrical surface properties are the electrokinetic measurements of streaming potential and streaming current which are described and formulated thereafter.

## 2.3 Streaming potential (SP) and streaming current (SC) experiments

AAO electrical surface properties are primarily investigated by electrokinetic techniques, mostly streaming current or potential experiments. Streaming experiments (SE) can be performed by applying a pressure gradient along the AAO outer surface (tangential SE) or through the AAO nanochannels to probe the inner surface (transverse SE). So far studies have been carried out on homemade or commercial AAOs primarily assuming that both inner and outer surfaces behave similarly, i.e. without combining both transverse and tangential SE. At this point we present the theoretical basis of these interrelated techniques before presenting the literature survey on the results of the other researchers from these techniques.

In contact with aqueous electrolyte solution the AAO hydroxyl surface groups undergo protonation/deprotonation process responsible of a surface charge that is compensated by the presence of ions to ensure electroneutrality. An electrical double layer (EDL), consisting of an immobile Stern layer and a mobile diffuse layer, is formed adjacent to the charged surface. When a pressure gradient is applied, the ions in the diffuse layer are displaced with the fluid and an electrical streaming current ( $I_s$ ) arises and comes with an electrical streaming potential ( $U_s$ ) [81]. Assuming that the surface conductivity is neglected and the  $\zeta$ -potential of the surface is low, the transport phenomenon through the nanochannels can be formulated by irreversible thermodynamics with the equations 1 and 2 which take into account the two thermodynamic forces that lead the flow which are namely the electric field gradient  $\Delta E$  and the pressure gradient  $\Delta P$  [84]:

$$J_V = L_P \Delta P + L_{EP} \Delta E \quad (2-1)$$

$$I = L_{EP} \Delta P + L_E \Delta E \quad (2-2)$$

In these equations,  $J_V$  is the volume flux passing through the nanochannel,  $I$  is the electric current,  $L_P$  is the hydraulic permeability,  $L_E$  is the electric conductance and  $L_{EP}$  is the nondiagonal phenomenological coefficient which is responsible for the electrokinetic phenomena.  $L_{EP}$  is referred as the electroosmotic permeability in some cases. In these equations, Onsager's symmetry relationship is taken into account [84]. We intend to use the equations 2-1 and 2-2 to describe the streaming current and the streaming potential. Depending on the initial and boundary conditions, these two correlations can describe a variety of transport phenomena.

Once a charged nanochannel is filled with electrolyte solution, an electrical double layer (EDL) is formed adjacent to the nanochannel wall. By applying a pressure gradient between the two ends of a nanochannel, the fluid will flow and this convective flow causes some ions of the diffuse layer of the EDL to displace in the direction of fluid flow. In case there is no potential gradient between the two ends, this movement of ions lead to a current which is called streaming current ( $I_S$ ):

$$I_S = L_{EP}\Delta P \quad (2-3)$$

The convective flow of ions towards one end of the nanochannel, causes a potential gradient between the two ends. This potential gradient causes a conductance current in the opposite direction in the nanochannel which leads to a stationary state when the convective current is equal to the conductance current and the net electric current is zero. The potential gradient in the equality of convective and conductance current is considered as the streaming potential ( $\Delta E_S$ ). By setting  $I=0$  in correlation 2-2, we can obtain the streaming potential:

$$\Delta E_S = -\frac{L_{EP}}{L_E}\Delta P = -\frac{I_S}{L_E} \quad (2-4)$$

At this step, once we obtain an equation for  $I_S$ , we will be able to present an equation for the streaming potential as well according to the fact that the streaming potential is measured once the streaming current is cancelled out with a convective current with the same magnitude and opposite direction:

$$I_C = -I_S \rightarrow \Delta E_S(\text{maintaining } I_C) = U_{str} = I_C Z = -I_S Z$$

where  $Z$  is the impedance of the channel through which we have the flow. Impedance is the resistance of the path against the electric flow. It is the inverse of the conductance of the channel which is correlated to the dimensions and the specific conductivity ( $\sigma$ ) of the electrolyte filling the channel with equation 2-5:

$$Z = \frac{L}{A\sigma} \quad (2-5)$$

In the presented equations we can observe that it is possible to convert the streaming current to the streaming potential by deviding the streaming by the impedance of the channel with a reverse sign. At this step we will go through a detailed derivation of the Helmholtz-Smoluchowski correlations. We will formulize the electric current in the case of lack of electric field ( $I_s$ ) as follows. Figure 2-2 shows schematically a capillary path through which the streaming current passes. The origin of the coordinates is considered in the middle of the channel:

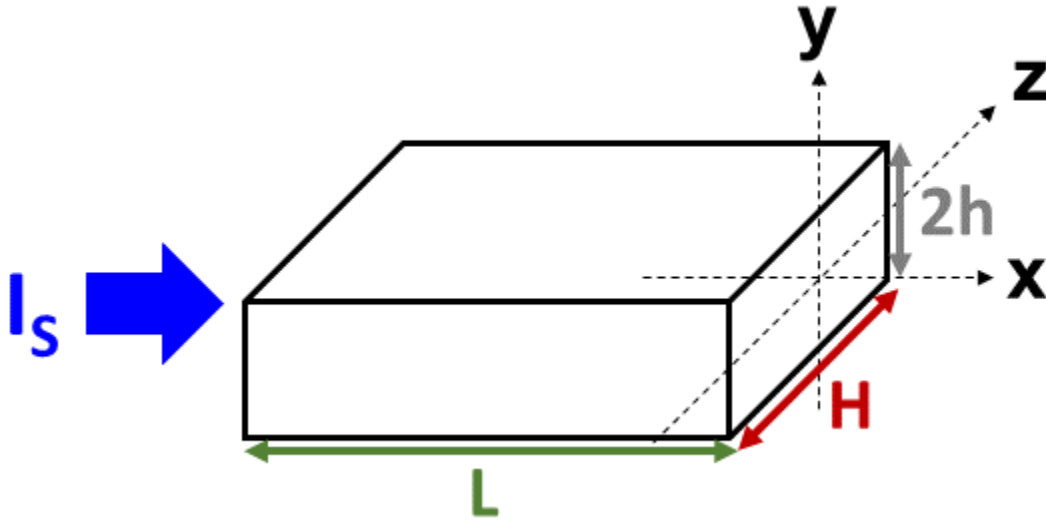


**Figure 2-2** Scheme of the channel through which the streaming current passes

In the presented equations,  $L$  is length of the channel in which flow occurs and  $A$  is the channel surface area perpendicular to the flow;  $\sigma$  is the specific conductivity of the electrolyte solution;  $\eta$  is the viscosity of the electrolyte solution and is considered same as that of water;  $\epsilon$  is the permittivity of the electrolyte solution that is also approximated, as the relative permittivity of water multiplied by  $\epsilon_0$  which is the vacuum permittivity ( $\epsilon = \epsilon_{r(water)} \cdot \epsilon_0$ ).

The current passing the channel surface cross section can be calculated by multiplying the volume flow ( $u = v \cdot A$ ) by the charge density ( $\rho_e$ ). By looking at the rectangular cross-section of the channel, we consider the charge density  $\rho(y)$  and the velocity  $v(y)$  to be functions of the coordinates inside the cross-section plane which are namely  $y$  and  $z$ . Besides, we consider their profiles to be symmetric with respect to  $x$ - $y$  and  $x$ - $z$  planes. Which means that  $\rho_e(y, z) = \rho_e(-y, z) = \rho_e(y, -z) = \rho_e(-y, -z)$ .

This is the same for the velocity profile. Hence we can integrate the flow elements in one quarter of the cross-section plane and multiply it by 4:

$$I_S = 4 \int_0^h \int_0^{\frac{H}{2}} v(y, z) \rho_e(y, z) dy dz \quad (2-6)$$

By considering the width of the channel to be highly larger the height ( $H \gg 2h$ ), we neglect the variation of the velocity and the charge density over  $z$ , thus the integral becomes single by considering  $2 \int_0^{H/2} dz = H$  and assuming that the charge density satisfies Poisson equation ( $\frac{d^2 \phi}{dy^2} = -\frac{\rho_e(y)}{\epsilon}$ ):

$$I_S = 2H \int_0^h v(y) \rho_e(y) dy = -2\epsilon H \int_0^h v(y) \phi''(y) dy \quad (2-7)$$

At this point, we will find the velocity profile  $v(y)$ , by the flow analysis of an incompressible fluid between two parallel plates in steady state which is equivalent to the geometry that we are considering ( $H \gg 2h$ ). The scheme of the flow and the volumetric element taken for the differential force balance are shown in Figure 2-3.

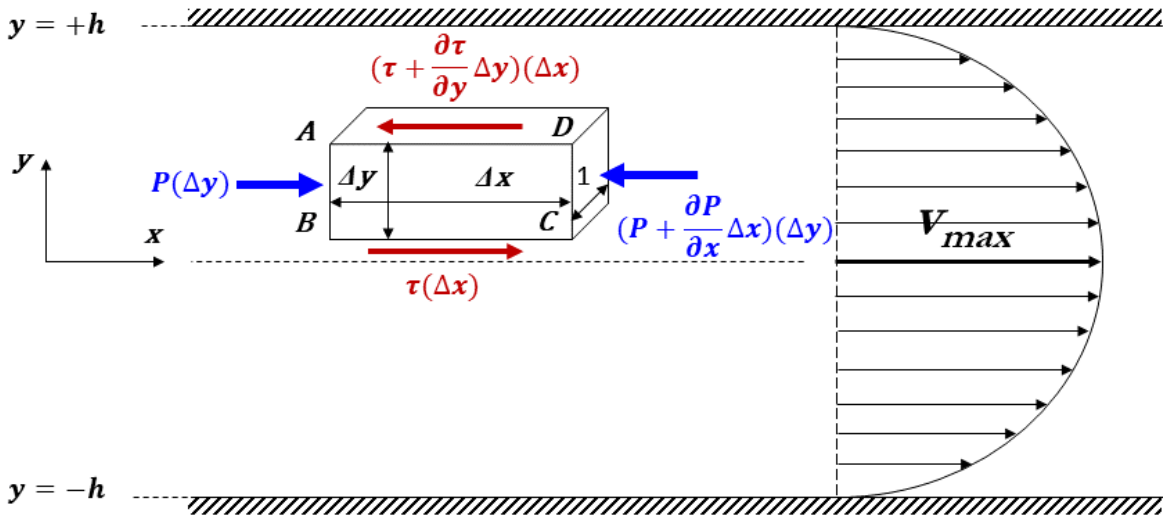


**Figure 2-3** Scheme of the flow of an incompressible fluid between two parallel plates and the volumetric element on which the forces balance is studied.

We can see that the fluid flows along the x axis. The volumetric element considered has the dimension of  $\Delta x$  along the x axis,  $\Delta y$  along the y axis and unity (1) in the z axis perpendicular to the page. The origin of the coordinates is considered to be placed at the middle of the two plates. Since we assume the flow to be in steady state, we have:

$$\sum F_x = 0$$

$$P(\Delta y) - \left(P + \frac{\partial P}{\partial x} \Delta x\right) (\Delta y) + \tau(\Delta x) - \left(\tau + \frac{\partial \tau}{\partial y} \Delta y\right) (\Delta x) = 0$$

Since it is assumed not to have velocity gradient in z direction ( $\frac{\partial v}{\partial z} = 0$ ), there is no shear stress acting on ABCD plane and the plane parallel to it on the element.

$$\begin{aligned} \rightarrow -\frac{\partial P}{\partial x} \Delta x \Delta y - \frac{\partial \tau}{\partial y} \Delta y \Delta x &= 0 \\ \rightarrow \frac{\partial \tau}{\partial y} &= -\frac{\partial P}{\partial x} \end{aligned}$$

We know that for the incompressible fluids, the shear stress ( $\tau$ ) is correlated to velocity gradient ( $\partial v / \partial y$ ) by viscosity ( $\eta$ ) as a coefficient  $\tau = \eta \frac{\partial v}{\partial y}$ . Thus:

$$\frac{\partial}{\partial y} \left( \eta \frac{\partial v}{\partial y} \right) = -\frac{\partial P}{\partial x} \quad \xrightarrow{\text{incompressible and isotropic fluid}} \quad \frac{\partial^2 v}{\partial y^2} = -\frac{1}{\eta} \frac{\partial P}{\partial x}$$

Integrating this correlation twice with respect to y gives:

$$v(y) = -\frac{y^2}{2\eta} \frac{\partial P}{\partial x} + C_1 y + C_2$$

One of the boundary conditions is the derivative of the velocity with respect to the y axis in the middle of the two plates is equal to zero. Because this point is an extremum point for the velocity which gains its maximum value. Hence:

$$\frac{\partial v}{\partial y} \Big|_{y=0} = C_1 = 0$$

Another boundary condition is adjacent to the planes ( $y = \pm h$ ) where the velocity should be zero due to the no slip condition. Thus:

$$v(+h) = v(-h) = -\frac{h^2}{2\eta} \frac{\partial P}{\partial x} + C_2 = 0 \quad \rightarrow \quad C_2 = \frac{h^2}{2\eta} \frac{\partial P}{\partial x}$$

At last by substitution of  $C_2$  in the correlation and some simplifications we obtain equation 2-8 as the velocity profile of the incompressible fluid flowing between two parallel plates in the steady state:

$$v(y) = \frac{h^2}{2\eta} \frac{\partial P}{\partial x} \left(1 - \frac{y^2}{h^2}\right) \quad (2-8)$$

Now we expand the integral in equation 2-7 and use the boundary conditions to reach to the electric current correlation. For the right hand integral, we should integrate twice by part:

$$\begin{aligned} -2\varepsilon H \int_0^h v(y) \varphi''(y) dy &= -2\varepsilon H \left( v(y) \varphi'(y) \Big|_{y=0}^{y=h} - \int_0^h v'(y) \varphi'(y) dy \right) \\ &= -2\varepsilon H \left( v(y) \varphi'(y) \Big|_{y=0}^{y=h} - \left( v'(y) \varphi(y) \Big|_{y=0}^{y=h} - \int_0^h v''(y) \varphi(y) dy \right) \right) \\ &= -2\varepsilon H \left( v(h) \varphi'(h) - v(0) \varphi'(0) \right. \\ &\quad \left. - \left( v'(h) \varphi(h) - v'(0) \varphi(0) - \int_0^h v''(y) \varphi(y) dy \right) \right) \end{aligned}$$

For reaching to the final value of this integral, we need these boundary and initial conditions:

- We consider the thickness of the EDL to be negligible, thus the place of the slip plane is approximately in  $y = h$ . At this point:  $\varphi(h) = \zeta$ . From equation (2-8), we can see that  $v(h) = 0$  and  $v'(h) = -(\Delta P/L)(h/\eta)$  if we consider the  $\frac{\partial P}{\partial x} = cte = \frac{\Delta P}{L}$ .
- In the origin of the coordinates in the middle of the channel ( $y=0$ ) we have:  $v'(0) = 0$ .
- $\eta v''(y) = -\Delta P/L$ .

Thus with substitution of the boundary conditions we have:

$$\begin{aligned}
 I_s &= -2\varepsilon H \left( v'(0)\varphi(0) - v'(h)\varphi(h) + \int_0^h v''(y)\varphi(y)dy \right) \\
 &= -2\varepsilon H \left( -\left(-\frac{\Delta P h}{L \eta} \zeta\right) + \int_0^h -\frac{\Delta P}{L \eta} \varphi(y)dy \right) = -\frac{2\varepsilon H h \Delta P}{L \eta} \left( \zeta - \frac{1}{h} \int_0^h \varphi(y)dy \right)
 \end{aligned}$$

Since the electric potential far from the slip plane is considered to be zero, and we have considered the EDL thickness to be negligible compared to the width of the channel,  $\int_0^h \varphi(y)dy \approx 0$ . Thus, by rearrangement of the correlation for  $\zeta$  we reach to equation 2-9 for correlating the streaming current to zeta potential:

$$\zeta = -\frac{\eta L I_s}{\varepsilon A \Delta P} \quad (2-9)$$

Now, according to equation 5, we can present a correlation for converting the streaming potential to zeta potential as shown in equation 10:

$$\begin{aligned}
 U_{str} &= -I_s Z = -\left(-\frac{\zeta \varepsilon A \Delta P}{\eta L}\right) \left(\frac{L}{A \sigma}\right) = \frac{\zeta \varepsilon \Delta P}{\sigma \eta} \\
 \zeta &= \frac{\sigma \eta U_{str}}{\varepsilon \Delta P} \quad (2-10)
 \end{aligned}$$

These Helmholtz-Smoluchowski equations are used in this research work for converting the streaming current (equation 2-9) and streaming potential (equation 2-10) to zeta potential. Each of these equations shows its own advantage for determining the zeta potential. In Equation 2-10, knowing the geometry of the channel in which we measure the zeta potential is not necessary to extract this zeta potential while it requires knowing the specific conductivity of the electrolyte solution. In equation 2-9, the geometry of the channel should be known while there is no need for the conductivity of the electrolyte. We presented the assumptions made for reaching to these equations. In case of deviation from the ideal conditions, it is possible to change the variables like the conductivity (considering the

surface conductivity), velocity profile, ionic density and also EDL thickness and solve the differential equation numerically. Here, two different experimental modes with different channel geometries were used to measure  $I_s$  and/or  $U_s$ .

Streaming experiments (SE) are either performed by applying a pressure gradient along the AAO top or bottom outer surfaces (tangential mode) or through the AAO nanochannels to probe the inner surface (transverse mode); see Figure 2-4.

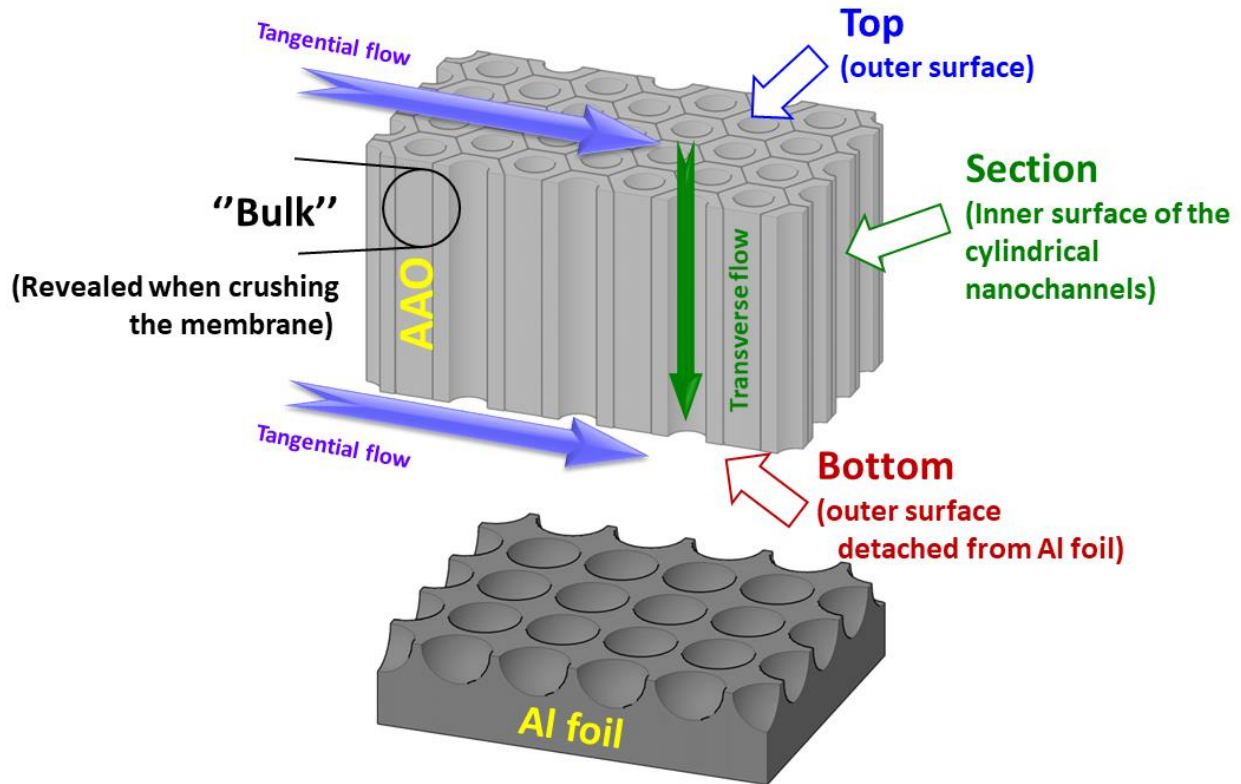


**Figure 2-4** Schematic representation of the AAO membrane obtained after detachment from the Al foil. The different surfaces investigated by electrokinetic experiments are shown (top and bottom outer surfaces, pore wall surface and surface created after the grinding).

Tangential SE are carried out at room temperature with a SurPASS instrument (Anton Paar GmbH). In this mode, the channel geometry is made of two identical AAO pieces ( $S = 1 \text{ cm} \times 1 \text{ cm}$ ) facing each other with a variable and tunable gap distance  $b$ . The two AAO pieces were mounted with double-adhesive tape on the two surfaces of the SurPASS adjustable-gap cell. The surfaces gap distance  $b$  is determined by flow measurements using the Hagen-Poiseuille formula and adjusted by a micrometric screw. In all our tangential SE the typical gap distance is fixed at an average value of  $89 \pm 7 \text{ }\mu\text{m}$ . The

electrolyte solution is circulated back and forth through the cell with two syringe pumps. The pH and conductivity are continuously monitored. All experiments are carried out with 100 mM KCl solution, setting the solution conductivity to 12.2 mS/cm and giving a Debye length  $\lambda_D$  of around 1 nm (fulfilling the conditions to apply eq. 2-9 and 2-10). The pH of the electrolyte solution is modified by adding small amounts of concentrated HCl or KOH solutions. A pair of Ag/AgCl electrodes is used to measure both  $I_s$  and  $U_s$  and four streaming measurements are performed (corresponding to two “back and forth” measurements). A typical set of raw data ( $I_s$  versus  $P$ ) is shown in Figure 2-5.

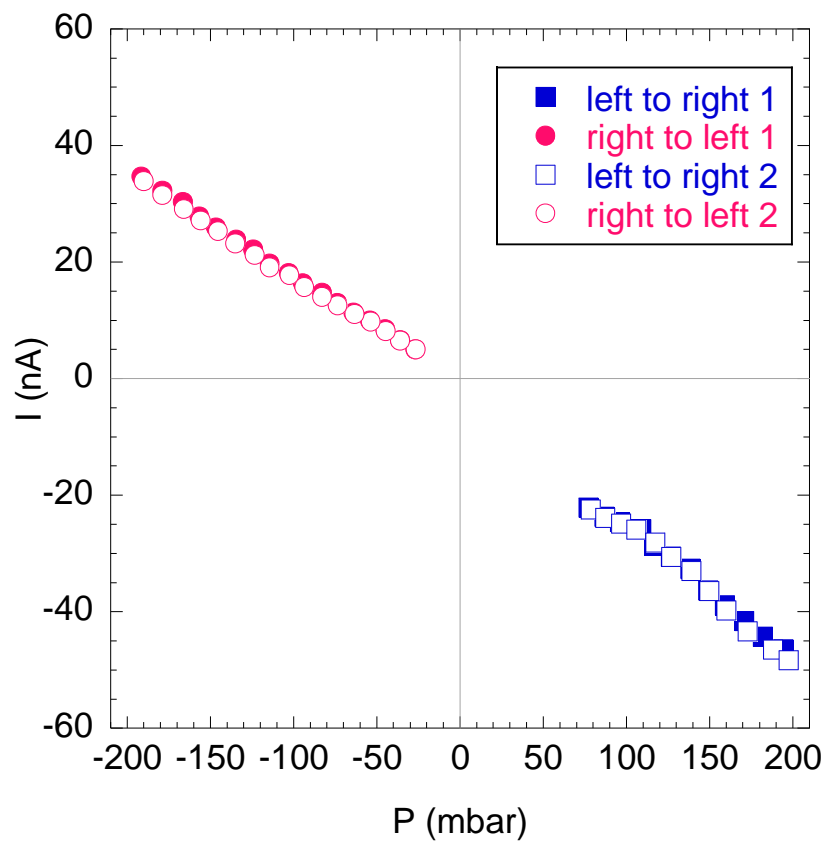


**Figure 2-5** Raw P-I graph of tangential flow streaming current measurement on the top surface of the OA(0.8)-2 AAO membrane at pH=10.4. The measurement composes of four steps: two from left to right (blue) and two in the opposite direction (red) flow.

The  $\zeta$ -potential obtained by  $I_s$  or  $U_s$  are similar (see Figure 2-6). The AAO membranes are first measured in pure KCl solution at pH around 6 and the  $\zeta$ -potential is negative. To ensure that the AAO surfaces are not contaminated by impurities, the pH is thus directly adjusted to a high value (pH around 10) and then decreased stepwise down to around 3 and the  $\zeta$ -potential is measured for each pH.

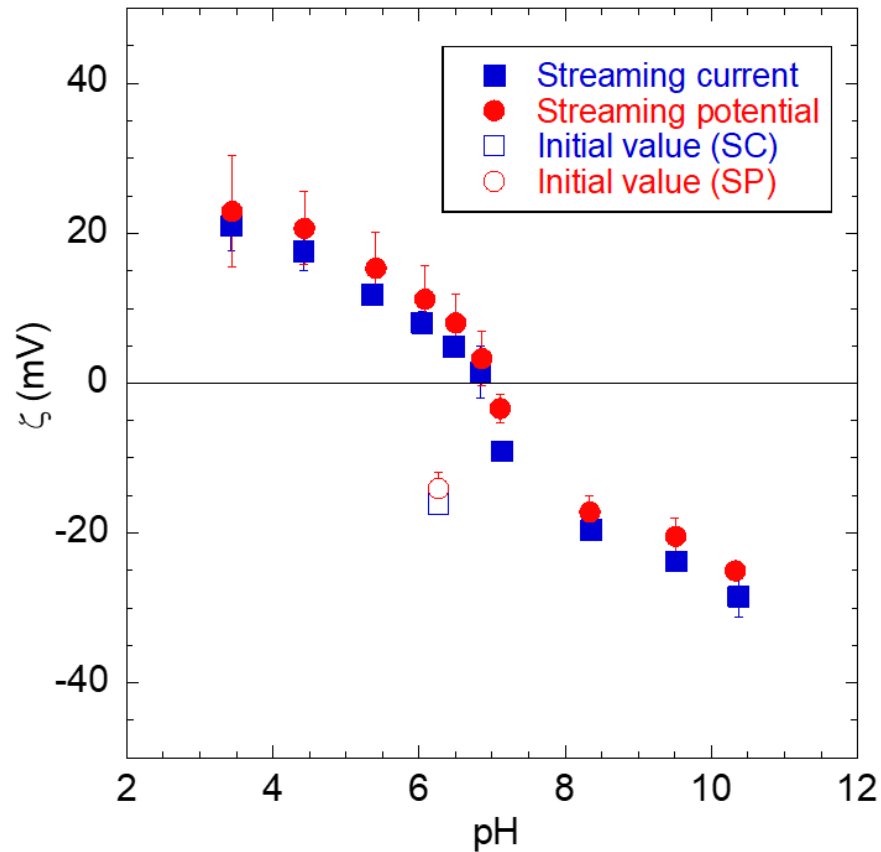


**Figure 2-6** Comparison between the  $\zeta$ -potential values derived from the streaming current  $I_s$  (blue square) and streaming potential  $U_s$  (red circles) obtained by tangential SE. The measurement cycle was carried out on the bottom side of the OA(0.8)-2 AAO membrane. The empty symbols show the first measurement in pure KCl solution at pH=6.3. The initial negative value suggests that the AAO surface is contaminated by impurities. To wash away and desorb these impurities, the pH is directly adjusted to a high value (pH around 10) and then decreased stepwise down to around 3 and the  $\zeta$ -potential is measured for each pH.

In order to study the pore wall surfaces inside the channels, the streaming potential across the membrane is measured, applying a difference of pressure on both sides. These transverse SE are performed at room temperature with a homemade device composed of two compartments filled with 100 mM KCl solution separated by the AAO membrane (note that in this mode the probed channel geometry is directly the AAO nanochannel). The instrument is built and developed by Dr. Didier Lairez at Laboratoire des Solides Irradiés, École Polytechnique. The picture of the instrument is shown in Figure 2-7 in both dismantled and assembled status.

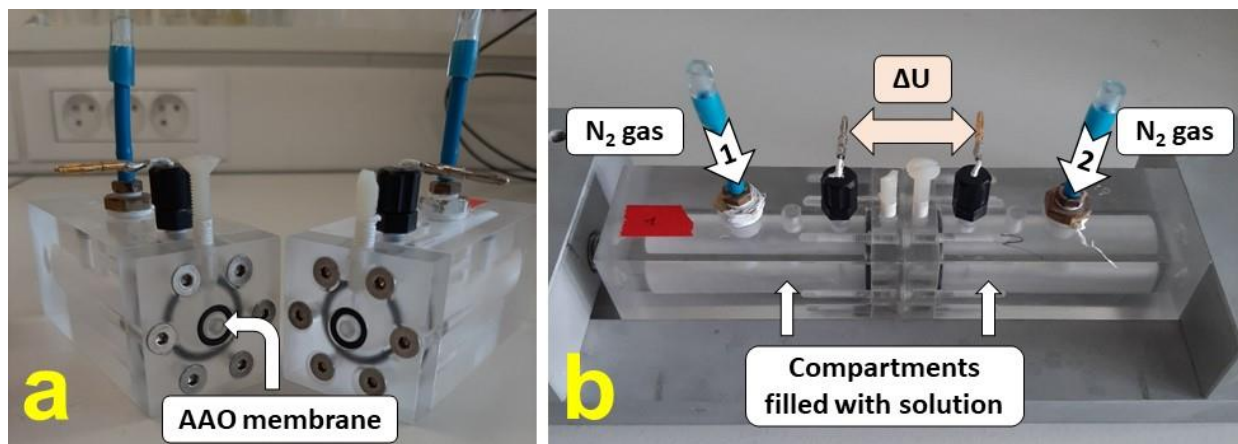


**Figure 2-7** The homemade transverse streaming potential measurement instrument in **a)** dismantled and **b)** assembled status. The setup is built and developed by Dr. Didier Lairez at Laboratoire des Solides Irradiés, École Polytechnique.

An Ag/AgCl electrode is immersed in each compartment to measure  $U_s$  and the pressure is alternatively applied from one compartment to another by electrovalves with a given frequency of 0.2 Hz. One measurement consists of a “back and forth” cycle of 5 s (see Figure 2-8) from which  $dU_s/dP$  is extracted and then converted into  $\zeta$ -potential according to eq. 2-10. The first measurement is also performed in pure KCl solution and here a positive  $\zeta$ -potential is measured. As the tangential SE, the pH is then adjusted to high value and followed by stepwise pH lowering down to around 3. For each pH, the cycle is repeated during 10 min or 1 h to obtain an average  $\zeta$ -potential (see Figure 2-9).

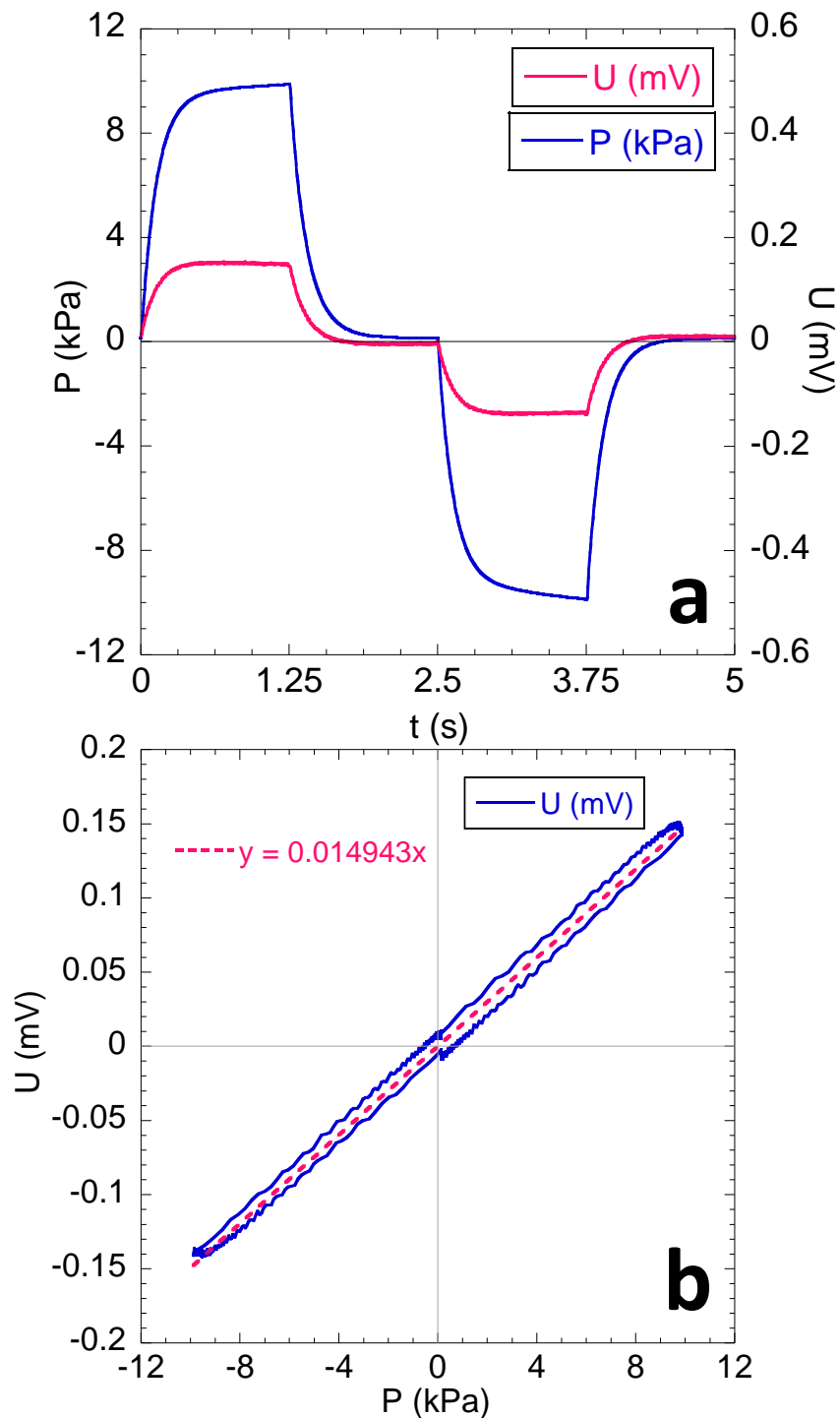


**Figure 2-8** Raw data of the transverse SE for one “back and forth” cycle: a) pressure  $P$  and the resulting voltage  $U$  as a function of time b)  $U$  vs  $P$  diagram with the corresponding linear fit. The slope of the fit yields the  $dU/dP$  that is then converted to the  $\zeta$ -potential. The membrane is OA(0.3)-14 and the  $pH \approx 6$ .

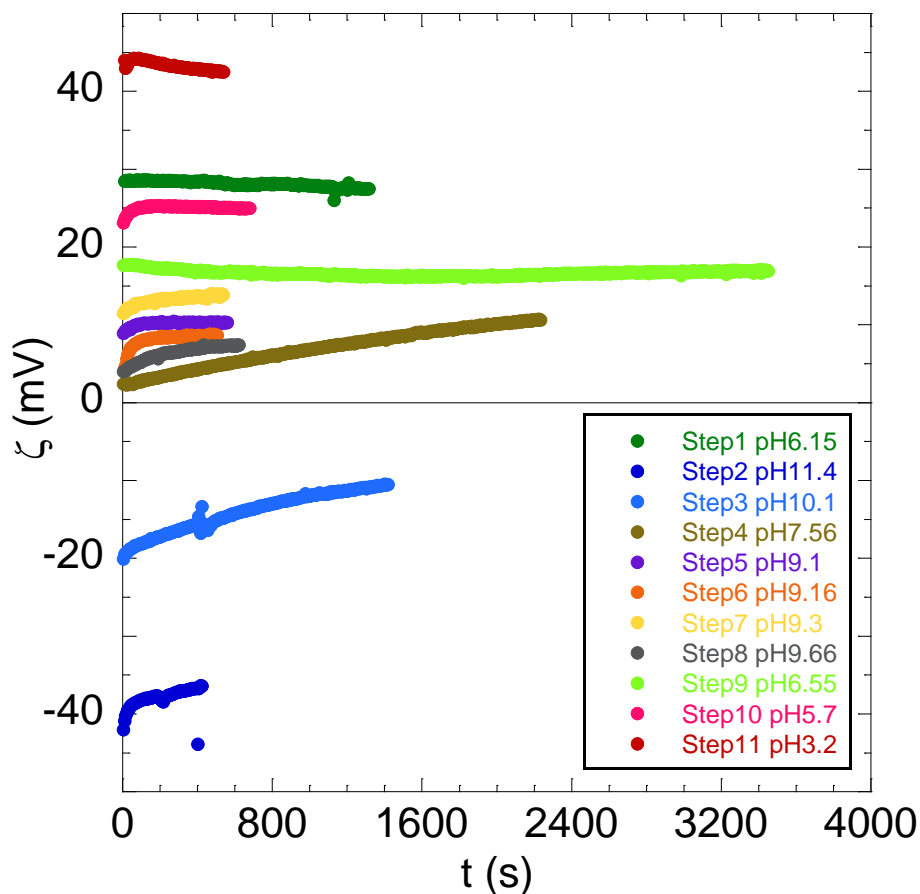


**Figure 2-9**  $\zeta$ -potential obtained by transverse SE as a function of time at different pHs for OA(0.8)-2 AAO membrane.

In literature, both techniques have been used in few studies however never on the same samples. The results show that IEPs range from 6.7 to 7.9 by using tangential SE [85] while higher IEPs are found by transverse SE (from 8 to 10) [86]–[88]. Moreover, a recent work using electrophoretic mobility (EM) experiments on crushed AAO in KCl solution found IEPs of 4.6, 5.3 and 6 for AAOs synthesized in phosphoric, oxalic or sulfuric acid, respectively [89]. Additionally, another technique using electron paramagnetic resonance can also probe the inner surface and lead the determination of an effective PZC around 5 for AAOs synthesized under different conditions and with variable pore  $D_p$  [90], [91]. For comparison, plain aluminum oxides (including the different crystallographic forms) or aluminum hydroxides ( $AlOOH$  and  $Al(OH)_3$ ) have typical IEPs comprised between 8 and 11 [92]).

These previous works showed that, depending on the technique used, the type of AAOs and the nanochannel morphology ( $D_p$ ), a large range of IEPs is found (from 4.6 to 10), suggesting that the probed surfaces might be different. The origins of these differences can be multiple:  $\lambda$ ) modification in

the local chemical environment (coordination [85], density of active sites, chemical surface heterogeneities, preferential adsorption) or *ii*) modification of the electrical double layer (EDL) structure induced by the surface morphology. For the latter, the influence of curvature or roughness has not been considered for AAO but could also explain the IEP differences [93]. However, with the current results, it is impossible to decorrelate these multiple factors since no systematic studies have been performed to differentiate them on the different surfaces.

## 2.4 Electrophoretic mobility (EM) experiments

Electrophoretic mobility measurements can also provide the  $\zeta$ -potential value of AAO when the sample is formulated as particles suspended in aqueous solution. To obtain AAO particles, around 1 mg of AAO membrane are crushed manually in a mortar and further dispersed in 2 mL of 100 mM KCl solution. The suspensions are not stable in time, indicating a large range of particle sizes, the biggest ones rapidly sediment. The volume size distribution of the AAO particles in solution is thus determined by combining complementary techniques. First, laser granulometry that can provide sizes from the microns up to few millimetres is performed using the Mastersizer 3000 (Malvern Instruments) on the suspension under a constant stirring of 500 rpm. Additionally, Dynamic Light Scattering (DLS) has been performed with a Vasco KIN (Cordouan Technologies, laser wavelength of 638 nm with a detection angle of 170°) on a suspension without stirring in which bigger objects will sediment with time making the sizes of smaller objects measurable. Finally, SEM has also been conducted on the crushed AAO powder deposited on a carbon tape.

Then, EM are performed using the ZetaSizer NanoZS (Malvern Instruments) at 20 °C following the same pH variation cycle than the SP experiments. The pH is adjusted by adding small volumes of concentrated KOH or HCl solutions and is measured before and after the EM measurements. When the pH is stable, three measurements made of three runs are performed by pH value to obtain an average  $\zeta$ -potential.

## 2.5 The aims of the current research work

The structural and compositional studies of our membrane were discussed in details in chapter 1. As it was shown in the preceding chapter, the final structural morphology (pore diameter  $D_p$ ,

interpore distance  $D_{\text{int}}$ , length  $L_p$ , pore density) and composition of AAO membranes are a consequence of a complex interplay between different experimental parameters used during the anodization: voltage, temperature, nature and concentration of the electrolyte and anodizing time. Thus, by varying these parameters, one can tune the AAO structure and composition. Hereby, we intend to investigate the influence of the tuned features of AAO on their electrical surface properties.

In this context, we aim here to investigate the effect of curvature, roughness and composition on the electrical surface properties ( $\zeta$ -potential and IEP) of AAOs synthesized with three different electrolytes (OA with variable concentration, sulfuric acid and selenic acid, both at a fixed concentration of 0.3 M) in order to tune the composition and the diameter  $D_p$  of the nanochannels. We will use an original experimental approach combining both tangential and transverse SE on the membranes as well as EM experiments on the crushed membranes to probe all the different surfaces available in AAOs: outer surfaces (top and bottom planes), pore wall surfaces and surfaces created by the grinding of the AAOs. Such approach, never used previously, and applied here on AAO membranes can further help to clarify the electric surface behavior of various systems since it can be used for different types of nanoporous membranes (organic or inorganic).

Here, we can now correlate them by comparing the different samples in order to *i*) study the effect of contaminants amount at constant  $D_p$ , *ii*) study the effect of the electrolyte nature at constant contaminants amount and constant  $D_p$ , *iii*) study the effect of pore  $D_p$  at constant contaminants amount. In the following the AAO electrical surface properties are investigated by combining several electrokinetic experiments to probe all the AAO surfaces: tangential SE for the top and bottom outer surfaces, transverse SE for the inner nanochannel surface and EM for “bulk” surfaces.

## 2.6 Electrical surface properties of AAO membranes

### 2.6.1 IEPs of the different probed surfaces: outer, pore wall and ground surfaces.

Figure 2-10 shows the  $\zeta$ -potential evolution as a function of pH for OA(0.8)-2 AAO membrane measured by transverse SP, tangential SC and EM experiments. From these curves the IEPs of the different probed surfaces, i.e. the pH at which the  $\zeta$ -potential is zero, can be determined.

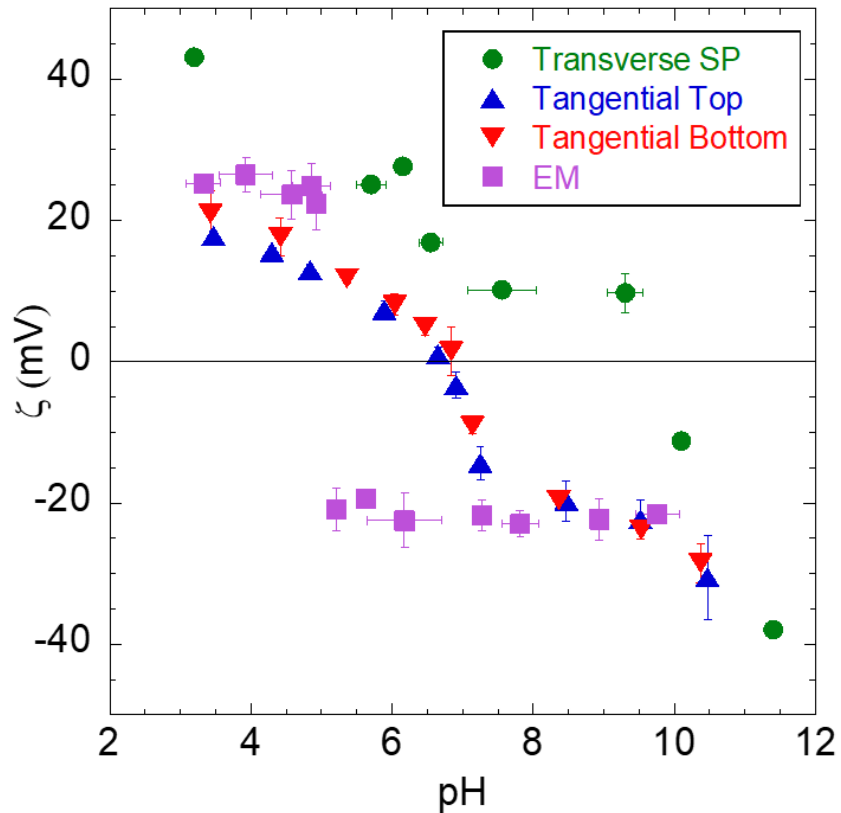


**Figure 2-10**  $\zeta$ -potential evolution as a function of pH for OA(0.8)-2 AAO membrane measured by transverse SP (green circles), by tangential SC on the top (blue triangles) and bottom (red triangles) surfaces, and by electrophoretic mobility (EM) on the powdered AAO (purple squares).

One finds IEP of 6.7, 6.9, 9.8 and 5.1 for outer top, outer bottom, pore wall and ground surfaces, respectively. The transition from positive to negative is continuous for tangential SE while it is sharp for EM. Moreover the positive and negative  $\zeta$ -potentials are similar in absolute value for both cases (between 20 - 25 mV). For transverse SE, the transition is also continuous but with higher absolute  $\zeta$ -potential values (up to 40 - 45 mV) and the negative plateau is not reached because of the high IEP. Besides, the top and bottom outer surface present a similar IEP ( $\approx 7$ ), which is quite different from the pore wall surface ( $= 9.8$ ) and the ground surface ( $= 5.1$ ). Thus, a clear change in IEPs (above 1 pH unit) is observed depending on the surface probed:  $IEP_{\text{bulk}} < IEP_{\text{outer}} < IEP_{\text{inner}}$ . In the following, we propose to investigate the possible origins of the different IEPs by decoupling the various effects with our different synthesized AAOs described above.

## 2.6.2 Influence of the amount and nature of “contaminants” within AAOs.

First we will focus on the effect of contaminants (oxalates) content. As mentioned previously, by changing the OA concentration, AAOs present similar  $D_p$  (13 % difference) but large variations in oxalates content (from 0.08 to 0.025, around 70 % difference), especially between 0.05 M and 0.8 M. Figure 10 shows the evolution the  $\zeta$ -potential as a function of pH for OA(0.05), OA(0.3) and OA(0.8) AAO membranes for the top outer (Fig. 2-11a) and bottom outer surfaces (Fig. 2-11b), the pore wall surface (Fig. 2-11c) and the ground surface (Fig. 2-11d) and the Table 2-1 provides the IEPs values. Small variations ( $< 1$  pH unit) are observed for the outer (tangential top and bottom) and pore wall (transverse) surfaces when changing the oxalates amount: IEPs range from 6.4 to 7.1, from 6.1 to 6.9 and from 9.2 to 9.8 for the top, bottom and pore wall surfaces, respectively.

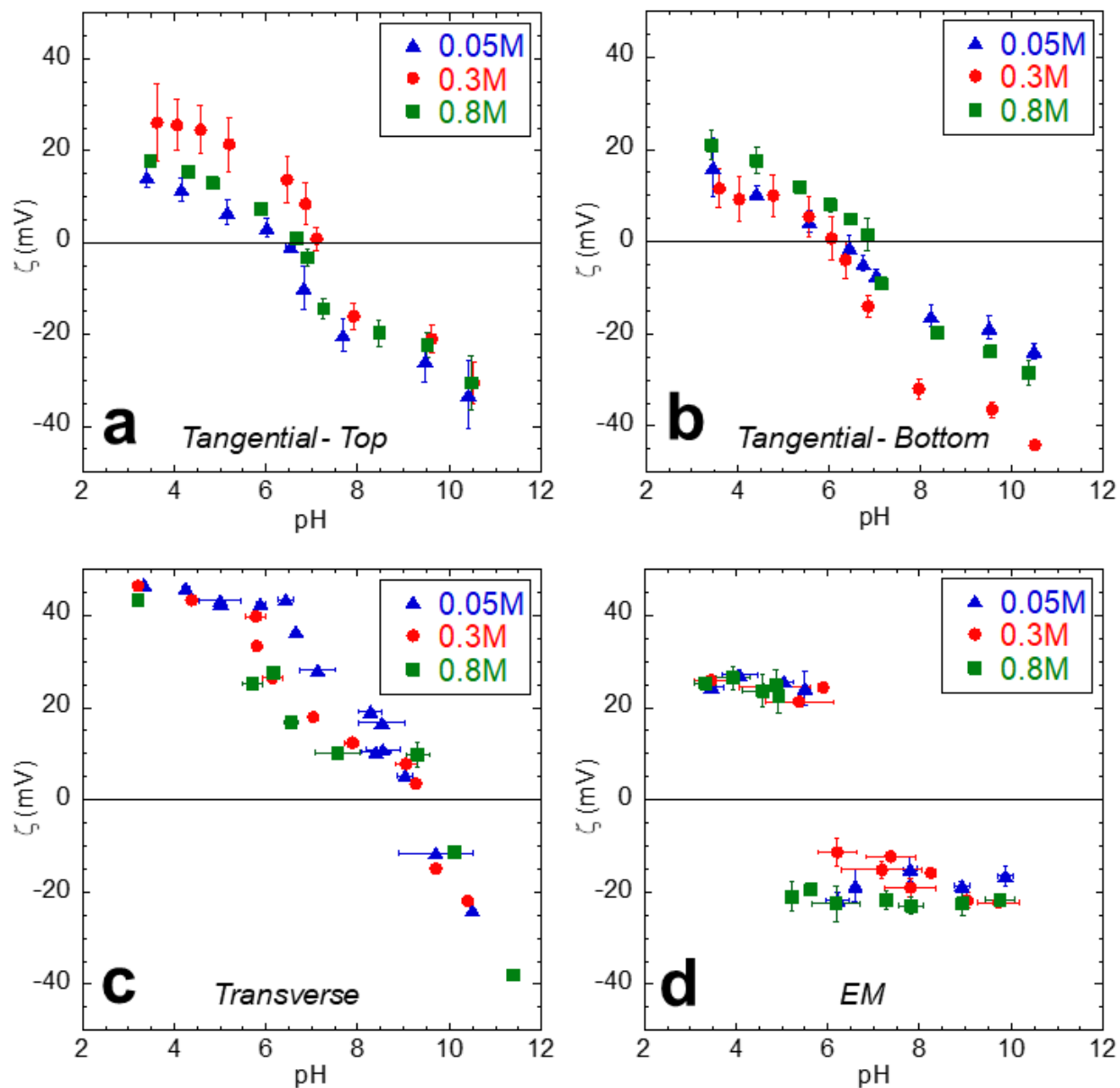


**Figure 2-11**  $\zeta$ -potential evolution as a function of pH for OA(0.05)-1 (blue triangles), OA(0.3)-16 (red circles) and OA(0.8)-2 (green squares) AAO membranes synthesized in different oxalic acid solution concentrations measured by **a)** tangential SC on top and **b)** bottom surfaces, **c)** by transverse SP and by **d)** electrophoretic mobility (EM) of the ground AAO membranes.

For EM, since the transition is sharp, the uncertainties in the IEP determination are lower and an IEP increase of 1 pH unit (from 5.1 to 6.1) is observed by decreasing the OA from 0.8 M to 0.3 M but remains unchanged by decreasing further the OA concentration down to 0.05 M. Since the C/Al content decreases less between 0.8 M and 0.3 M than between 0.3 M and 0.05 M, the IEP modification

is not proportional to the oxalate content. The specific case of EM data will be discussed in a dedicated section below.

**Table 2-1** IEP of the studied membranes obtained from the  $\zeta$ -potential measurements by tangential flow streaming current on top and bottom surfaces, transverse flow streaming potential inside the nanochannels and electrophoretic mobility (EM) of the ground membrane samples with porcelain mortar and pillar.

Samples	IEP			
	Top	Bottom	Transverse	EM
<b>OA(0.8)-2</b>	6.7	6.9	9.8	5.1
<b>OA(0.3)-16</b>	7.1	6.1	9.4	6.1
<b>OA(0.05)-1</b>	6.4	6.2	9.2	6.1
<b>SA(0.3)-10</b>	-	6.7	9	5.1
<b>SA(0.3)-9</b>	7.3	-	-	-
<b>SeA(0.3)-2</b>	7.3	-	9	6

Let us focus on the effect of the contaminants nature, which can be modified during the synthesis in order to incorporate either sulfates or selenates. Figure 2-12 shows the evolution the  $\zeta$ -potential as a function of pH for OA(0.3), SA(0.3) and SeA(0.3) AAO membranes for the top outer (Fig. 2-12a), bottom outer surfaces (Fig. 2-12b), the pore wall surface (Fig. 2-12c) and the ground surface (Fig. 2-12d) and the IEPs values are shown in Table 2-1. Here again, no drastic changes are measured for the outer, inner and bulk surfaces when the nature of contaminants is changed. For instance, OA(0.3) and SeA(0.3) AAO membranes have similar  $D_p$  but difference in contamination nature and level but no variations in IEPs are observed. Thus the amount and nature of contaminants don't induce drastic IEPs changes, indicating that the surface groups properties are not affected by the AAO bulk composition.

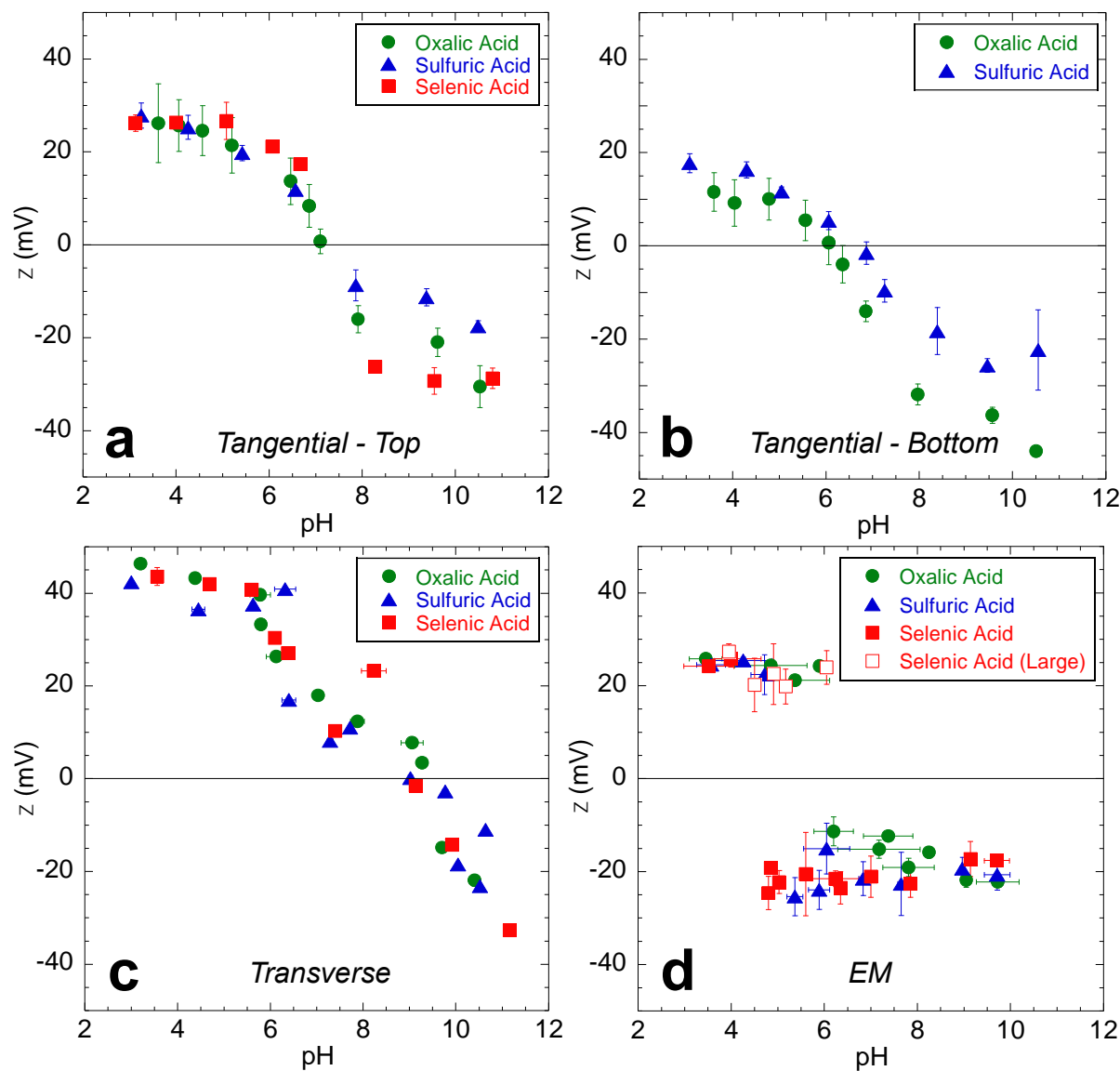


**Figure 2-12**  $\zeta$ -potential of the OA(0.3)-16, SA(0.3)-10<sup>1</sup> and SeA(0.3)-2 membranes synthesized in the oxalic, sulfuric and selenic acid solutions with 0.3M concentration measured by **a)** tangential flow streaming current on the top and **b)** bottom surface, **c)** transverse streaming potential inside the nanochannels and **d)** electrophoretic mobility (EM) of the powdered membrane sample.

<sup>1</sup> The membrane using for the Tangential – Top is the SA(0.3)-9.

## 2.7 Effect of buffers on the electrical surface properties of AAO membranes.

We had done a complete series of transverse streaming potential measurements through OA(0.3), SA(0.3) and SeA(0.3) membranes. The pH of the electrolyte solutions was adjusted by  $\text{NH}_4^+/\text{NH}_3$  buffer in pH values higher than 6.5 up to around 11, and  $\text{CH}_3\text{COO}^-/\text{CH}_3\text{COOH}$  buffer in pH values lower than 6.5. The initial measurement was done by water/KCl solution. Afterwards, the pH was reduced stepwise until around 3.5, followed by a measurement with KCl/water solution. The cycle was completed by increasing the pH stepwise by the solutions containing  $\text{NH}_4^+/\text{NH}_3$  buffer from pH 6.5 to more than 10. Figures 2-13a and 2-13b show the evolution of the  $\zeta$ -potential with pH for the membranes synthesized in different acids with 0.3 M solution (Fig. 2-13a) and membranes synthesized in different concentrations of oxalic acid (Fig 2-13b). In these figures, the data obtained in KCl/water solution,  $\text{NH}_4^+/\text{NH}_3$  containing solutions and in  $\text{CH}_3\text{COO}^-/\text{CH}_3\text{COOH}$  containing solutions are plotted by green, blue and red points respectively. The order in which the measurements have been done are shown on the figures starting from 1 ending to 5.

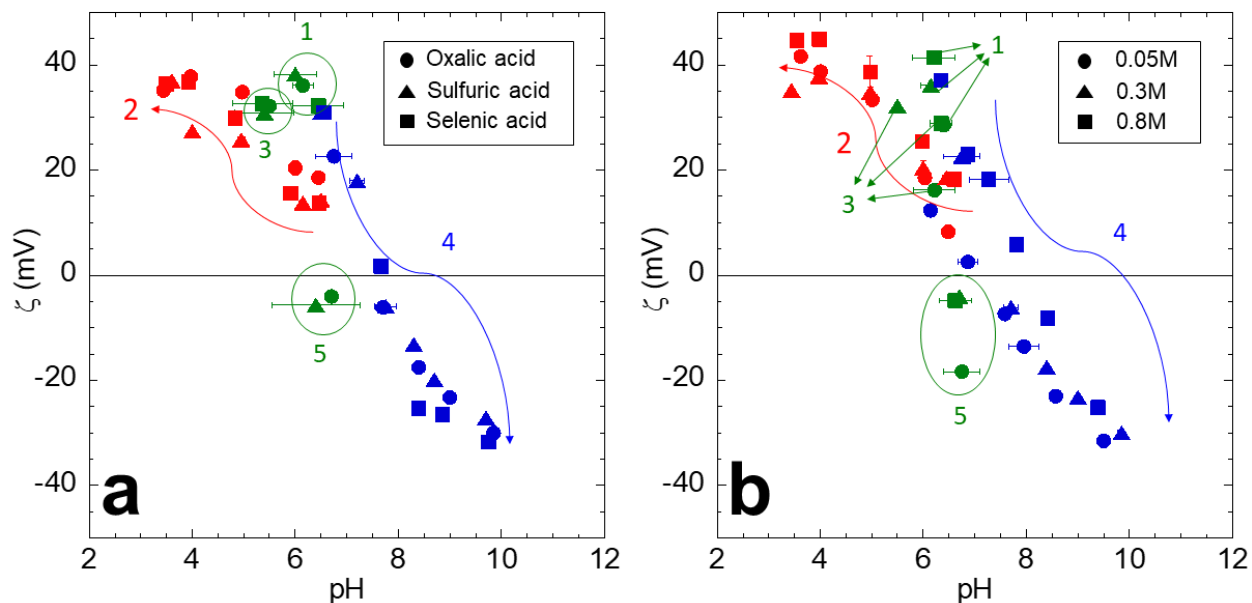


**Figure 2-13**  $\zeta$ -potential versus pH obtained by transverse streaming potential measurement through the nanochannels of **a)** AAO membranes<sup>1</sup> synthesized in oxalic acid (circles), sulfuric acid (triangles) and selenic acid (squares) and **b)** AAO membranes<sup>2</sup> synthesized in oxalic acid with the concentrations of 0.05 M (circles), 0.3 M (triangles) and 0.8 M (squares). The measurements are done in KCl/water solutions without buffer (green) and containing  $\text{NH}_4^+/\text{NH}_3$  buffer (blue) and  $\text{CH}_3\text{COO}^-/\text{CH}_3\text{COOH}$  buffer (red).

By analyzing these figures, some tips are observed. The first is that the isoelectric point is shifted around 1 pH unit for the AAO membranes by using buffers for adjusting the pH. The second is that in the pH values overlapping between different solutions, we see different values for the  $\zeta$ -potential. These can be due to the changes that the surface of the AAO nanochannel undergoes by contact with the buffer species. As an example, chemical interactions between the hydroxyl groups of the alumina surface with the carboxylic groups have been reported by Seravanan et al [94]. And there are carboxylic groups ( $\text{COO}^-$ ) in acetic acid and acetate salts species in the buffer. This can be the reason according to which we see a decrease in the  $\zeta$ -potential values between step 1 measurements and the first measurements of step 2 although the pH values are the same. They have reported irreversibility for the adsorption of carboxylic groups on alumina surface which implies that the interaction is not hydrogen bond or electrostatic. As mentioned above, the pH- $\zeta$  cycle was terminated by measurements in water/KCl solutions without buffer (Step 5). Although the pH values are less than 7, we can see that the nanochannels surface is still negative. It can be either due to lack of enough time for the

<sup>1</sup> OA(0.3)-12, SA(0.3)-12, SeA(0.3)-2

<sup>2</sup> OA(0.05)-1, OA(0.3)-12, OA(0.8)-1

nanochannels surface to become positive, or due to the chemical adsorption of  $NH_4^+$  ions on the alumina surface. Adsorption of the  $NH_4^+$  on alumina surface in pH less than the IEP has been reported [95]. It can be concluded that there are non-electrostatic interactions between  $NH_4^+$  and the alumina surface same as what reported for carboxylic groups. Accordingly, there are possibilities of the occupation of the charged hydroxyl sites because of chemical interactions with the buffer ions. Hence, it was decided not to use buffers in our work for maintaining the pH.

## 2.8 Influence of nanochannel curvature.

In addition to the amount and to the nature of contaminants that showed not to affect significantly the IEP, the question of the curvature effect can be raised and explored by changing the diameter  $D_p$  of the pores. Indeed, Pedimonte et al measured in tangential mode an increase of IEP with  $D_p$  ( $\approx 1.2$  pH unit from a  $D_p$  of 15 nm to 40 nm) on non-detached thin porous alumina films. This shift is proposed to result from the existence of two areas with different Al coordination, the relative proportion of which varies with the size of the pores, assuming a composition independent on the pore sizes [85]. On the contrary, Baca et al. observed no significant variation of the IEP for pores ranging from 2 to 20 nm, however on commercial mesoporous alumina and using classical titrations, as large amounts are available [96]. This effect of curvature can be analysed from our data on the IEPs determined by tangential and transverse SE since, for EM, AAO is ground and the probed surfaces are presumably different (see section below). Fig. 2-14 displays the IEPs as a function of nanochannel  $D_p$  and there is no significant IEP variation with  $D_p$ , indicating that, within our investigated range of  $D_p$  (from 31 nm to 61 nm), no curvature effect is observed whatever the SE mode used (tangential or transverse), confirming the results of Baca et al [96] with alumina with different pore sizes and similar composition. Note that, as in our case, the ionic strength is such that the diffuse layers are not large enough to overlap so that an effect due to overlap cannot be excluded for lower ionic strengths. Concerning our tangential measurements, they do not show the same trend as Pedimonte et al [85], however the pore diameters  $D_p$  are larger in the present study and their variations of IEPs are not so large. Their interpretation is nevertheless connected to the existence of different regions in the material, here probed by the different electrokinetic techniques, enlightening large differences that will be discussed later.

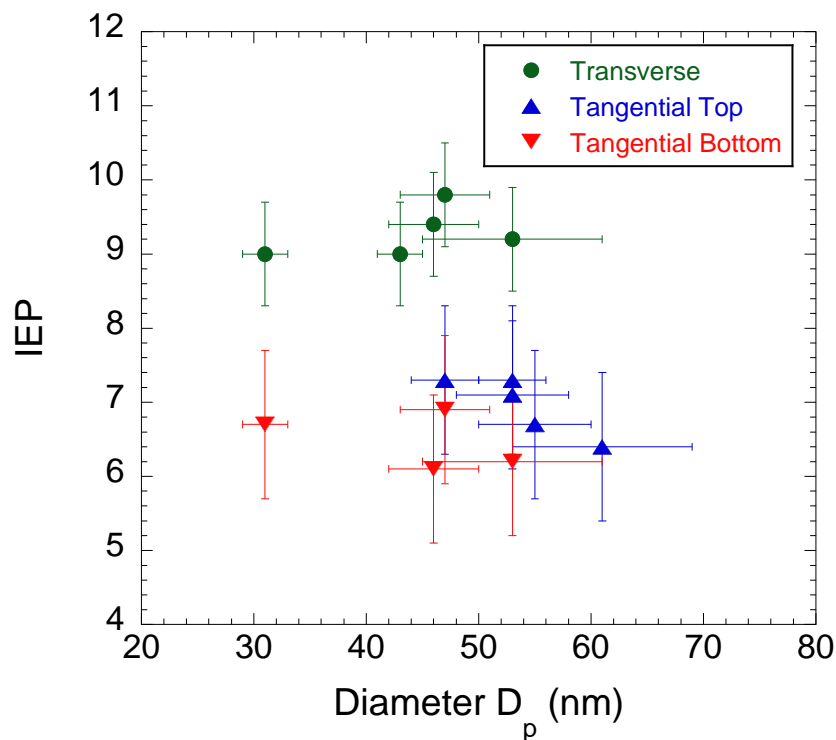


**Figure 2-14** IEP as a function of nanochannel diameters  $D_p$  obtained by transverse (green circles) and tangential SE (top: blue triangles; bottom: red inverted triangles). The error bars of the IEPs were estimated from two measurements performed on OA-0.3 AAOs.

## 2.9 The case of EM

Let us focus on the EM experiments for which different results have been obtained. Contrary to the SE, the AAO is ground for EM to prepare a particle suspension. Fig. 2-15a shows the SEM images of the AAO powder after grinding it in a porcelain mortar. Objects with multiple sizes below  $100 \mu\text{m}$  are observed. At higher magnification (Fig. 2-15b) the porous structure is still visible and the nanochannels are preserved. Once the AAO powder is dispersed in aqueous solution, the volume size distribution can be obtained by laser granulometry for the different AAO suspensions studied by EM. Several populations in size are measured for each sample, the highest proportion being centered on  $20 \mu\text{m}$ , value of the order of the membrane thickness (see Fig. 2-15c), indicating a good reproducibility of the grinding process with the mortar. Additionally, DLS performed on suspensions without stirring revealed that, after sedimentation of the biggest objects (typically after 60 mins), the typical size is around 1 to few microns.

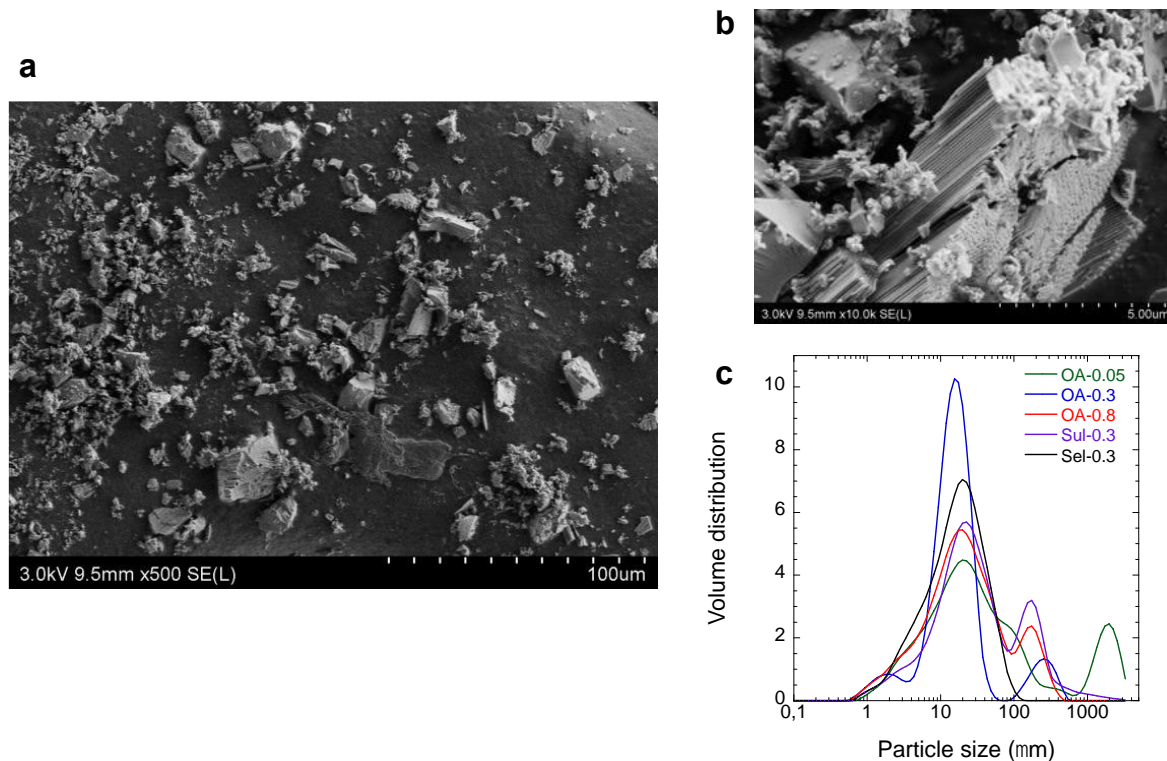


**Figure 2-15 (a)** and **(b)** SEM images of OA(0.8)-2 AAO membrane manually ground in a porcelain mortar. **(c)** Volume size distribution as a function of particle diameter obtained by laser granulometry for the different AAO suspensions studied by EM. The volume size distribution is an average of 5 measurements. OA-0.05 also presents larger objects ( $> 1000 \mu\text{m}$ ) that can be dust since all these solutions are not filtered prior to measurement.

Note that EDX measurements performed on the sample area shown in Fig. 2-15a reveal the presence of silicon Si, certainly coming from the porcelain mortar and pillar. To rule out the possible influence of Si on the measured IEPs, we also ground OA-0.8 AAO with an agate mortar (for which no Si has been detected by EDX after grinding) and performed EM and laser granulometry (see Fig. 1 Appendix). The volume size distribution in Agate is similar in terms of population sizes but with a higher proportion of large objects of about  $250 \mu\text{m}$  (Fig. 1b-Appendix). However, the evolution of the  $\zeta$ -potential with pH is similar with the same IEP as the AAO sample ground with porcelain mortar and pillar (Fig. 1c Appendix). The IEP is thus not affected by the presence of Si.

The IEPs obtained by EM are comprised between 4.4 and 6.1 (listed in Table 2-1), consistent with recent experiments done on similar AAO crushed membranes [89], and are close to the tangential ones. The main question arising here is about the nature of the probed surfaces during EM. In the membrane, the surface area of the pore walls is around 200 times larger than the outer surfaces (top

and bottom). However, the grinding process creates new surfaces, exposing the bulk AAO, i.e. the material located inside the walls that are between the channels. The area of this new surface is at least of the order of the area of the pore walls and can thus modify the IEP of the ground membranes. The data from Table 2-1 indicate that the IEP of the new surfaces, which correspond to the material inside the wall, is lower than the IEP of the pore walls. It could be due to the quantity of contaminants incorporated in the material, evidenced with EDX and ATR-FTIR (Fig. 2 Appendix). Neither the amount of contamination nor its nature (C, S or Se) have a huge impact on the IEPs, which vary by half a pH unit. Finally, the obvious first conclusion from these measurements is that EM measurements of ground AAO do not provide an IEP that corresponds to the one of real surfaces of the AAOs used in multiple applications in the form of membranes (i.e., pore wall or outer surfaces).

## 2.10 How can we reconcile the tangential and transverse results?

Finally, this last section is dedicated to the discussion about the clear difference between the IEPs determined by tangential ( $\approx 7$ ) and transverse SE ( $\approx 9$ ). From the previous sections, we concluded that both SE modes, taken separately, are not influenced by composition or curvature. However, a clear shift is observed between these two SE modes, suggesting differences between the probed surfaces.

We first remind that the differences are not due to possible external contaminations or AAO chemical transformation in water. For the former, the pH was directly adjusted to a high value (pH around 10) to ensure that, for both SE modes, the AAO surfaces were not contaminated by impurities and then decreased stepwise down to about 3. Moreover, the surfaces obtained after grinding, which cannot be polluted as the others could be, give even lower IEP values, strengthening the existence of a difference depending on the probed surface. For the latter, it has been shown that the chemical transformation is a slow rated process that can decrease the density of active sites at the surface [97]. Here the experiments duration is typically ranging from 2 h to 9 h to perform a complete  $\zeta$ -potential versus pH curve, i.e., are shorter than the time needed to initiate the alumina chemical transformation (typically  $> 1$  day), indicating that our surfaces remain stable in term of density of active OH sites within our experimental time window.

Let's now discuss the possible origins in IEP differences. The probed surfaces are presumably different between the tangential and transverse mode in term of i) surface morphology and/or ii) chemical environment (including coordination, density of active sites, or atomic composition). In

tangential mode the probed surface consists in an alternance of two types of regions: holes (corresponding to the opening of the nanochannels) and alumina that is also heterogeneous in composition (see Figure 2-16a and 2-16b). In transverse mode the probed surface is only made of alumina homogenous in composition (see Figure 2-16c).

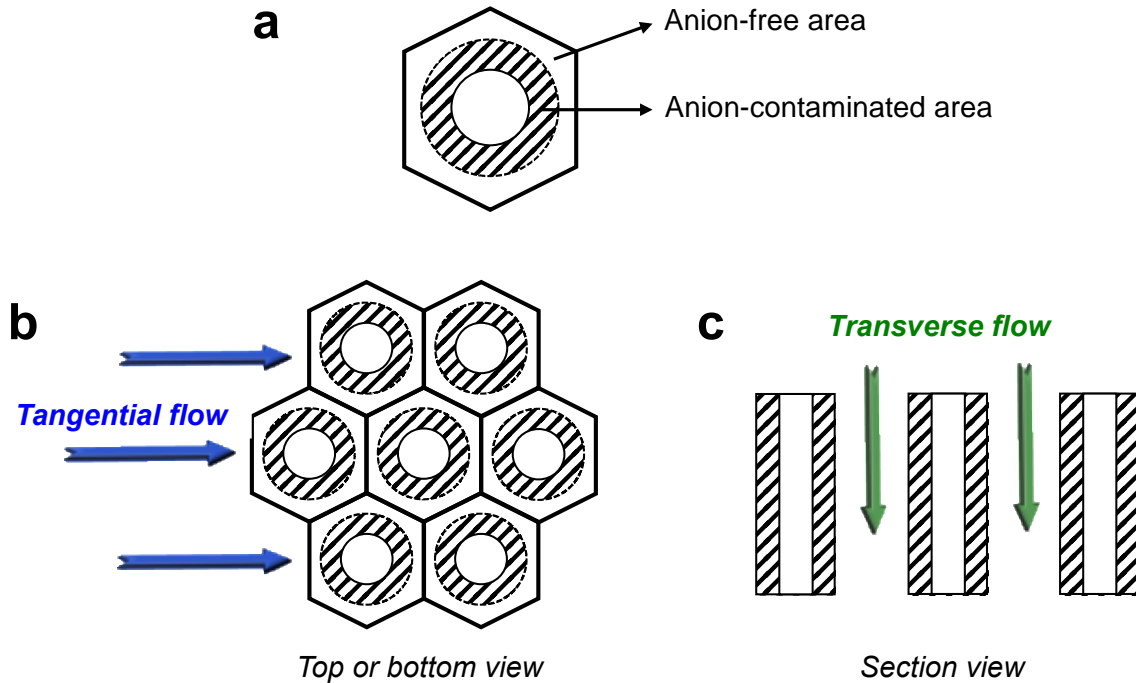


**Figure 2-16** (a) Schematic representation of AAO hexagonal cell made of two areas: one anion contaminated (hatched region) and one anion-free. (b) Top or bottom schematic representation of the outer surface exposed to the tangential flow. (c) Section view with the exposed AAO surface to the transverse flow.

Let's first discuss the possible influence of the morphology on the IEP and in particular the influence of surface roughness. Here, the RMS roughnesses ( $R_q$ ) of the outer surfaces of OA membranes have been determined by AFM measurements. AFM images are shown in Figure 2-17 and the results are presented in Table 2-2.  $R_q$  ranges from 7 nm to 17.5 nm and increase when  $D_p$  increases (OA(0.05)-1 > OA(0.3)-16 = OA(0.8)-2). No differences are observed between the top and the bottom surfaces.

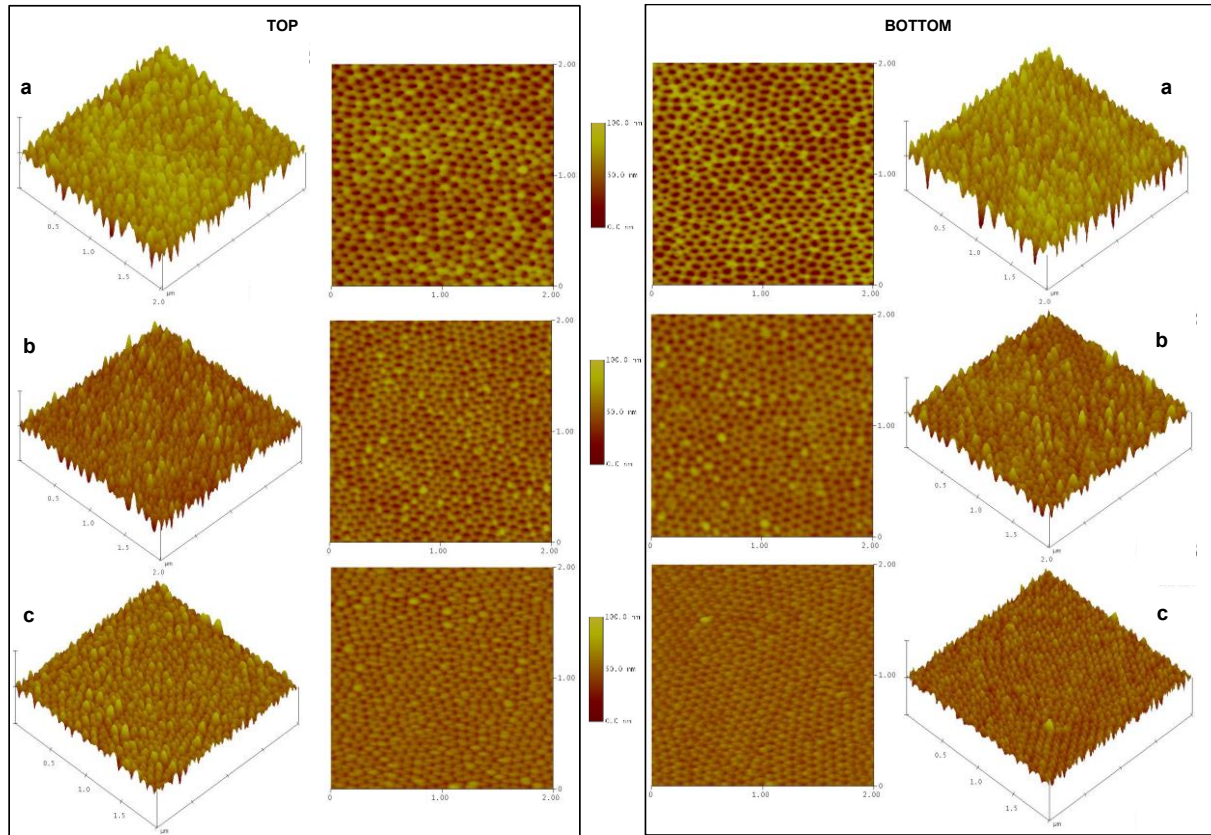


**Figure 2-17** AFM images of top (left side) and bottom (right side) surfaces of AAO membranes: OA(0.05)-1 (**a**), OA(0.3)-16 (**b**), OA(0.8)-2 (**c**).

**Table 2-2** RMS roughness  $R_q$  determined by AFM measurements. The corresponding images are shown in Figure 2-17

AAO membrane	$R_q$ (nm)	
	TOP	BOTTOM
OA(0.05)-1	$15.7 \pm 3.2$	$17.5 \pm 2.2$
OA(0.3)-16	$10.6 \pm 0.5$	$9.9 \pm 1.5$
OA(0.8)-2	$7.0 \pm 1.1$	$6.9 \pm 1.7$

On the contrary, the roughness of the inner surface is more challenging to probe. By using SAXS, Engel et al. found a roughness of 0.5 nm [98], significantly smaller than the outer surfaces. Thus, both probed surfaces have clear roughness difference.

The influence of roughness on IEP has been studied by Borghi et al. [93] on non-porous TiO<sub>2</sub> films of various roughnesses (4 to 26 nm) using AFM force measurements with a colloidal probe in 1 mM NaCl solution, giving a Debye length of 9.6 nm i.e, in the middle of the roughness range. The IEP decreases by 3 pH units between the flattest and the roughest surfaces and the authors propose that this shift originates from the diffuse layer overlap. In our case, the Debye length is much smaller (1 nm) compared with the estimated roughness but we cannot fully exclude that some roughness on the same scale modifies the IEP compared with the one of the very smooth pore surface. Additionally, in these conditions where the Debye length is smaller than the roughness dimension, a decrease of the  $\zeta$ -potential due to the shear flow attenuation by the protrusions is expected [80] and it can explain the decrease in absolute  $\zeta$ -potential compared to the inner surface we observed (Fig. 2-10).

We will explore now the possibility of IEP shift due to the modification of local chemical environment: coordination, density of active site, atomic composition or preferential adsorption. It has been intensively demonstrated that AAO are heterogeneous in composition (Figure 2-16a) with an anion contaminated and anion-free area; the extent of the anion-contaminated region being dependent on the nature and the size of the contaminants: the smaller the contaminant the more extended the contaminated area [35]. Discriminating between the two regions is rather difficult as direct measurements like XPS can only probe the surface atomic composition of the whole outer surfaces and the inner pore wall surface is not directly available. However, due to this heterogeneity, as shown in Fig. 2-16, the tangential SE probes a heterogeneous surface while the transverse mode only probes a homogeneous anion-contaminated area.

One can then propose that the IEP shift is a consequence of the differences in the chemical environment of the surface hydroxyl groups. The protonation / deprotonation process of the OH groups is sensitive to the heterogeneities at the surface and the dissociative constants (i.e. pKa's) can differ from each other because of the number of surrounding Al<sup>3+</sup> (i.e. singly, doubly or triply coordinated OH groups) and/or by the Al<sup>3+</sup> coordination number (CN) [99]. The average CN was estimated by <sup>27</sup>Al NMR around 4.75 with a predominance of 5-fold coordinated Al for AAOs synthesized in OA, sulfuric or phosphoric acid [100]. Additionally, Ijima et al. also proposed by using <sup>27</sup>Al NMR that the anion-contaminated area is mainly composed of 6-fold coordinated Al<sup>3+</sup>, while the

anion-free area is composed of 4-fold and 5-fold coordinated  $\text{Al}^{3+}$  [101]. It was reported that single OH within a 6-fold coordinated  $\text{Al}^{3+}$  has a pKa of 9.5 while it was 4.4 for single OH within 4-fold coordinated  $\text{Al}^{3+}$  [99]. These observations allow us to propose an interpretation to reconcile the observed IEP differences between the outer and inner surfaces. The inner surface (which corresponds to the anion-contaminated area) might be composed of single OH within a 6-fold coordinated  $\text{Al}^{3+}$  with a pKa of 9.5, consistent with our IEP of around 9. On the other hand, the outer surfaces (which are made of both anion-contaminated and anion-free regions) might be composed of both OH types (pKa of 9.5 and 4.4) and can give an average IEP of 6 – 7 depending on the relative proportions of both types.

A similar argument has been used by Pedimonte et al. to explain the IEP shift observed for the top outer surface with tangential SE [85]. Their interpretation is however different: they consider singly coordinated Al-OH (with 2 pKa giving a predicted IEP of 8.5) on the flat area (corresponding to the anion-free region) and doubly coordinated Al<sub>2</sub>-OH, also with 2 pKa giving a predicted IEP of 5.4, on the curved area around the channel aperture (corresponding to the anion-contaminated region). Changing the pore diameter modifies the proportion of these two areas and therefore the IEP. Although the depth of contamination depends on the synthesis conditions, this contamination should be higher in the curved area at the top of the pores than in the flat area between the pores, which means that their conclusion is opposite to our results. However, the direct study of the inner pore wall surface and of the ground material and the decoupling of the different parameters that can change in these nanoporous materials strengthen the result of a higher IEP on the anion-contaminated areas.

## 2.11 Conclusions

In this chapter, the electrical surface properties of AAO membranes have been studied by combining several electrokinetic techniques in order to determine the surface  $\zeta$ -potential and IEPs. By using tangential and transverse streaming potential/current as well as electrophoretic mobility (EM) experiments, the outer (top and bottom planes), the pore wall surfaces and the the surfaces created after grinding can be probed. Interestingly, a clear IEP difference by around 2 pH unit is measured between outer and pore wall surfaces, which means that the outer and pore wall surfaces can be of opposite sign on a range of pH. This difference can be attributed to a modification of local chemical environment of surface hydroxyl groups, i.e., number of surrounding  $\text{Al}^{3+}$  and/or the  $\text{Al}^{3+}$

coordination number. Additionally, the IEPs obtained by EM on ground membranes are slightly lower than the ones of the outer surfaces. We hypothesize that the grinding process creates new surfaces, exposing the materials of the AAO walls, whose composition is dependent on the nature and amounts of contaminants. This work shows that the electrical properties of a single nanoporous material can differ depending on the nature of the probed surface. Our experimental approach can further help to clarify the electric surface behavior of various systems since it can be used for different types of nanoporous membranes (organic or inorganic). Now, the electric surface properties of our AAO membranes are clear for us from the IEP points of the different surfaces. We will use this information in the upcoming chapter where we study the adsorption of the polyelectrolytes on the inner surface of the AAO membranes nanochannels. Once in the AAO membranes a magnificent change in the magnitude or the sign of the  $\zeta$ -potential is observed, it is required to know the electric surface properties of the AAO membrane in order to be able to discuss the reason of the change of the  $\zeta$ -potential. Either it is due to the adsorption of a species possessing a charge opposite to the surface, or it is due to approaching the IEP because of the pH of the environment. Besides, it is highly useful for us to know in which pH range the surface of our AAO is positively charged and beyond which pH it is negative. This can reach us to conclusion about the nature of the interactions of the different species on the AAO nanochannels surface i.e. if a chemical species is adsorbed on the surface with the same charge, the interaction is not electrostatic.

## **3 Chapter 3: The Behavior of Polyelectrolyte Chains Under Confinement in the Nanochannels of AAO membranes**

### **3.1 Introduction**

In this chapter, we present our studies on the behavior of the sodium polystyrene sulfonate (NaPSS) as a model negatively charged strong polyelectrolyte inside AAO charged nanochannels. For studying the penetration of PSS inside AAO nanochannels, we monitor the change of the surface charge of the nanochannels over time by determining the  $\zeta$ -potential through transverse streaming potential measurements. We go through evaluation of the variables affecting the behavior of the NaPSS inside AAO nanochannels.

### **3.2 State of the art of the polyelectrolyte macromolecules inside nanoporous media**

The adsorption of the polyelectrolytes (PEs) on metal oxide surfaces has various important applications such as, for instance, water treatment [102], [103], electronics [104], drug delivery [105] and catalysis [76]. For this reason, in the last decades this subject has attracted the attention of many researchers from different viewpoints. Many works have been done in order to study the PE adsorption on metal oxide surfaces with different geometries such as plates [106]–[113], beads [114], particles [115]–[117] and inside nanoporous media on the walls of the confining medium [104], [118]–[126].

Considering the PE adsorption on the metal oxide surfaces as a physical process, many works have been done on studying the kinetics of this process since 1980s and 1990s. Muthukumar has presented one of the earliest works on the PE adsorption on charged surfaces and considered temperature, Debye length, surface and polymer charge density to be the main parameters affecting this process [127]. Experimental studies on the PE adsorption on the metal oxide have been pioneered by adsorption on the flat surfaces. The majority of these studies have considered the effect of ionic strength on the adsorption amount of the polyelectrolytes on the surface using techniques such as ellipsometry, reflectometry, surface force measurements and UV-vis absorption spectroscopy [106],

[108], [113], [128]–[130]. It is observed that increasing the ionic strength increases the adsorption amount up to a specific concentration because of screening the repulsion forces between the polyelectrolyte chains. But after a level of salt concentration, it screens the electrostatic attractions between the polyelectrolytes and the surface. So, the subject is the balance between the long range and short range interactions screening [106], [131].

Electrokinetic techniques such as streaming current and streaming potential also have been used for studying the adsorption of polyelectrolytes on the metal oxide surfaces [110], [111], [132], [133].

Numerous research works have been done on the hydrodynamic and electrokinetic properties of the polyelectrolytes – solid interfaces [109]–[111], [132]–[134]. These authors have proposed models and correlations for the surface conductivity and swelling properties of the polyelectrolyte films in order to interpret their electrokinetic variables on their studied surfaces accurately. One of the main points that has been considered for increasing the accuracy of determining the electrokinetic variables on the interface of polyelectrolyte layers is distinguishing the layer from a hard surface. In brief words, the behavior of the polyelectrolyte adsorbed layer which is classified in soft surface is different from a rigid surface such as bare metal oxide [135]–[138]. According to the work of the researchers, the electrokinetic behavior of the soft nanochannels is different from that of the rigid nanochannel. For example, it is reported that the electroviscous effect in soft nanochannels shows a monotonic decrease with the EDL thickness while in the rigid nanochannels the electroviscous effect first increases and then decreases with EDL thickness [137]. One approach to more accurate calculation is to distinguish between the polyelectrolyte layer (considered as the diffuse soft layer) and the rigid surface and solving the electrokinetic equations based on linearized or nonlinearized Poisson-Boltzmann equation. Duval has shown that in high concentrations of polyelectrolyte and consequently low Donnan potentials, the linear and nonlinear Poisson-Boltzmann equations lead to similar results [136]. The Donnan potential exists in the polyelectrolyte layer adsorbed once the thickness of the layer is higher than the debye length [139]. If we consider high concentration of polyelectrolyte equivalent to a more compactly adsorbed polyelectrolyte layer, it can be concluded that the swallowing the polyelectrolyte layer will lead to more deviation from the predictions of simple models of the electrokinetic variables.

In a series of experimental works, Adamczyk and coworkers studied by electrokinetic measurements (streaming current or streaming potential experiments) the adsorption behavior of different charged species (colloids or PE) and they proposed a relation between PE coverage and zeta potential assuming that the surface coverage can be governed either by diffusion or mass-transfer due

to convection. They have also proposed an equation for measuring the coverage for their case studying the adsorption of poly(allylamine hydrochloride) (PAH) on mica surface [109]:

$$\zeta(\theta) = F_i(\theta)\zeta_i + F_p(\theta)\zeta_p \quad (3-1)$$

Where where  $\zeta(\theta)$  is the zeta potential of the polyelectrolyte-covered substrate,  $\zeta_i$  is the zeta potential of bare mica,  $\zeta_p$  is the zeta potential of PAH molecules in the bulk, and  $F_i(\theta)$ ,  $F_p(\theta)$  are the dimensionless functions of the coverage and the electrical double-layer thickness.

After considering the polyelectrolytes adsorption of flat surfaces, attentions were attracted to the adsorption on the curved surfaces. Muthukumar also stated theoretically that the PE adsorbed amount on curved charged surfaces is different from the planar surfaces [140]. According to the geometry of the surface, the adsorbed amount on the surface varies based on the energy and entropy concepts. It is theoretically shown that the critical adsorption parameter which implies the critical amount adsorbed, increases from spherical to planar surfaces [141]. Nanopores and nanochannels are examples of the surfaces that possess highly curved surfaces on which the adsorption of polyelectrolytes is studied both in closed pores [120], [123]–[126], [142]–[144] and through-hole medium [88], [118], [121], [122], [145]. Majority of the works done on the adsorption of polyelectrolytes inside nanoporous media have focused on layer by layer deposition of the polyelectrolytes. Researchers have studied parameters affecting the adsorption kinetics and the thickness of the adsorbed polyelectrolyte layer in nanoporous media [121], [125], [143], [145]. Examples of the techniques that have been used for accessing the polyelectrolyte layers adsorbed inside the nanopores and nanochannels consists of streaming potential measurement [88], streaming current measurement [146], electroosmotic flow [145], reflectometric interference spectroscopy [126], [143], optical waveguide (OWS) spectroscopy [123]. The most important variables are seen to be the polyelectrolyte size, nanopore or nanochannel size and the ionic strength of the solution. Based on their studies, the thickness of the adsorbed polymer layer increases in the nanopore or nanochannel with increasing the ionic strength [145] and the pore diameter [124], [125].

Here we study the diffusion/adsorption behavior of sodium polystyrene sulfonate (NaPSS) inside our homemade synthesized AAOs using transverse streaming potential measurement. A sketch of the monomer of this polymer is shown in Figure 3-1. Figure 3-1a shows the structural formula of

NaPSS and in Figure 3-1b we have shown the 3D sketch of the monomer. Both the structural formula and the 3D sketch have been drawn by MolView.

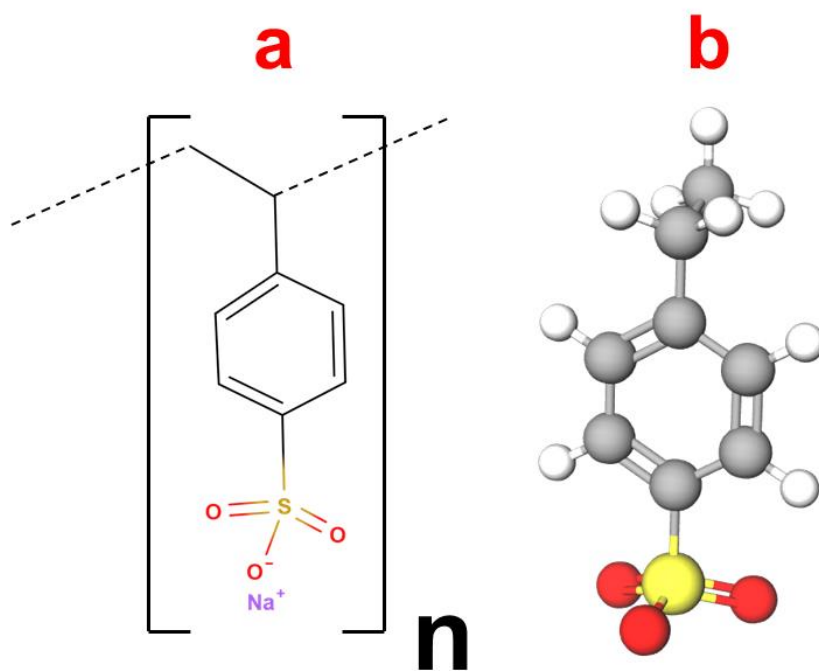


**Figure 3-1 a)** Structural formula of sodium polystyrene sulfonate and **b)** 3D sketch of the monomer.

In order to conduct our study, there are some characteristics that are worthy to be known from this macromolecule. The radius of gyration ( $R_g$ ) can be defined as the average distance of the atoms from the center of mass of the polymer chain. The hydrodynamic radius is the radius that the polymer chain possesses when displacing in aqueous solution which consists also of the double layer forming around the monomers and the water molecules hydrating the atoms and charged groups in the polyelectrolytes. The length of the polymer chain in the fully stretched state is called the contour length. Since the styrene sulfonate monomer has a length of  $2.5 \text{ \AA}$  [147], the contour length of the sodium polystyrene sulfonate with molecular weight ( $M_w$ ) of  $7 \times 10^4 \text{ g/mol}$  is approximately 85 nm. The hydrodynamic diameter of the PE macromolecules depends on the ionic strength of the solution. For 50 mM KCl it is reported to be 20 nm [88]. The persistence length is the length in which the polymer chain has no flexibility to bend anymore and behaves like a stiff rod. In dilute regimes, this length decreases with the ionic strength and it is reported to be around 15 nm at  $I = 2.5 \text{ mM}$  for molecular weight of  $74 \times 10^3 \text{ g/mol}$  [148]. Thus, for the higher ionic strengths it is expected to be lower.

Another characteristic that is important to analyze for studying the transport of the PE macromolecule is the diffusion coefficient. For NaPSS of the  $M_w = 7.85 \times 10^4$  g/mol in dilute regime and ionic strength of 50 mM, the diffusion coefficient ( $D$ ) is reported to be  $3.1 \times 10^{-7}$  cm<sup>2</sup>/s [149]. In case we consider this value valid for the case of diffusion inside nanochannels, it means that for passing a distance of 50  $\mu$ m which is equivalent to our thickest membrane, the time of diffusion can be calculated by equation 3-2 [150]:

$$\bar{\Delta} = (2Dt)^{1/2} \quad (3-2)$$

$$50 \times 10^{-4} \text{ cm} = (2 \times 3.1 \times 10^{-7} \times t)^{1/2} \rightarrow t = 40 \text{ s}$$

So, in case of considering the situation in a nanochannel same as the bulk, 40 s time is needed for the macromolecule chain to pass through the 50  $\mu$ m long nanochannel.

Zamrik et al [143] studied the kinetics of polyelectrolyte deposition inside the nanochannels of the AAO. In their work, they reached to the conclusion that the deposition of the polyelectrolyte on the nanochannels surface is limited by diffusional mass transfer. In our work, we will consider this phenomenon in our experiments.

### 3.3 Methods to monitor the polyelectrolyte diffusion in AAO nanochannels

#### 3.3.1 In situ monitoring

In this work, it is sought to study in which rate the polyelectrolytes (PE) adsorb on the surface of the AAO nanochannels. For this, we have utilized the *in situ*  $\zeta$ -potential determination by transverse streaming potential measurement using the same instrument described in chapter 2. At the beginning, the compartments of the streaming potential instrument are filled with the electrolyte solution at a given pH and ionic strength without PE and the  $\zeta$ -potential of the bare AAO is determined at this step. Afterwards, the electrolyte is evacuated and the cell compartments are loaded with a PE solution at the same pH and ionic strength as the preceding step and the  $\zeta$ -potential of the AAO nanochannels in contact with this solution is determined *in situ*. Finally, a washing step in KCl solution is performed to wash away weakly or non-bonded PE chains from the nanochannels. In our experiments, we have used sodium polystyrene sulfonate (NaPSS) with the molecular weight  $M_w$  of 70 kDa and polydispersity of 1.8 [155] having a hydrodynamic diameter of about 19 nm (as determined by DLS measurement in

100 mM KCl solution at pH = 6). This PE macromolecule is a strong negatively charged PE, i.e., fully dissociated in the whole pH range. At a pH lower than the IEP, the AAO nanochannels are positively charged and the PE is expected to adsorb onto the surface and to gradually reverse the sign of the charged AAO surface. Such change in the electrical surface properties can be followed by the electrokinetic measurements such as streaming potential that we use. Figure 3-2 shows an example of *in situ* monitoring of PE adsorption in which a continuous decrease in the  $\zeta$ -potential is observed.

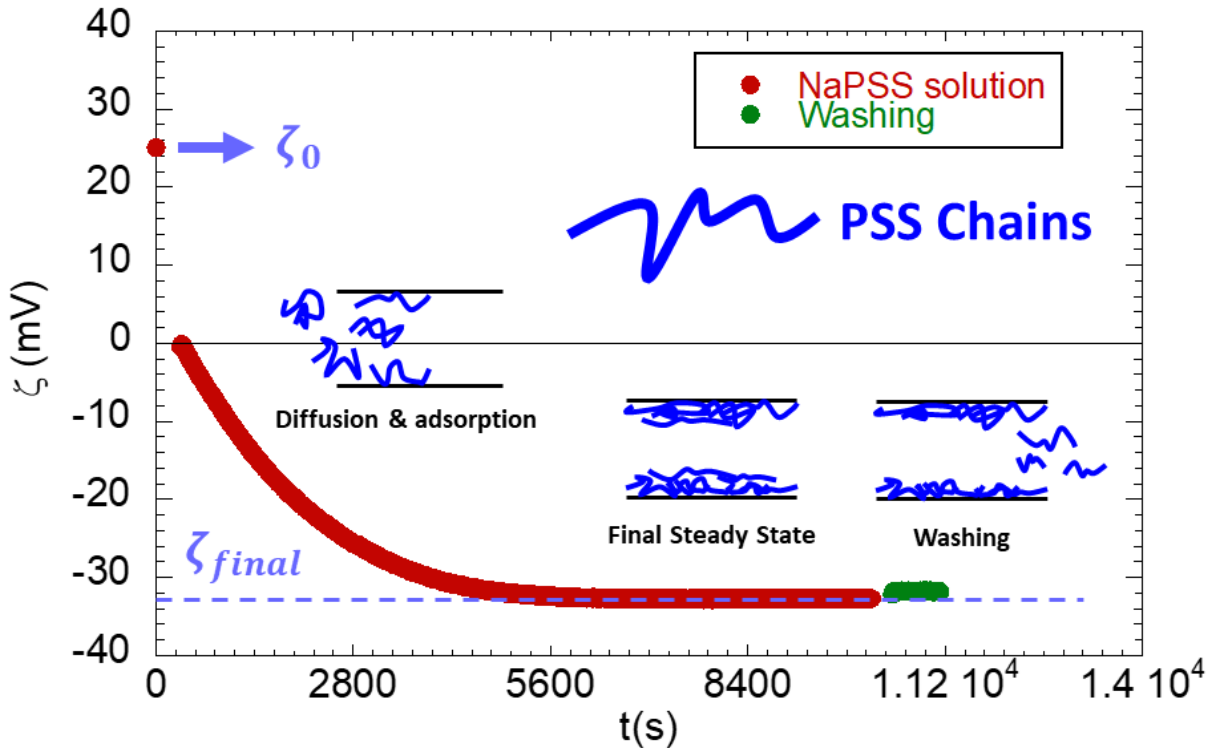


**Figure 3-2**  $\zeta$ -potential of the OA(0.3)-9 membrane nanochannels versus time after exposure to the polystyrene sulfonate aqueous solution with 0.5 g/L NaPSS concentration, 10 mM ionic strength and pH =6 at  $t=0$ .

By analyzing this curve, we can discuss the kinetics of the diffusion and adsorption of the NaPSS chains inside the AAO nanochannels and the parameters affecting the rate of the process, which are shown in Figure 3-2. In our work we succeeded to do *in-situ* experiments in AAOs with different pore diameters (20 to 50 nm), different pore lengths (10 to 50  $\mu\text{m}$ ), different ionic strength (1 to 100 mM) and PE concentration (0.5 and 1.5 g/L). The curve in Figure 3-2 can be fitted with an exponential equation as follows:

$$\zeta(t) = \Delta\zeta \exp\left(-\frac{t}{\tau}\right) + \zeta_{final} \quad (3-3)$$

$$\Delta\zeta = \zeta_0 - \zeta_{final}$$

The main parameter by which we can examine the rate of the process that we are studying is the characteristic time in the equation ( $\tau$ ). This value indicates the time at which the difference between the instant  $\zeta$ -potential and the steady final value ( $\zeta(t) - \zeta_{final}$ ) reaches to the 36.8% of the initial value which is the  $\Delta\zeta$  in equation 1. It can be interpreted that the surface has reached to 38.6% of the coverage that it reached in the final steady state. Since there are differences in the solutions conditions of different experiments such as ionic strength, we have also normalized the  $\zeta$ -potential values of the curves by reporting them as a ratio of the corresponding  $\zeta$ -potential value to the initial value:

$$\zeta_r(t) = \frac{\zeta(t)}{\zeta_0} \quad (3-4)$$

Thus, equation 3-3 and the data analysis will be conducted based on equation 3-4. The characteristic time ( $\tau$ ) will not change by switching  $\zeta(t)$  to  $\zeta_r(t)$ .

$$\zeta_r(t) = \Delta\zeta_r \exp\left(-\frac{t}{\tau}\right) + \zeta_{r,final} \quad (3-5)$$

$$\Delta\zeta_r = \frac{\zeta_0 - \zeta_{final}}{\zeta_0} = 1 - \frac{\zeta_{final}}{\zeta_0} = 1 - \zeta_{r,final}$$

By obtaining the curves of the  $\zeta$ -potential ratios versus time, we obtain the characteristic time by curve fitting. The characteristic time gives us insight of the rate of the process.

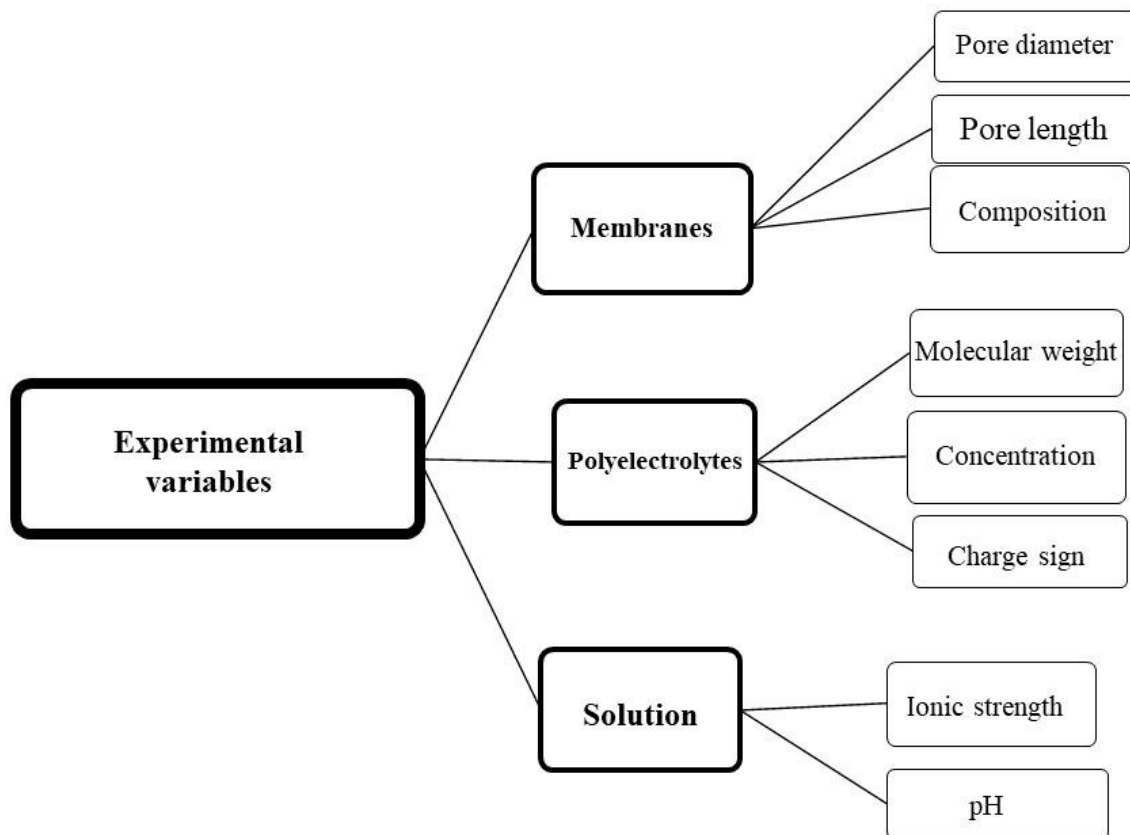


**Figure 3-3** Parameters that might affect the kinetics of adsorption of the PSS chains on the surface of AAO membranes nanochannels.

In-situ experiments were used also for studying the nature of the interaction between the PSS polyelectrolyte chains and the charged surface of the AAO nanochannels. Moreover it is important to know the reversibility of the adsorption of PSS macromolecules on the AAO nanochannels surface. From the reversibility, the type of the interactions between the AAO nanochannels and the PSS macromolecules can be discussed. For this reason, we made sequences of *in situ* measurements with two approaches. In the approach 1 we study the possible adsorption of NaPSS on a negatively charged AAO. It will give us information on the nature of the interaction between the PSS macromolecules and the AAO nanochannels surface. In case the PSS is not adsorbed in basic pH (higher than the IEP point where the surface has a negative net charge), it can be concluded that the interaction between the PSS macromolecules and the AAO nanochannels surface is purely electrostatic. In the approach 2, the NaPSS is first adsorbed on a positive AAO and then the pH condition is changed in order to change the sign of the AAO surface (from positive to negative). Beside the nature of the interactions,

with this approach we can also study the reversibility of the adsorption in case we can remove the PSS from the surface of the AAO by switching the surface charge by changing the pH to a value higher than IEP.

**Description of approach 1:**

- 1) SP measurement in KCl solution at pH ~ 4,
- 2) SP measurement in KCl solution with pH ~ 9,
- 3) repeating step 1,
- 4) repeating step 2,
- 5) SP measurement in a NaPSS solution with the same ionic strength as the preceding steps at pH~9 (pH > I.E.P of AAO, the AAO is thus negatively charged).
- 6) SP measurement in a solution with the same ionic strength and pH as step 5 but without PE molecules,
- 7) SP measurement in a solution with the same ionic strength as step 6 but with pH ~ 4.

**Description of approach 2:**

- 1) SP measurement in KCl/water solution with pH ~ 6,
- 2) SP measurement in a NaPSS solution with the same pH and ionic strength as step 1,
- 3) repeating step 1,
- 4) SP measurement in KCl/water solution with pH ~ 4,
- 5) SP measurement in KCl/water solution with pH ~ 9,
- 6) repeating step 4.

**3.3.2 *Ex situ* monitoring**

Another approach for studying the behavior of the PE in the AAO nanochannels is the *ex situ* experiments. First, the streaming potential measurement is done on the AAO piece in KCl solution at a given pH and ionic strength to determine the bare AAO  $\zeta$ -potential. Afterwards, the membrane is

taken out and immersed in a beaker containing the NaPSS solution with the desired concentration for a specific time. After immersion, the membrane is rinsed in KCl solution in order to remove the excess PE solution from the membrane outer surface. The streaming potential apparatus is then assembled with this membrane and is filled with the KCl solution and the streaming potential is measured for around 5 minutes. This approach is used in order to have insights on the possible effect of pressure gradient on the diffusion and adsorption of the PSS inside the AAO nanochannels and to discuss the mechanisms of the transport of the PSS macromolecules inside the AAO nanochannels: either it is governed mainly by diffusion or by the convection flow.

### **3.4 The in-situ experiments with styrene sulfonate monomers inside the nanochannels of the AAO membranes**

The other in-situ  $\zeta$ -potential measurements were done with the electrolyte solutions containing the sodium styrene sulfonate monomers. These measurements were done in order to compare the interaction of the monomers with the macromolecules and also to check the extent of the coverage of the inner surface of the AAO nanochannel with the oppositely charged monomer. There is an unclarified speculation about the completion of the coverage of the interior surface of the AAO nanochannels by the PSS polymer chains. Since the hydrodynamic diameter of the PSS macromolecules is comparable with the diameter of the nanochannels, it is challenging to ascertain the whole surface of the nanochannels to be accessible with macromolecules. For this reason, it was decided to make streaming potential measurements through the AAO nanochannels in contact with styrene sulfonate monomers. It was hypothesized that the monomers can reach to all parts of the nanochannels due to their small size and consequently be adsorbed by virtue of their small size. It is expected that the styrene sulfonate monomers change the sign of the surface charge of the nanochannels upon their adsorption. By achieving the same final value for the  $\zeta$ -potential inside the nanochannels after styrene sulfonate adsorption with the case of PSS macromolecules, it can be hypothesized that the polyelectrolyte molecules reach to all regions of the surface. We have a similar sequence for the *in situ* measurements the steps of which are as follows similar to those in-situ experiments done with macromolecules:

- 1) SP measurement in KCl solution with the specific ionic strength

- 2) SP measurement in a solution with the ionic strength same as step 1 and a specific monomer concentration,
- 3) repeating step 1,
- 4) repeating step 2 (steps 1 and 2 can be repeated consequently for some times).

## 3.5 Results and discussion

### 3.5.1 The diffusion rate and kinetics of adsorption

In our research work, in order to investigate the rate of diffusion of the PSS macromolecules inside the nanochannels, we utilized the  $\zeta$ -potential versus time curves. These curves were our means of tracking of the transfer and adsorption of the PSS macromolecules inside the nanochannels. From the theoretical basis, we speculate the reliance of the rate of transfer and adsorption to different parameters shown in Figure 2. Thus, we aimed to find the dependence of the rate of this processes on the variables that we could change. Variables that we have changed in this work are namely:

- **Membranes thickness:** The nanochannel length that the macromolecules should migrate and the surface exposed for PE adsorptions.
- **Pores diameters:** The space that the macromolecules have got for migration. This variable also shows the curvature of the surface exposed to the macromolecules.
- **Ionic strength:** This variable changes the hydrodynamic diameter of the polyelectrolyte macromolecules (they shrink more with higher ionic strength), the screening length of the electrostatic interactions and also the thickness of the electrical double layer (Debye length) which changes the space available for the macromolecules to migrate and the extent to which they can approach the surface of the oxide. The Debye length is calculated by using equation 3-6:

$$\lambda_D = \sqrt{\frac{\epsilon_r \epsilon_0 k_B T}{2e^2 I}} \quad (3-6)$$

Where  $\epsilon_0$  is the permittivity of free space,  $\epsilon_r$  is the dielectric constant of the fluid,  $k_B$  is the Boltzmann constant and  $T$  is the temperature in kelvins. The elementary charge is shown by  $e$  and  $I$  is the ionic

strength of the solution. We have calculated at room temperature the Debye length of our aqueous solutions and found values of 9.7, 3, 1.4 and 1 nm in KCl solutions of 1, 10, 50 and 100 mM respectively. Thus, by increasing the ionic strength, the screening length reduces and accordingly the space occupied by the EDL in nanochannels reduces and there is more space available to PSS macromolecules to diffuse through.

- **pH:** By changing this variable, the surface charge density of the oxide surface will change. By getting further from the IEP point, the charge density increases. Thus, the amount of the charges that must be compensated by the polyelectrolyte macromolecules will increase.

### 3.5.1.1 Effect of AAO thickness

In discussing the parameters affecting the kinetics of the diffusion and adsorption process of the polyelectrolytes inside the charged nanochannels, we start with the AAO thickness. In Figure 3-4 the in situ  $\zeta$ -potential vs time curves of the AAO membranes in contact with NaPSS solution containing 0.5 g/L of NaPSS are depicted. We can see that for the oxalic acid synthesized AAOs, all curves approach approximately a unique value that depends on the ionic strength and the pH of the solution. The quantitative analysis of the data is shown in Figure 3-5. For each figure in Figure 3-4, we have a corresponding figure in Figure 3-5 depicted in terms of  $\zeta/\zeta_0$  which is the ratio of the  $\zeta$ -potential at each point divided by the initial value of the  $\zeta$ -potential measured in a solution with the same ionic strength and pH but without polyelectrolyte. For accurate fitting, equation 3-7 has been used to report the characteristic times and it is shown in the figures as Fit 2. The fit on the data with equation 3-5 is shown as Fit1:

$$\zeta_r(t) = A \exp\left(-\frac{t}{\tau_1}\right) + B \exp\left(-\frac{t}{\tau_2}\right) + C \quad (3-7)$$

where A, B and C are the fit coefficients. C shows the final value to which the curve approaches. B is a coefficient and along with the second exponential term fixes the fit on the data points. This term vanishes in some conditions. At time  $t = 0$  we these coefficients should satisfy the condition:  $A+B+C = 1$ .

By adding one exponential term, the fitted curve showed a better match with the experimental data in the short time in particular. In this manuscript equation (3-7) is used for the fitting on the data because equation (3-5) cannot reproduce our data accurately in majority of the cases.

This leads to some speculations. Such as: the process of adsorption of macromolecules on the internal surface of AAO is governed by several mechanisms. Some of these mechanisms may become negligible in some concentrations and geometric conditions. Hence, the second exponential term vanishes for some membrane thicknesses and polyelectrolyte concentrations. We have presented this analysis for all of the proceeding figures.

After each of our figures in this chapter, there is a table showing the fitting parameters of the data on equation 3-7 and also the initial and final zeta potential value in the  $\zeta$ -t curve. For the measurements that the final value was not reached, it is written N.R. (which stands for Not Reached) in the column of  $\zeta_{\text{final}}$ .

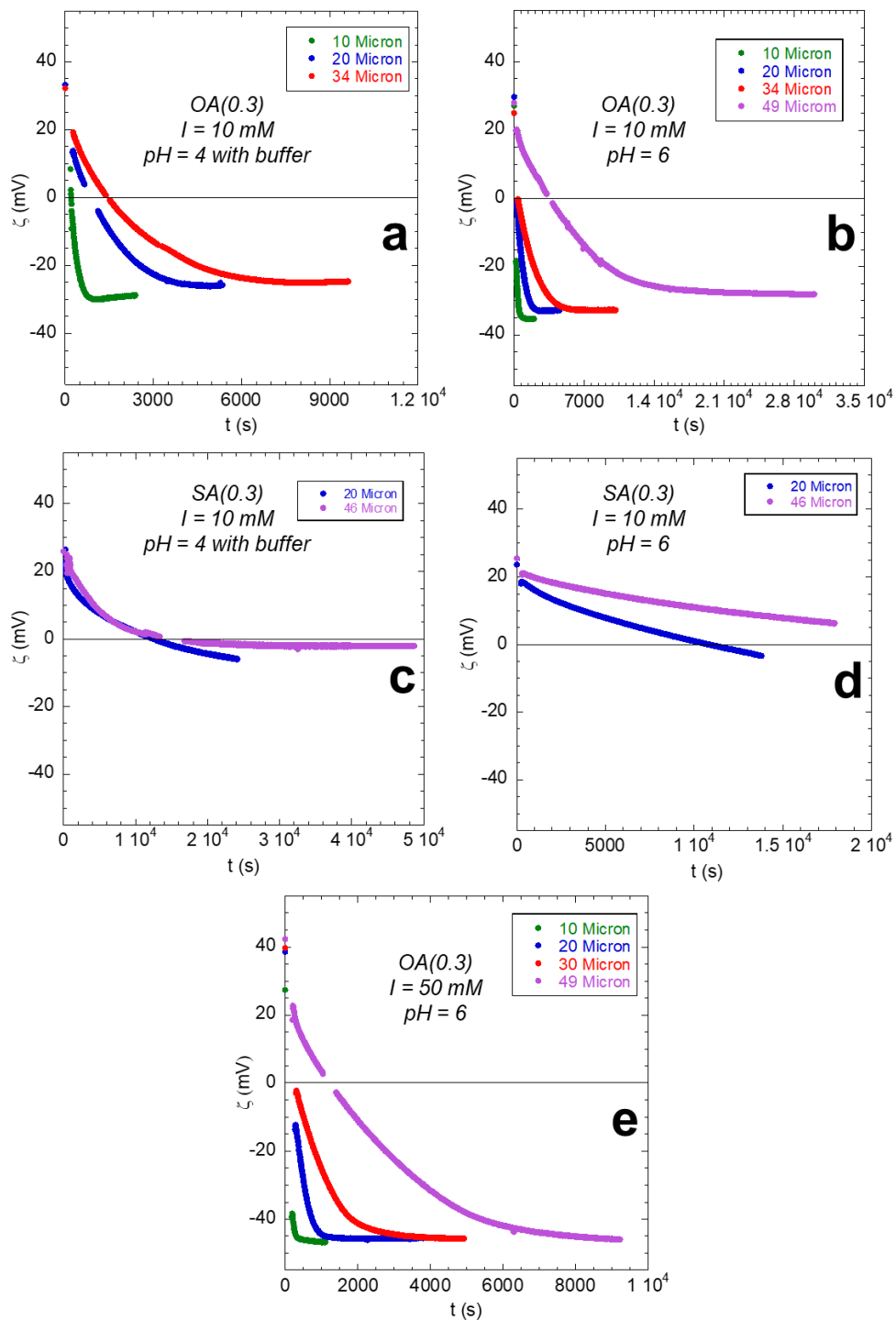


**Figure 3-4** *In situ*  $\zeta$ -potential versus time curves for membranes with different thicknesses in contact with solutions with ionic strength of 10 mM (except figure e) and PSS 70 kDa concentration of 0.5 g/L. **a)** Oxalic acid (0.3 M) synthesized membranes in pH = 4 with buffer, **b)** Oxalic acid (0.3 M) synthesized membranes in pH = 6, **c)** sulfuric acid (0.3 M) synthesized membranes in pH = 4 with buffer, **d)** sulfuric acid (0.3 M) synthesized membranes in pH = 6 and **e)** oxalic acid (0.3 M) synthesized membranes in ionic strength of 50 mM and pH = 6.

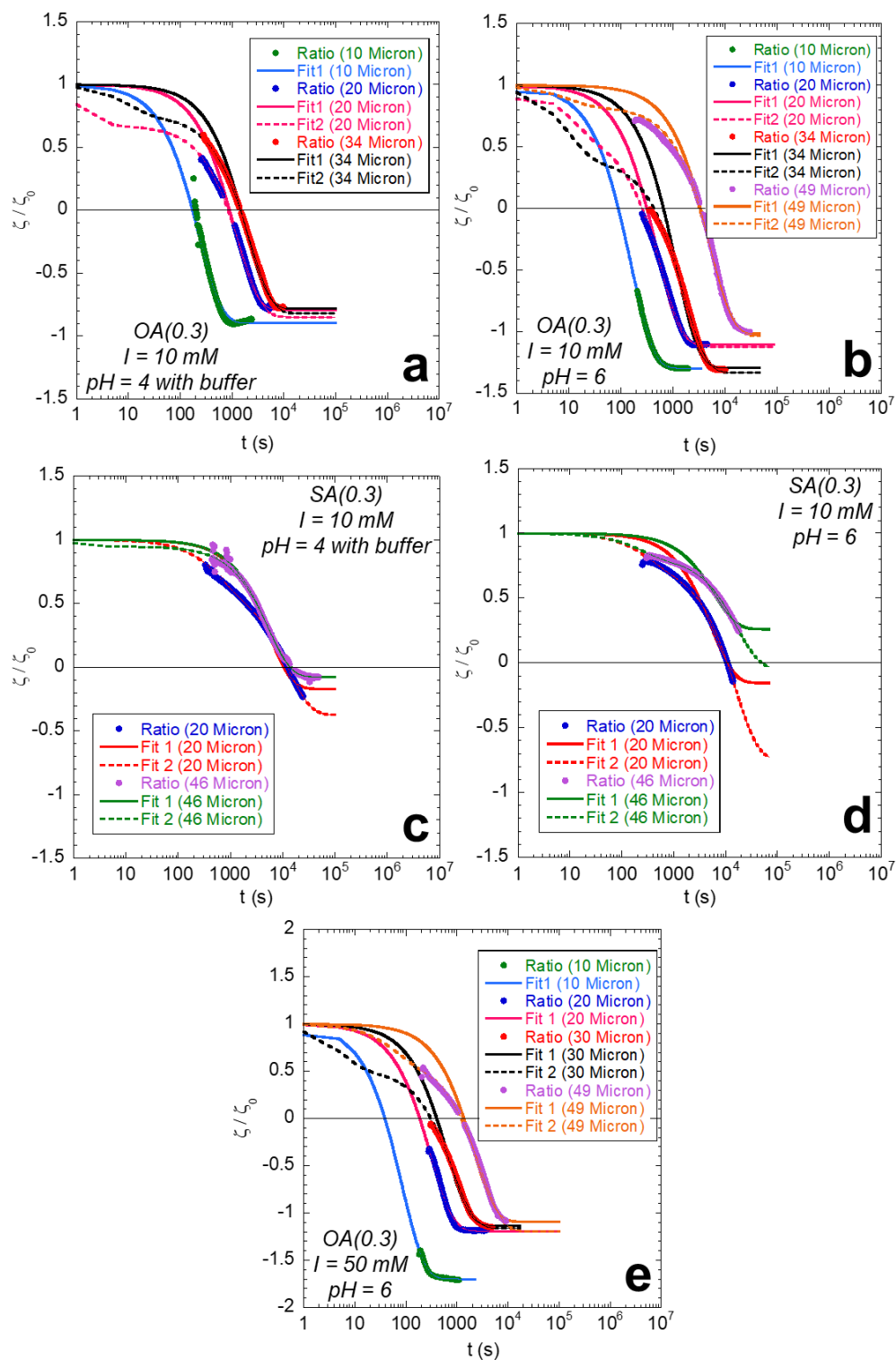


**Figure 3-5**  $\zeta/\zeta_0$  versus time figures for the data presented in graphs of figure 3. **a)** Oxalic acid (0.3 M) synthesized membranes in pH = 4, **b)** Oxalic acid (0.3 M) synthesized membranes in pH = 6, **c)** sulfuric acid (0.3 M) synthesized membranes in pH = 4, **d)** sulfuric acid (0.3 M) synthesized membranes in pH = 6 and **e)** oxalic acid (0.3 M) synthesized membranes in ionic strength of 50 mM and pH =6. Fit 1 consists of one exponential term and Fit 2 of two exponential terms.

Table 3-1 Fitting parameters of Figure 5 curves

Membrane code	Thickness ( $\mu\text{m}$ )	A	B	C	$\tau_1$	$\tau_2$	$\zeta_0$ (mV)	$\zeta_{\text{final}}$ (mV)
<b>Figure 3-5a (pH = 4 with buffer, I = 10 mM)</b>								
OA(0.3)-14	10	1.9	0	-0.9	232	-	33.2	-28.8
OA(0.3)-11	20	1.52	0.33	-0.85	1446	1.5	33.3	-25.8
OA(0.3)-9	34	1.58	0.24	-0.82	2223	10.5	32.2	-24.7
<b>Figure 3-5b (pH = 6, I = 10 mM)</b>								
OA(0.3)-14	10	2.3	0	-1.3	157	-	27.2	-35.3
OA(0.3)-11	20	1.72	0.4	-1.12	600	12.2	29.7	-32.8
OA(0.3)-9	34	1.74	0.6	-1.33	1620	12.9	25	-32.7
OA(0.3)-5	49	1.86	0.17	-1.04	5518	10	27.9	-28.4
<b>Figure 3-5c (pH = 4 with buffer, I = 10 mM)</b>								
SA(0.3)-11	24	1	0.37	-0.37	12600	580	25.9	N.R.
SA(0.3)-9	46	1.03	0.05	-0.05	5426	1.5	24.8	-1
<b>Figure 3-5d (pH = 6, I = 10 mM)</b>								
SA(0.3)-11	24	1.68	0.37	-1.05	14840	653	23.2	-24
SA(0.3)-9	46	0.86	0.18	-0.04	16760	225	25.5	N.R.
<b>Figure 3-5e (pH = 6, I = 50 mM)</b>								
OA(0.3)-14	10	2.7	0	-1.7	84	-	27.4	-46.7
OA(0.3)-8	20	2.2	0	-1.2	307	-	38.6	-45.6
OA(0.3)-7	30	1.69	0.47	-1.16	827	5.6	39.7	-45.7
OA(0.3)-5	49	1.81	0.38	-1.2	2915	60	42.3	-45.9

By considering the different figures in Figure 3-4, there is a systematic trend of change of the  $\zeta$ -t figures with the thickness of the membranes synthesized in oxalic acid 0.3 M (Figures 3 a, b, e). The changes are observed both visually and quantitatively (by considering the fitting parameters). As we can see, by increasing the thickness of the membrane, the time to reach to the equilibrium final value (also referred as the plateau value) increases. This can be due to some facts that we explain. First, by increasing the thickness of the membrane, two variables increase. The first is the surface that is exposed to the coverage with the polyelectrolyte. Considering the internal surface of the channels to be covered by the polyelectrolyte macromolecules, the area increases linearly with the thickness of the membrane which is also the pore length. The second variable that changes with the thickness is the diffusion time that increases for the macromolecules to reach themselves to the adsorption site.

For the case of sulfuric acid 0.3 M synthesized AAOs in pH = 4 (Figure 3-4c), the situation is different: the curves seem to be so close. But in pH = 6 the change in the thickness is again pronounced. The difference between these two situations can be explained as follows:

In a pH further from the isoelectric point, the charge density of the surface of the AAO nanochannels increase. Thus, the electrostatic interactions between the charged surface of the alumina and the PSS macromolecules increase. Accordingly, more PSS chains adsorb in the entrance of the nanochannels and cause a considerable decrease in the diameter of the entrance. This causes the reduction of the rate of the change of the  $\zeta$ -potential with time. But, for the case of pH = 6, since the adsorption according to lower surface charge density of AAO, the entrance does not approach blockage and there is space for the entrance of the PSS chains. Accordingly, the difference between the 46 Micron and 20 Micron curves in this pH is obvious. And we can see that the  $\zeta$ -potential value of the 20 Micron thick membrane has crossed zero value much faster than that of the 40 Micron membrane.

### 3.5.1.2 Effect of PE concentration

The other parameter that can affect the rate of the diffusion and adsorption of the PSS chains inside the AAO nanochannels is the concentration of the PE solution. In Figure 3-6 we have presented the  $\zeta$ -t data of sulfuric and oxalic acid 0.3 M synthesized AAOs using two different PE concentrations namely 0.5 and 1.5 g/L. The figures are presented along with the Ratio and fit graphs corresponding to them. The fitting parameters are presented in Table 3-2.

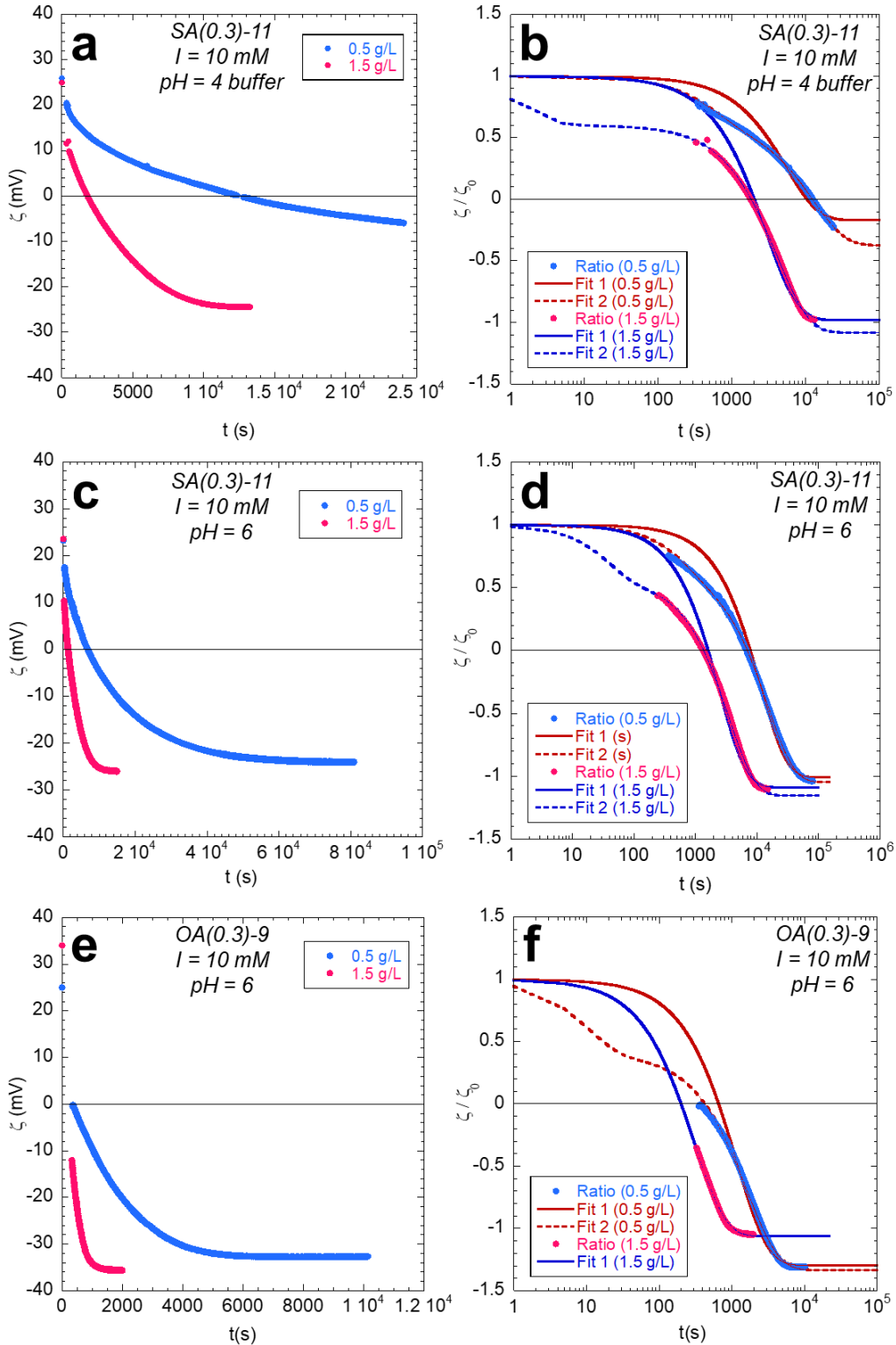


**Figure 3-6**  $\zeta$ - $t$  curves comparing the 0.5 g/L (in blue) and 1.5 g/L (in pink) NaPSS concentrations and the corresponding figures showing the data in terms of ratio to the initial  $\zeta$ -potential value and the fits. The ionic strength of all the solutions has been adjusted on 10 mM. **a)** SA(0.3)-11 in pH = 4 and **b)** ratio and fits. **c)** SA(0.3)-11 in pH = 6 and **d)** ratio and fits. **e)** OA(0.3)-9 in pH = 6 and **f)** ratio and fits.

Table 3-2 Fitting parameters of Figure 3-6 curves

Membrane code	NaPSS (g/L)	A	B	C	$\tau_1$	$\tau_2$	$\zeta_0$ (mV)	$\zeta_{\text{final}}$ (mV)
<b>Figure 3-6b (pH = 4 with buffer, I = 10 mM)</b>								
SA(0.3)-11	0.5	1	0.37	-0.37	12600	580	25.9	N.R.
	1.5	1.69	0.4	-1.08	4128	14	25	-24.4
<b>Figure 3-6d (pH = 6, I = 10 mM)</b>								
SA(0.3)-11	0.5	1.68	0.37	-1.05	14840	653	23.2	-24
	1.5	1.71	0.45	-1.15	3478	39	23.6	-26
<b>Figure 3-6f (pH = 6, I = 10 mM)</b>								
OA(0.3)-9	0.5	1.735	0.6	-1.33	1620	12.9	25	-32.7
	1.5	2.06	0	-1.06	302	-	34	-35.7

Analyzing the figures in Figure 3-6 and the fitting parameters and time constants in Table 3-2, we can see that the rate of the change of  $\zeta$ -potential with time increases sharply with changing the PSS concentration from 0.5 to 1.5 g/L, presumably due to the higher concentration gradient that is maintained between the bulk and the interior of the nanochannels. In case we consider a simple diffusion mechanism for the transport of the PSS chains to the interior part of the nanochannels and adsorption on the surface, according to Fick's law, the flux of diffusion is proportional to the concentration gradient ( $J = -D \frac{\partial C}{\partial x}$ ) where D is the diffusion coefficient of the studied species in the environment. Thus, if only the Fick's law governs the transport, an increase with a factor of 3 is expected in the flux in case of increasing the concentration gradient by a factor of three. Thus, a considerable increase in the rate of the change of the  $\zeta$ -potential with time in case of higher concentration is reasonably expected. The specific times of the fits for the SA(0.3)-11 membrane are 12600 and 4128 s in pH = 4, and 14840 and 3478 s in pH = 6 for the 0.5 g/L and 1.5 g/L concentrations respectively. The ratio of the specific times is 3 in pH = 4 but in pH = 6 it is around 4.5. For the case of the membrane OA(0.3)-9 and pH = 6, the characteristic times are 1620 and 300 for the 0.5 and 1.5 g/L concentrations, respectively, giving a ratio of 5.3. From these ratios one can

suggest that the simple diffusion cannot fully explained the characteristic time evolution with PE concentration.

### 3.5.1.3 Effect of ionic strength

The rate of the diffusion and adsorption of the PSS inside nanochannels of AAO is also expected to vary with the ionic strength of the solution. For this case, we conducted *in situ*  $\zeta$ -potential measurements with different AAOs membranes in PE solutions at 0.5 g/L with different KCl concentrations ranging from 1 to 100 mM. Figure 3-7 shows the different  $\zeta$ -t curves obtained for KCl concentrations and Figure 3-8 shows the corresponding of  $\zeta / \zeta_0$  curves with the fits. The fitting parameters are presented in Table 3-3.

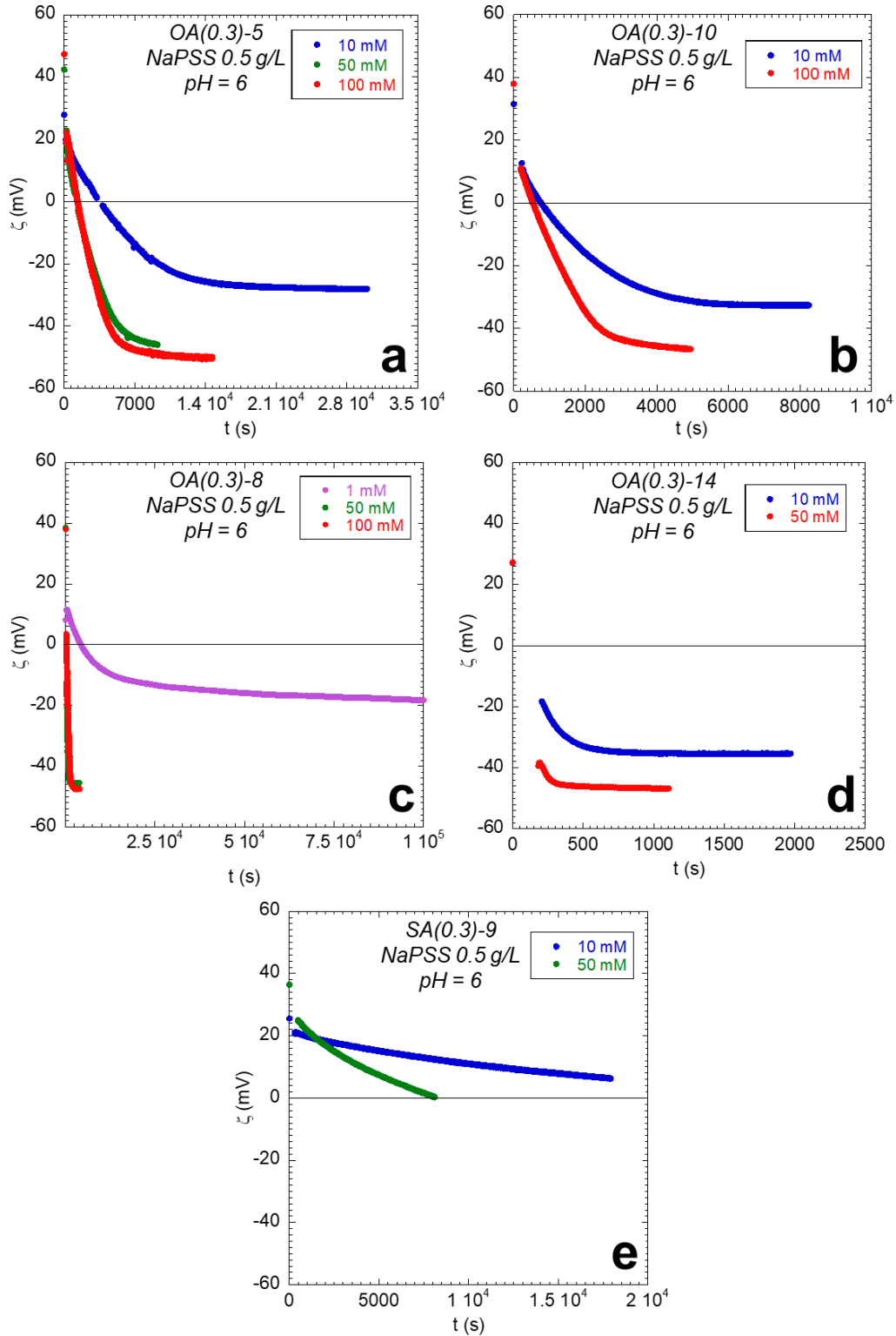


**Figure 3-7**  $\zeta$ - $t$  curves of membranes **a)** OA(0.3)-5, **b)** OA(0.3)-10, **c)** OA(0.3)-8, **d)** OA(0.3)-14 and **e)** SA(0.3)-9 in PSS concentration 0.5 g/L, pH = 6 and different KCl concentrations.

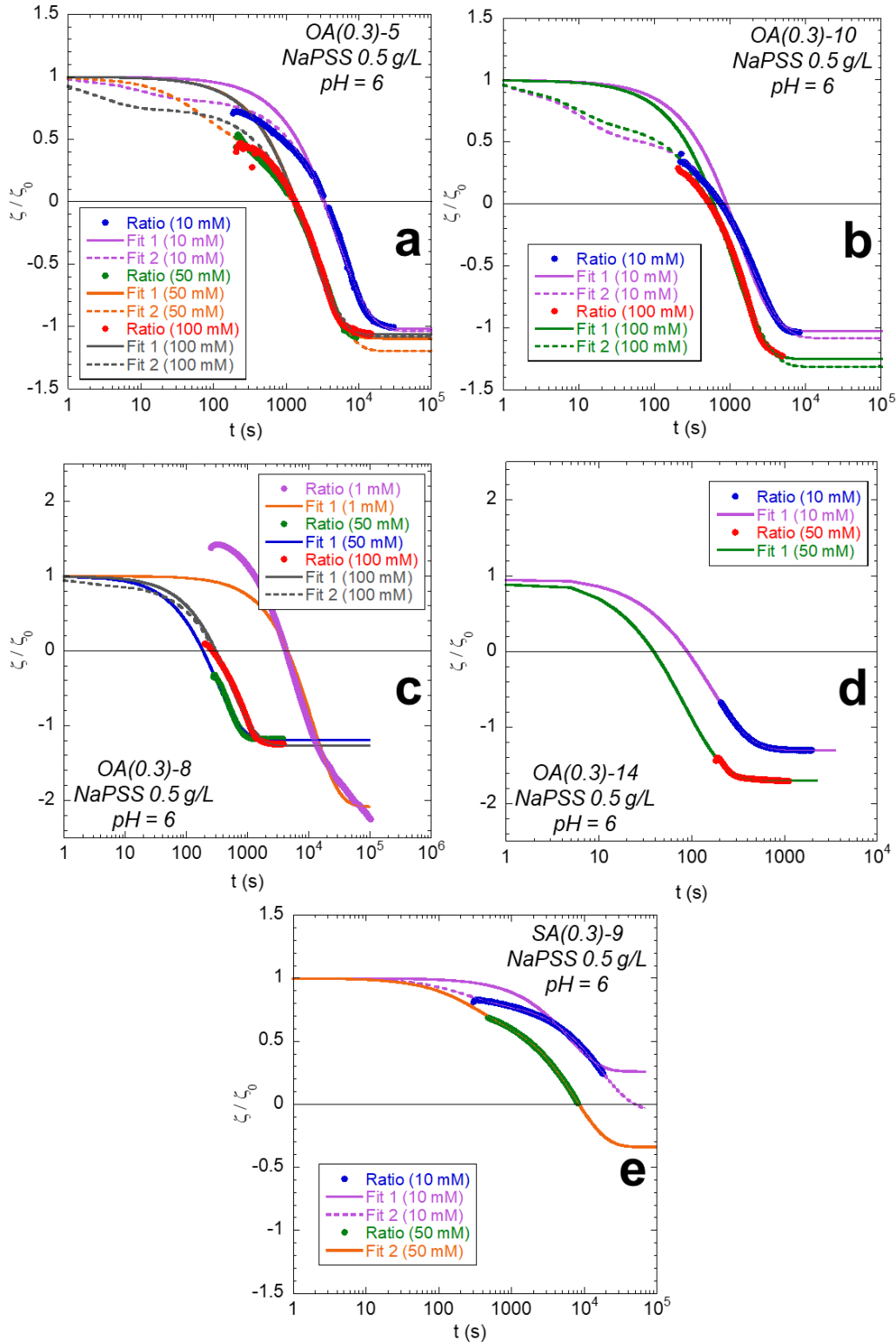


**Figure 3-8**  $\zeta$  Ratio- $t$  curves and fits of membranes **a)** OA(0.3)-5, **b)** OA(0.3)-10, **c)** OA(0.3)-8, **d)** OA(0.3)-14 and **e)** SA(0.3)-9 in PSS concentration 0.5 g/L, pH = 6 and different KCl concentrations.

Table 3-3 Fitting parameters of Figure 3-8 curves.

Membrane code	Ionic strength (mM)	A	B	C	$\tau_1$	$\tau_2$	$\zeta_0$ (mV)	$\zeta_{final}$ (mV)
<b>Figure 3-8a (pH = 6, NaPSS 0.5 g/L, <math>L_P = 49 \mu\text{m}</math>)</b>								
OA(0.3)-5	10	1.86	0.17	-1.04	5518	10	27.9	-28.4
	50	1.81	0.38	-1.2	2915	60	27.9	-28.1
	100	1.831	0.25	-1.08	2374	2.8	47.3	-50
<b>Figure 3-8b (pH = 6, NaPSS 0.5 g/L, <math>L_P = 32 \mu\text{m}</math>)</b>								
OA(0.3)-10	10	1.64	0.44	-1.08	1850	10.3	31.5	-32.6
	100	1.98	0.34	-1.31	1315	8.7	37.9	-46.6
<b>Figure 3-8c (pH = 6, NaPSS 0.5 g/L, <math>L_P = 20 \mu\text{m}</math>)</b>								
OA(0.3)-8	1	3.1	0	-2.1	11550	-	8.1	N.A.
	50	2.2	0	-1.2	307	-	38.6	-45.6
OA(0.3)-16	100	2.16	0.11	-1.27	546	1.5	38	-47.3
<b>Figure 3-8d (pH = 6, NaPSS 0.5 g/L, <math>L_P = 10 \mu\text{m}</math>)</b>								
OA(0.3)-14	10	2.3	0	-1.3	157	-	27.2	-35.3
	50	2.7	0	-1.7	84	-	27.4	-46.7
<b>Figure 3-8e (pH = 6, NaPSS 0.5 g/L, <math>L_P = 46 \mu\text{m}</math>)</b>								
SA(0.3)-9	10	0.86	0.18	-0.04	16760	225	25.5	N.R.
	50	1.06	0.28	-0.34	7414	266	36.7	N.A.

The curves in Figure 3-7 clearly show the effect of the ionic strength on the diffusion and adsorption process of NaPSS chains inside the AAO nanochannels. The effect of ionic strength on this phenomenon can be considered from different aspects. First of all, as calculated previously, the Debye length varies from 9.7, 3, 1.4 and 1 nm for KCl concentration of 1, 10, 50 and 100 mM, respectively. Thus, by increasing the ionic strength, the screening length reduces and accordingly the space occupied by the EDL in nanochannels reduces and there is more space available to PSS macromolecules to diffuse through it. The other effect of the ionic strength on the system is the hydrodynamic size of the NaPSS macromolecules. The screening length decreases when the ionic strength increases and the electrostatic repulsion forces between the monomers are reduced. Accordingly, the PE macromolecules shrink more and will have a smaller hydrodynamic diameter along with thinner EDL being formed around them. Thus, the macromolecules will have more freedom to displace according to their lower hydrodynamic diameter and also the more space that they have in the nanochannels for displacement. As observed in Figure 3-7a, the difference between 50 mM and 100 mM KCl concentration is not majorly observed. It can be explained by the fact that at high salt concentration the Debye length remains small. By considering the plateau values of the graphs, we can see that in a unique ionic strength, all the curves tend approximately to the same value, suggesting that the PE behavior at equilibrium (conformation, adsorbed amount) is similar at the surface independently of the AAO membrane. In case it is true, along with this hypothesis, the difference in the plateau values can be explained by possible differences in the PE conformation or adsorbed amount on the metal oxide surfaces at different ionic strengths. Some researchers have confirmed the increment of the amount of the polyelectrolyte adsorbed on the metal oxide surface with increasing the ionic strength [151]. This can be explained by the balance of the interactions as discussed by Hoogeveen et al [106], where the main interaction between the polyelectrolyte and the metal oxide surface is electrostatic, by overcompensation of the surface charge the repulsion force increases. Once the salt is increased, this repulsion force is screened and the adsorbed amount tends to increase. Although the increase in the salt concentration and the ionic strength tends to increase the adsorbed amount of polyelectrolyte, this increment in the adsorbed amount is not constant. By increasing the salt concentration, salt counterions also compete with the polyelectrolyte segments in adsorption to the metal oxide surface charged sites. So, up to a specific level of ionic strength the trend is increasing and at some point it may decrease and tend to zero. But, in our range of ionic strength, the increasing level of adsorption with increasing the ionic is observed. It can be seen from Figure 3-7c that the rate of the process has decreased considerably by lowering the KCl concentration to 1 mM to the extent that the curve has

not reached to a plateau. This observation is in line with what was theoretically discussed. The hydrodynamic diameter of the macromolecules is expected to be higher than in the case of lower ionic strengths. Besides, the EDL thickness is also higher than the previous situations of higher ionic strength which limits the transfer space. Thus, in very low ionic strength, both the space is limited and also the molecules hydrodynamic size is higher. These two factors thus reduce the rate of diffusion and adsorption. Besides, in lower ionic strength, another phenomenon that slows the process is the repulsion between the molecules due to the higher screening length. Which means that negatively charged macromolecules can have repulsive interactions from further distances which can render the entrance of the macromolecules in the nanochannels being diffracted by those that are already in the nanochannel.

For the case of sulfuric acid synthesized AAO membrane depicted in Figure 3-7e, although the curves have not reached to the plateau value within the experiment time interval, we can see that the rate of decrease in the  $\zeta$ -potential is higher in 50 mM ionic strength compared to the 10 mM as we can see after around 8000 s the  $\zeta$ -potential of the 50 mM curve has reached zero while the  $\zeta$ -potential in 10 mM is still positive after 18000 s.

Afterwards, we have studied the difference of the rate of the diffusion and adsorption process between the membranes synthesized in sulfuric acid and oxalic acid. As mentioned in the previous chapters, these membranes have different morphological properties such as the diameter of the nanochannels  $D_p$ , the nanochannel length  $L_p$  and also the pore density in a unit area. The total surface of the nanochannels exposed to the PE adsorption of a AAO membrane of lateral surface  $A$  is:

$$\text{Total surface exposed} = \text{Pore density (cm}^{-2}\text{)} \cdot A \cdot \pi \cdot D_p \cdot L_p$$

Considering a  $L_p$  of 20 microns and a pore density of  $10^{10}$   $\text{cm}^{-2}$  and  $2.5 \times 10^{10}$   $\text{cm}^{-2}$  for OA and sulfuric acid AAO membranes, respectively, a  $D_p$  of 45 and 27 nm, respectively, the total surface exposed is of 282.7  $\text{cm}^2$  and 424.1  $\text{cm}^2$  for OA and sulfuric acid respectively (if one takes  $A = 1 \text{ cm}^2$ ). Thus, for a similar AAO thickness, the total surface exposed is 1.50 times more for sulfuric AAO. But, once we analyzed the  $\zeta$ -t curves of the sulfuric and oxalic acid synthesized membranes in Figure 3-9, we can observe that the ratio of the rates does not follow the same ratio and the rate of the change of the nanochannels surface charge is much lower in sulfuric acid synthesized membranes. Quantitatively speaking, for the case of 20  $\mu\text{m}$  thick membranes at  $\text{pH} = 6$  and 10 mM KCl (Figures 3-9 c,d), the characteristic time for the OA AAO is approximately 600 s while for the sulfuric acid AAO it is about

15000 s. The ratio of these two characteristic times is far beyond the ratio of the total surface exposed of 1.5. Thus, pure geometrical consideration cannot explain this discrepancy, the increased curvature of the sulfuric acid nanochannels has brought complexities to the process. As we can see, the plateau value of the sulfuric acid membrane is higher than that of the oxalic acid membrane but their plateaus ratio values are almost the same. As we showed in chapter two, the IEP point of the internal surfaces of the sulfuric, oxalic and selenic acid synthesized membranes are almost similar (9 and 9.4). Hence, it is possible to consider the charge density of the internal surfaces of these membranes are similar. With surface ratio of around 1.5 and similar charge density, the reason of the highly slower rate of the process for the sulfuric acid synthesized membrane should be sought in the other parameters such as the diameter of the nanochannels because in case the diameter of the nanochannels approaches the diameter of gyration of the macromolecule ( $2 \times R_g$ ), the macromolecule can be considered to be confined in the nanochannel. This is the case for the PSS macromolecules used in our research and the sulfuric acid synthesized membranes. The  $D_p$  of the AAO membranes synthesized membranes is around 27 nm and the  $2 \times R_g$  value for the PSS macromolecules with the molecular weight and the ionic strength that we have worked is approximately 24 nm. Due to the proximity of the  $D_p$  and  $2 \times R_g$ , we can consider the PSS macromolecule to be confined in the nanochannels of the sulfuric acid synthesized AAO membrane and the considerably slower rate of the diffusion and adsorption process in sulfuric acid synthesized membranes compared to oxalic acid synthesized membranes is by virtue of the effect of confinement. In Figure 4 of the Appendix, the  $\zeta$ -potential data from Figure 3-9c is presented, plotted against the square root of time and normalized by the internal surface area of the nanochannels within the membranes. By examining the ratio of the slopes observed in the linear segments of the curves within this figure, it can be inferred that the diffusion coefficient of PSS within the nanochannels of the oxalic acid membranes is approximately 6.8 times greater than that within the nanochannels of the sulfuric acid-synthesized membrane. This analysis effectively highlights the discernible impact of confinement on the diffusion properties.

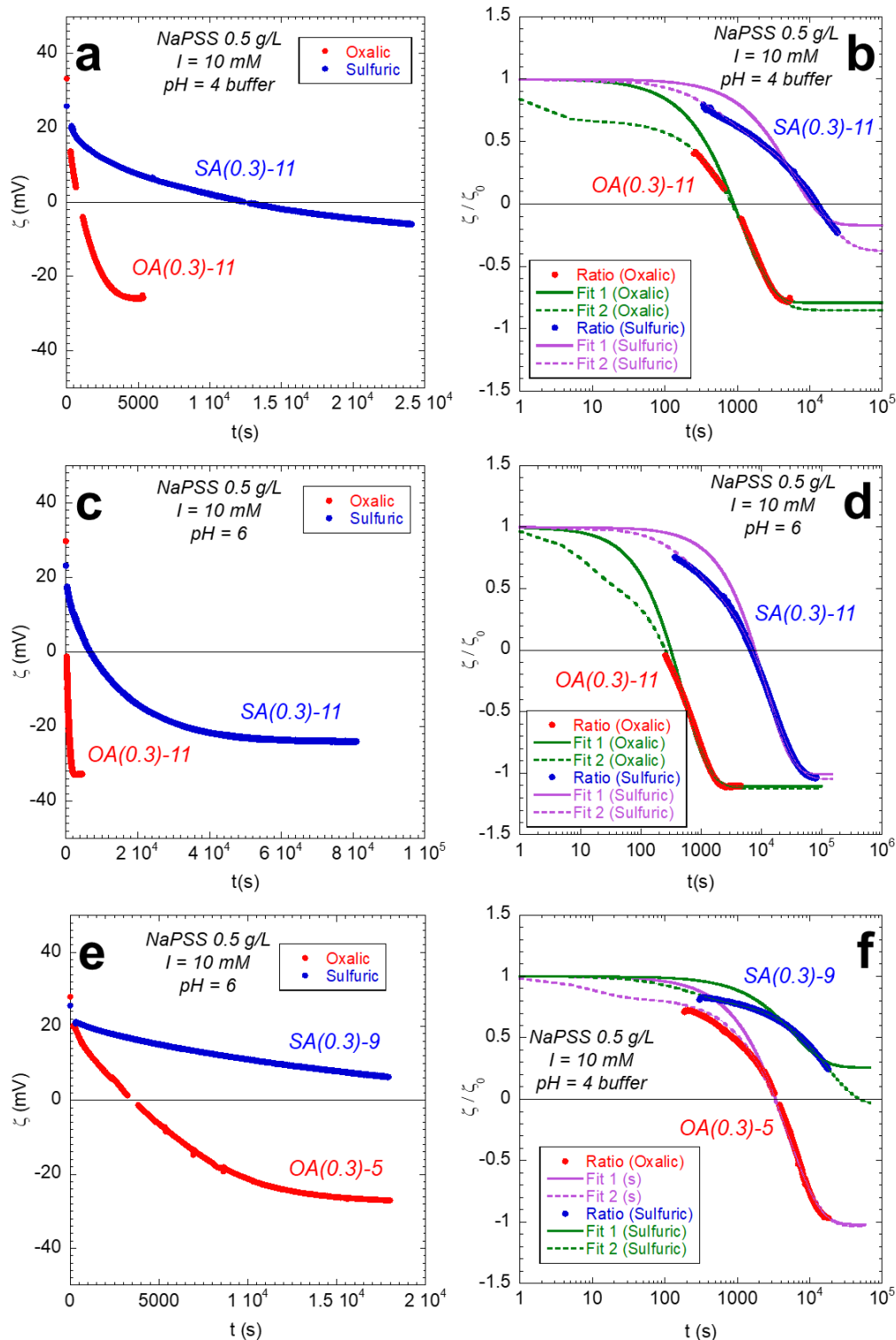


**Figure 3-9**  $\zeta$ - $t$  curves comparing the change of the  $\zeta$ -potential with time in AAO membranes synthesized with oxalic and sulfuric acid and the corresponding figures showing the data in terms of ratio  $\zeta/\zeta_0$  and the fits. The KCl concentration of all the solutions has been adjusted to 10 mM, and the concentration of the PSS is 0.5 g/L. **a)** SA(0.3)-11 and OA(0.3)-11 in pH = 4 and **b)** ratio and fits. **c)** SA(0.3)-11 and OA(0.3)-11 in pH = 6 and **d)** ratio and fits. **e)** SA(0.3)-9 and OA(0.3)-5 in pH = 6 and **f)** ratio and fits.

Table 3-4 Fitting parameters of Figure 3-9 curves.

Membrane code	Thickness ( $\mu\text{m}$ )	A	B	C	$\tau_1$	$\tau_2$	$\zeta_0$ (mV)	$\zeta_{\text{final}}$ (mV)
<b>Figure 3-9b (pH = 4 with buffer, NaPSS 0.5 g/L, I = 10 mM)</b>								
SA(0.3)-11	24	1	0.37	-0.37	12600	580	25.9	N.R.
OA(0.3)-11	20	1.52	0.33	-0.85	1446	1.5	33.3	-25.7
<b>Figure 3-9d (pH = 6, NaPSS 0.5 g/L, I = 10 mM)</b>								
SA(0.3)-11	24	1.68	0.37	-1.05	14840	653	23.2	-24
OA(0.3)-11	20	1.72	0.4	-1.12	600	12.2	29.7	-32.8
<b>Figure 3-9f (pH = 6, NaPSS 0.5 g/L, I = 10 mM)</b>								
SA(0.3)-9	46	0.86	0.18	-0.04	16760	225	25.5	N.R.
OA(0.3)-5	49	1.864	0.17	-1.04	5518	10	27.9	-28.1

### 3.5.1.4 Effect of pH

The other parameter that was considered affecting the rate of the diffusion and adsorption rate through the nanochannels of AAO membranes was the pH. For this, we have measured the  $\zeta$ -potential of the AAO membranes in NaPSS solution at a KCl concentration of 10 mM and at a pH values of 4 or 6. For maintaining the pH at 4, we mostly used  $\text{CH}_3\text{COOH}/\text{CH}_3\text{COO}^-$  buffer solution (4 mM) and for one case we also used HCl (for SA(0.3)-11 membrane with the PSS concentration 1.5 g/L). The solutions at pH = 6 correspond to solutions directly prepared in pure water.

Figures 3-10 and 3-11 show that there are differences in the  $\zeta$ -t curves when the pH is varied. First, in Figure 3-10 showing the  $\zeta$ -t curves of the oxalic acid synthesized membranes having different lengths (10, 20 and 34 microns for OA(0.3)-14, OA(0.3)-11 and OA(0.3)-9, respectively), we can observe a change in the plateau value: -28 mV for pH = 4 and -36 mV for pH = 6. Then, the change in the rate of the process is not visually obvious but, by considering the characteristic time of the curves in Table 3-5, we can see that the characteristic time is increased for the pH=4. For OA(0.3)-14 (10 microns thick, Figure 3-10 a,b) the characteristic times are 232 s and 157 s for the pH values of 4 and 6, respectively. For OA(0.3)-11 (20 microns, Figure 3-10 c, d) the characteristic times are 1446 s and

600 s for the pH values of 4 and 6, respectively and for OA(0.3)-9 (34 microns, Figure 3-10 e,f) the characteristic times are 2223 s and 1620 s for the pH values of 4 and 6, respectively. This shows that for the oxalic acid membranes, in pH = 4 the rate of the change of  $\zeta$ -potential and accordingly the surface charge of the nanochannels has decreased. Since PSS is a strong polyelectrolyte and dissociates completely in the whole pH range, the charge of the macromolecules is independent of the pH. Besides, the other variables such as the hydrodynamic diameter of the PSS and also the thickness of the EDL is independent of the pH of the environment. Furthermore, by considering the pH- $\zeta$  curves in chapter 2 for the AAO nanochannels surface, there is no considerable change in the  $\zeta$ -potential between pH values 4 (maintained with HCl) and 6. Thus the charge density of the surface between these two pH values should be similar. The change in the rate and the final value can be explained by the competition of the acetate species with PSS for adsorption on the surface.

Similar trend is observed for sulfuric AAOs. For SA(0.3)-11 (25 microns thick), Figure 3-11c,d show the  $\zeta$ -potential evolution with time and the diffusion and adsorption rate is also decreased in pH = 4 compared to pH = 6, for both 0.5 and 1.5 g/L PSS concentrations (Figure 3-11 e,f). One possible explanation is that the acetate buffer  $\text{CH}_3\text{COO}^-$  competes with the NaPSS chains for adsorption on the AAO nanochannels. To verify it, we performed a measurement in a pH=4 solution made with HCl. Figure 3-11e shows the corresponding data for 1.5 g/L NaPSS solution and we can see that the pH=4 in HCl is very close to the pH=6 curve. From the fits we obtained a characteristic time for pH = 6 of 3478 s and for pH = 4 in HCl a time of 3131 s. Such similarity tends to confirm the effect of acetate on the PSS adsorption behavior, which is more pronounced when the NaPSS concentration is lowered (see Figure 3-11 c,d for 0.5 g/L).

Form these observations, we realize that the acetate species compete with the polymers for adsorption. Thus it is better not to use them for maintaining the pH.

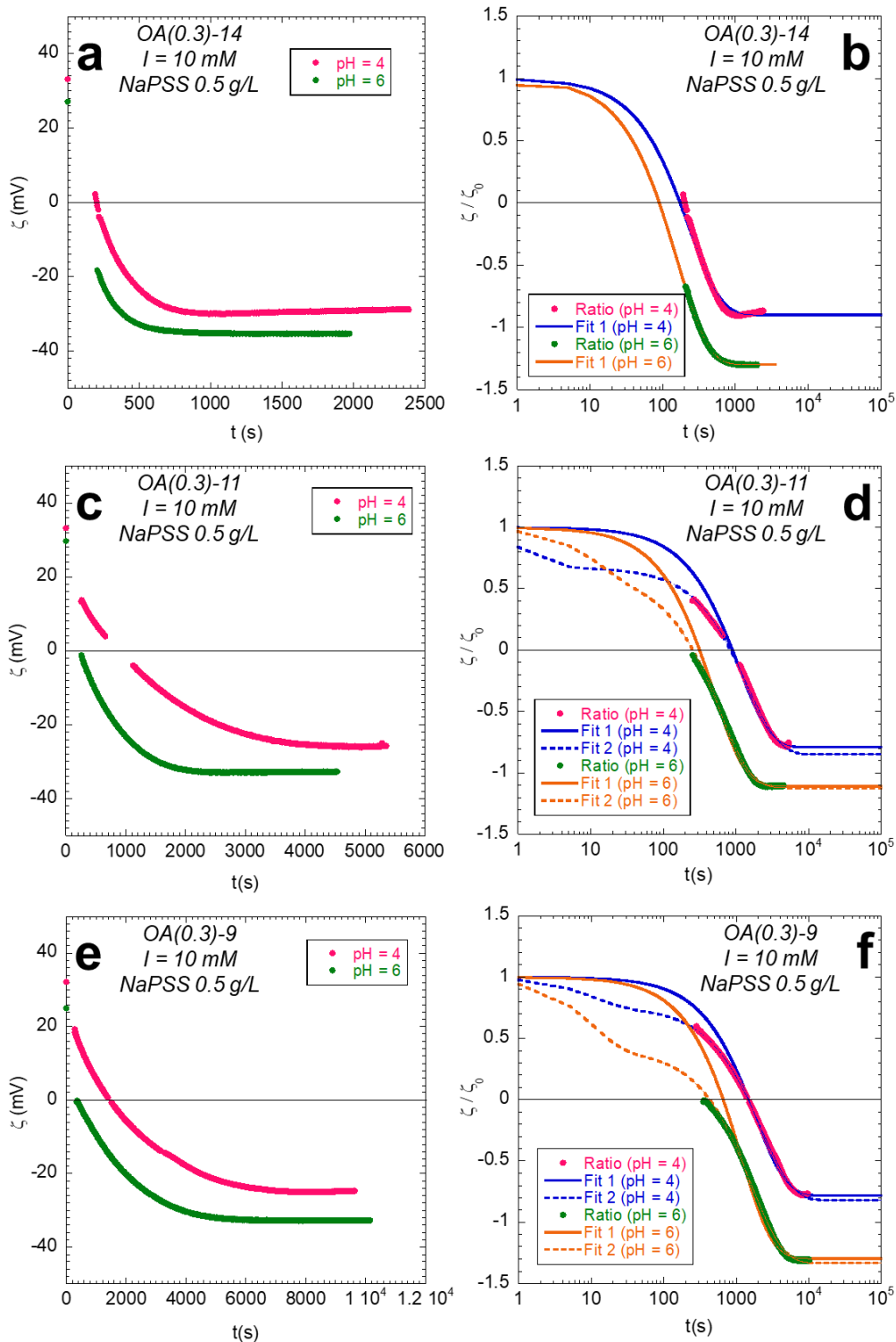


**Figure 3-10**  $\zeta$ - $t$  curves of the oxalic acid synthesized membranes at pH = 4 or 6 and the corresponding figures showing the data in terms of ratio to the initial  $\zeta$ -potential value and the fits. The ionic strength of all the solutions has been adjusted on 10 mM, and the PSS concentration on 0.5 g/L. **a)** OA(0.3)-14 (10 microns thick) and **b)** ratio and fits. **c)** OA(0.3)-11 (20 microns thick) and **d)** ratio and fits. **e)** OA(0.3)-9 (34 microns thick) in pH = 6 and **f)** ratio and fits.

**Table 3-5** Fitting parameters of Figure 3-10 curves.

Membrane code	pH	A	B	C	$\tau_1$	$\tau_2$	$\zeta_0$ (mV)	$\zeta_{final}$ (mV)
<b>Figure 3-10b (NaPSS 0.5 g/L, I = 10 mM)</b>								
OA(0.3)-14	4 Buffer	1.9	0	-0.9	232	-	33.2	-28.8
	6	2.3	0	-1.3	157	-	27.2	-35.3
<b>Figure 3-10d (NaPSS 0.5 g/L, I = 10 mM)</b>								
OA(0.3)-11	4 Buffer	1.52	0.33	-0.85	1446	1.5	33.3	-25.8
	6	1.72	0.4	-1.12	600	12.2	29.7	-32.8
<b>Figure 3-10f (NaPSS 0.5 g/L, I = 10 mM)</b>								
OA(0.3)-9	4 Buffer	1.58	0.24	-0.82	2223	10.5	32.2	-24.7
	6	1.74	0.6	-1.33	1620	12.9	25	-32.7

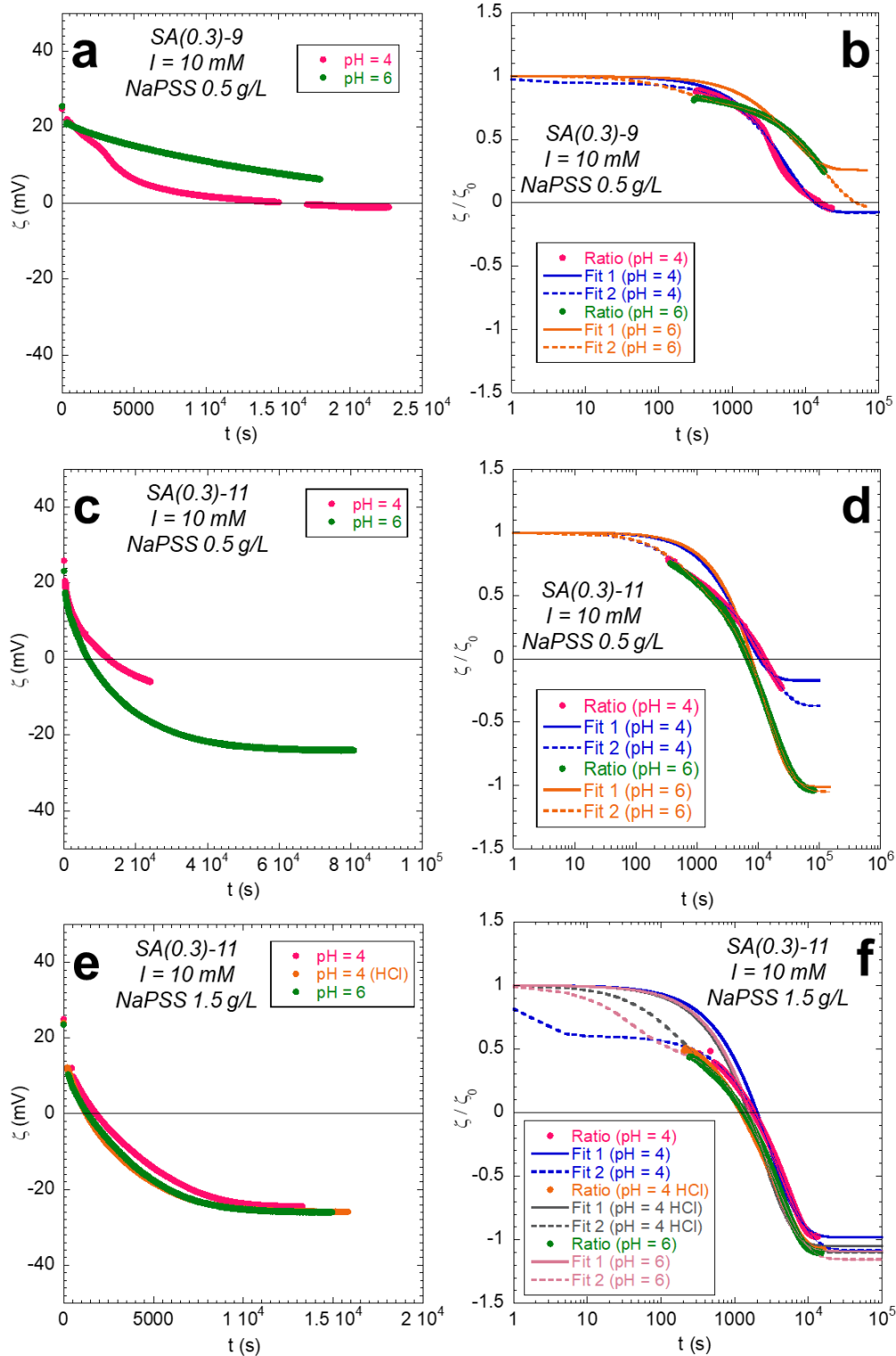


**Figure 3-11**  $\zeta$ - $t$  curves of the sulfuric acid synthesized AAO membranes comparing at pH values of 4 and 6 and the corresponding figures showing the data in terms of ratio to the initial  $\zeta$ -potential value and the fits. The ionic strength of all the solutions has been adjusted on 10 mM. **a)** SA(0.3)-9 (46 microns thick), PSS 0.5 g/L and **b)** ratio and fits. **c)** SA(0.3)-11 (25 microns thick), PSS 0.5 g/L and **d)** ratio and fits. **e)** SA(0.3)-11, PSS 1.5 g/L and **f)** ratio and fits.

**Table 3-6** Fitting parameters of Figure 3-11 curves.

Membrane code	pH	A	B	C	$\tau_1$	$\tau_2$	$\zeta_0$ (mV)	$\zeta_{final}$ (mV)
<b>Figure 3-11b (NaPSS 0.5 g/L, I = 10 mM)</b>								
SA(0.3)-9	4 Buffer	1.58	0.24	-0.82	2223	10.5	32.2	-24.7
	6	1.74	0.6	-1.33	1620	12.9	25	-32.7
<b>Figure 3-11d (NaPSS 0.5 g/L, I = 10 mM)</b>								
SA(0.3)-11	4 Buffer	1	0.37	-0.37	12600	580	25.9	N.R.
	6	1.68	0.37	-1.05	14840	653	23.2	-24
<b>Figure 3-11f (NaPSS 1.5 g/L, I = 10 mM)</b>								
SA(0.3)-11	4 Buffer	1.69	0.4	-1.08	4128	14	25	-24.4
	4 HCl	1.67	0.43	-1.1	3131	125	24	-26
	6	1.71	0.45	-1.15	3478	39	23.6	-26

### 3.6 In-Situ and Ex-Situ measurements

The driving force behind the diffusion and adsorption of NaPSS macromolecules inside the AAO nanochannels is still questionable: either it is purely conducted by diffusion, or it is accelerated by the hydraulic pressure gradient that is imposed between the two ends of the AAO membrane during *in situ* streaming potential measurements, i.e., due to convection effects. In order to have more insights to this matter, we also performed *ex situ*  $\zeta$ -potential measurements (see the details at the beginning of this chapter). In *ex situ* experiments the streaming potential is measured with KCl solution after the immersion of the AAO in the NaPSS solution. Thus, the transport of NaPSS chains in the nanochannel is a priori purely driven by diffusion since we don't impose any pressure gradient.

As we can see in Figure 3-12 a,b, for the 20  $\mu\text{m}$  thick OA AAO membrane, the *ex situ* measurement points fall exactly on the *in situ* points, suggesting that diffusion is the dominant phenomenon for the transport of NaPSS macromolecules inside the nanochannels and the convective flow induced by the pressure gradient during *in situ* measurement is negligible. The characteristic times

for the in-situ and ex-situ experiments are 307 s and 280 s, respectively, showing a good agreement and also slightly lower characteristic time for the fit on the ex-situ data.

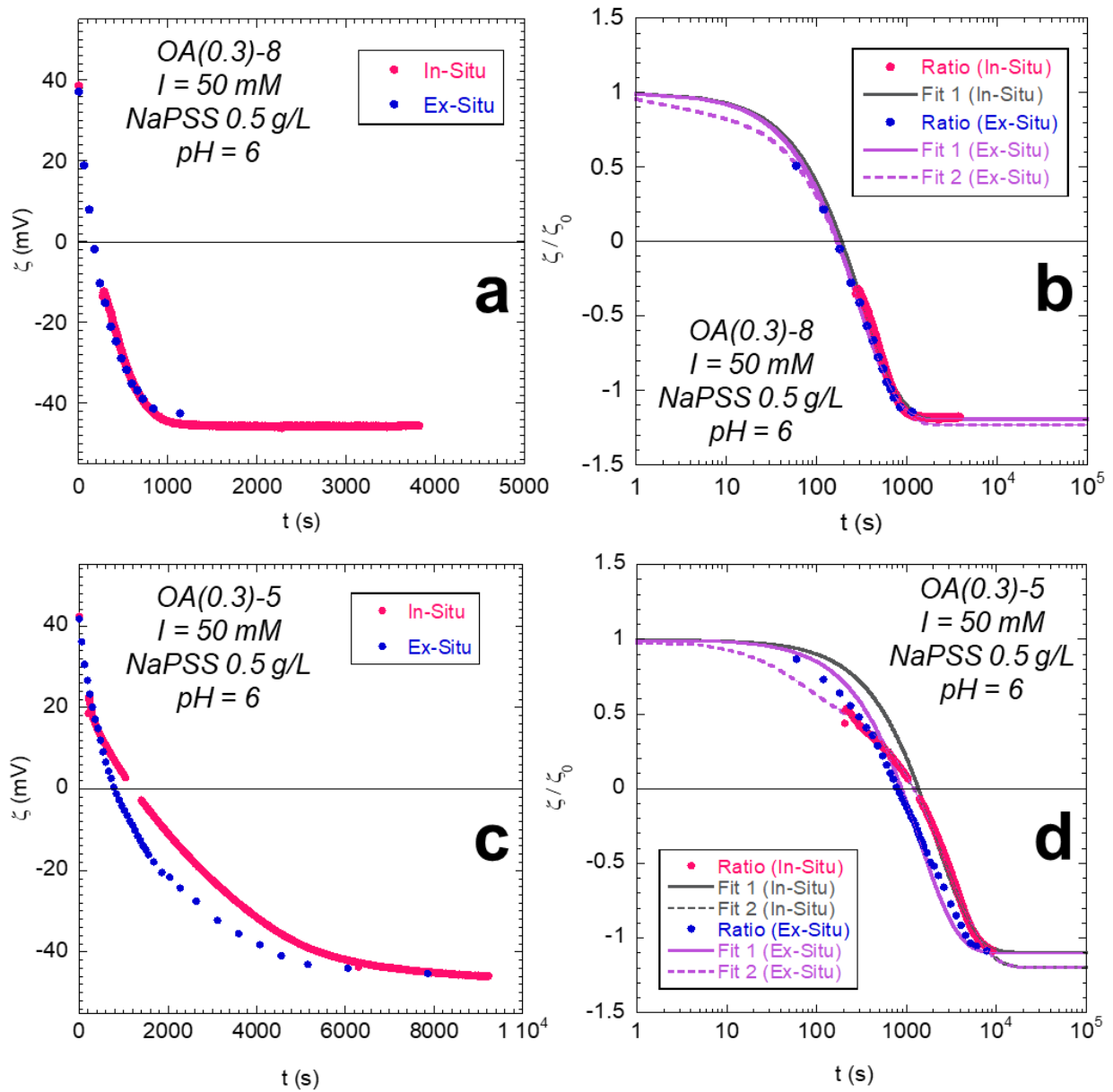


**Figure 3-12** In-situ and ex-situ  $\zeta$ - $t$  data of the **a)** OA(0.3)-8 (20 microns thick) and **b)** the corresponding ratio and fits, **c)** OA(0.3)-5 (49 microns thick) and **d)** the corresponding ratio and fits.

Table 3-7 Fitting parameters of Figure 3-12 curves.

Membrane code	Measurement	A	B	C	$\tau_1$	$\tau_2$	$\zeta_0$ (mV)	$\zeta_{final}$ (mV)
<b>Figure 3-12b (NaPSS 0.5 g/L, I = 50 mM)</b>								
<b>SA(0.3)-8</b>	In-Situ	2.2	0	-1.2	307	-	38.6	-45.6
	Ex-Situ	2.2	0	-1.2	281	-	37.1	-42.5
<b>Figure 3-12d (NaPSS 0.5 g/L, I = 50 mM)</b>								
<b>SA(0.3)-5</b>	In-Situ	1.81	0.38	-1.2	2915	60	42.3	-46
	Ex-Situ	1.59	0.55	-1.2	2121	362	41.7	-45.3

However, for the case of 49  $\mu\text{m}$  OA AAO membrane we can see that, even though the  $\zeta$ -potential approaches the same plateau value for in situ and ex situ measurements, the curves don't superimpose. Presenting a clear reasoning for this observation is challenging. Why the change of surface charge accelerates without hydraulic pressure gradient? One hypothesis is that in such a system that we have charges hydrophilic surface inside the AAO nanochannels, such a pressure gradient does not lead to a convection flow accelerating the movement of the PSS macromolecules. But it can lead to increment of the movement of water molecules inside the nanochannel which opposes the diffusion of the macromolecules and their relaxation on the nanochannels surface. But, for the thinner membrane this phenomenon opposing the diffusion of the PSS macromolecules through nanochannels are less dominant. This can be due to the different geometries and aspect ratios. As we can see, for the membranes of 20  $\mu\text{m}$  thickness, there is no need for the second exponential term for fitting the  $\zeta$ -t data. It means that in the case of thinner membranes, the single exponential equation can fit on the experimental data even on the beginning part of the experiments where the system is further from the equilibrium while for the thicker membranes the single exponential does not fit on the data. Besides, for the 49  $\mu\text{m}$  the characteristic times of the in-situ and ex-situ experiments have considerable differences.

The in-situ and ex-situ experiments along together show that the main phenomenon for the transfer and adsorption of the PSS macromolecules inside the AAO charged nanochannels is the diffusion. We hypothesized the physical phenomena that can play a role in this diffusion and adsorption process and make the quality and the rate of the process different from the situation in which there is no pressure gradient applied. On the other hand, there are two aspects to focus on, in order to affirm the hypothesis that higher aspect ratio leads to phenomena that are not favorable to diffusion and adsorption process in the presence of pressure pulses. And we accordingly, the equation with a single exponential term cannot predict the  $\zeta$ -potential change with time especially in the beginning of the process where the system is further from the equilibrium. But, in Figure 3-12d we can see that the experimental data points are closer to Fit1 compared to Fit2. This can deny our hypothesis regarding the thicker membranes with higher aspect ratio of the nanochannels which stated that the model with two exponential terms can be fitted on the  $\zeta$ -t data of such membranes. We may conclude that the behavior of the system in terms of  $\zeta$ -t curves can be modeled by exponential equations. But, this equation may contain additional terms in order to be able to predict the experimental data. In the models that we currently use, we only use the characteristic time and also the final value for the comparison between the different experiments. But, the functionality of this characteristic time of different variables is still unclear to us. In Figure 3 in the Appendix we have presented two interpretations of the in-situ  $\zeta$ -t data of the oxalic acid membranes that were presented in Figure 3-4 e. The linear trend of the graph in which the  $\zeta$ -potential is plotted versus square root of time normalized by the surface of the nanochannels, makes us closer to concluding that the transport of the PSS macromolecules inside the AAO nanochannels is mainly governed by diffusion mechanism.

### **3.7 Strength of the interactions between the NaPSS macromolecules and the AAO nanochannel surface.**

In this section, we aim to evaluate the strength of the interactions between the NaPSS macromolecules and the AAO nanochannel surface. For this, we have conducted a complementary step after the in-situ  $\zeta$ -potential measurement. At this step, once the  $\zeta$ -t curve reaches to equilibrium, the NaPSS solution is evacuated from the streaming potential measurement device and is replaced by a KCl solution at the same pH and ionic strength but without NaPSS in order to wash away all the possible weakly bonded chains from the surface (we have named this step in the following as the

"washing step"). In Figures 3-13 to 3-15, we have presented the examples of washing steps at different experimental conditions such as the NaPSS concentration, pH and also the ionic strength.

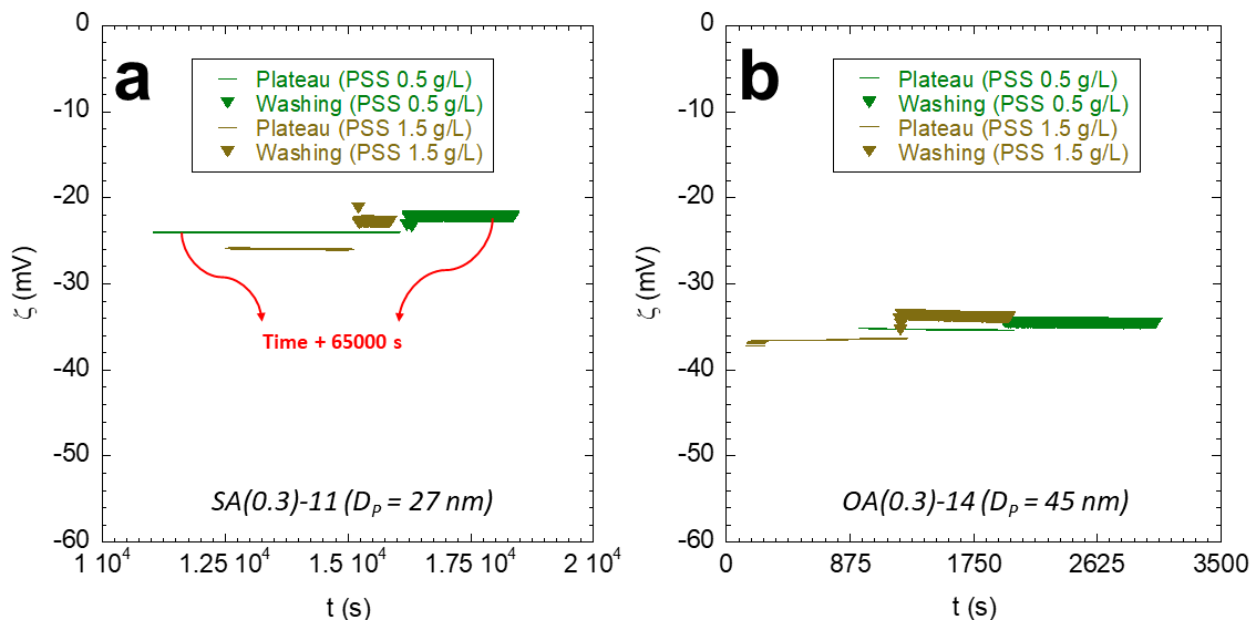


**Figure 3-13** Washing steps  $\zeta$ -potential measurements of **a)** OA(0.3)-11 membrane and **b)** OA(0.3)-14 comparing 10, 50 and 100 mM ionic strengths in 0.5 g/L PSS concentration and pH = 6.

In these figures, the continuous lines correspond to the plateau observed in the  $\zeta$ -potential versus time curves shown previously (see Figure 3-2) and the inverted triangles corresponds to the washing steps. Figure 3-13 shows the corresponding data for 2 NaPSS concentrations (0.5 and 1.5 g/L) at pH=6 and 10 mM KCl. We see that the equilibrium  $\zeta$ -potential plateaus between the adsorption from 0.5 and 1.5 g/L are slightly different. After the washing step, both  $\zeta$ -potential values are now quite similar and still negative (about -22 mV), indicating that the NaPSS chains are still strongly adsorbed to the surface. Similar behavior is also observed for different ionic strengths at a given PE concentration of 0.5 g/L (50 mM and 100 mM, see Figure 3-14).

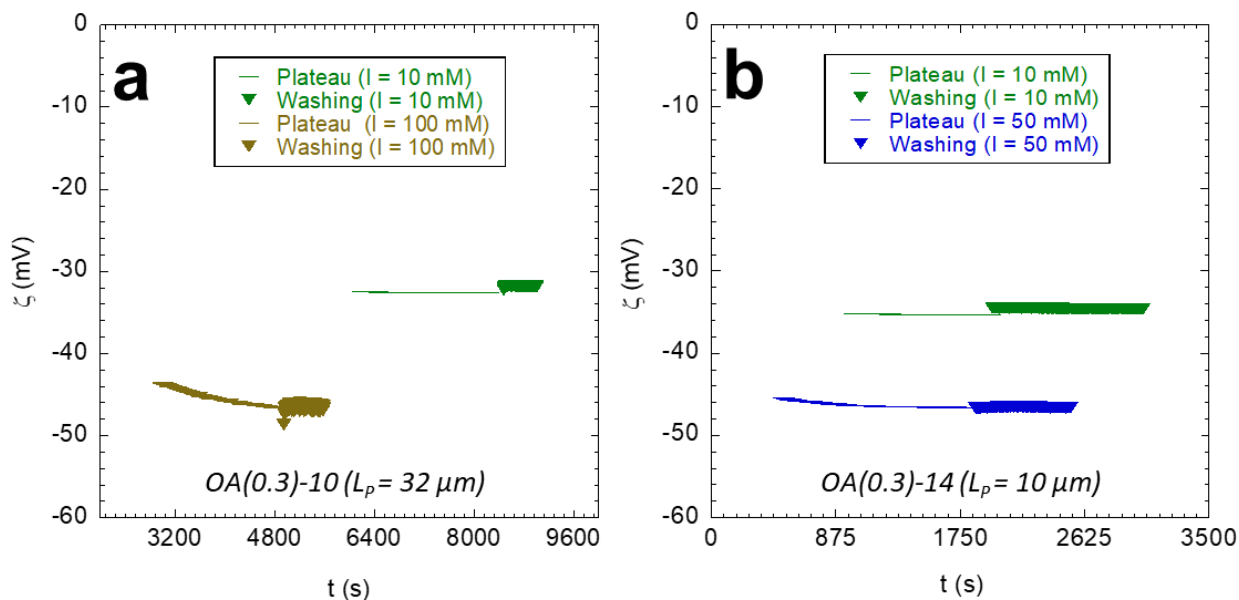


**Figure 3-14** Washing steps  $\zeta$ -potential measurements of **a)** OA(0.3)-11 membrane and **b)** OA(0.3)-14 comparing 10, 50 and 100 mM ionic strengths in 0.5 g/L PSS concentration and pH = 6.

We have compared two pH values of 4 and 6 and also the influence of acetate and HCl for adjusting the pH value at 4. In Figure 3-15 the washing steps are compared at different pH values. Here again, the surface remains always negative after washing. Additionally, in pH = 4 adjusted with acetic acid buffers, we can see that the  $\zeta$ -potential is inclined to increase. This confirms our conclusion about the competition of between the acetate species and the PSS macromolecules for adsorption on the surface.

All these experiments show that the PE macromolecules remain attached to the nanochannels surface. Even by increasing the ionic strength and accordingly screening the charged surface of the AAO nanochannels and reducing the screening length, there is still no change in the  $\zeta$ -potential after the washing step, suggesting some non-electrostatic interactions between the NaPSS macromolecules and the AAO nanochannels surface or an entropic driven adsorption [152], [153].

To summarize, the washing step experiments show three facts. The first is that the PSS macromolecules get strongly attached to the charged surface and this adsorption is not reversible because there are no changes in the  $\zeta$ -potential in washing step. The second tip is that the interactions between the PSS macromolecules and AAO nanochannels surface are effective even in short screening lengths. It gives the hypothesis that non-electrostatic interactions may play a rule in adsorption of PSS on AAO nanochannel surface. The third point is confirmation the weakening of the adsorption of PSS

on the AAO nanochannels surface in case of competition with acetate species for adsorption. In the next section, we will discuss the types of interactions between the PSS macromolecules and AAO nanochannels surface.

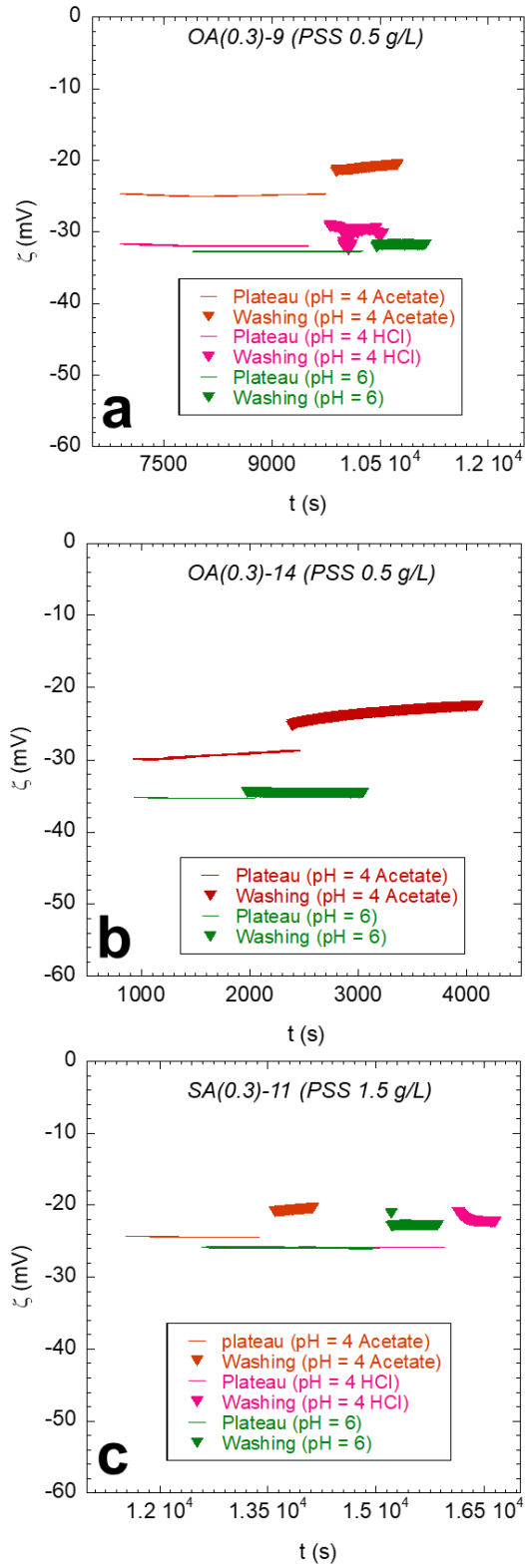


**Figure 3-15** Washing steps  $\zeta$ -potential measurements of **a)** OA(0.3)-9 membrane PSS 0.5 g/L **b)** OA(0.3)-14 membrane PSS 0.5 g/L and **c)** SA(0.3)-11 membrane PSS 1.5 g/L at different pH values.

### **3.8 The nature of the interactions between the NaPSS Macromolecules and AAO nanochannels surface**

At this step, after having discussed the strength of the interactions between the NaPSS macromolecules and the AAO nanochannels surface qualitatively at different conditions, it is aimed to examine the type of these interactions. As mentioned in the previous section, the NaPSS and nanochannels surface interact even in high ionic strength and consequently low screening lengths. Thus, this question must be answered: do the macromolecules and the nanochannels surface interact non-electrostatically also? For this reason, we have designed two different experimental sequences called Approach 1 and Approach 2 and described previously in section 3.3. The description of both approaches is recalled below:

#### **Description of approach 1:**

- 1) SP measurement in KCl solution at pH  $\sim 4$ ,
- 2) SP measurement in KCl solution with pH  $\sim 9$ ,
- 3) repeating step 1,
- 4) repeating step 2,
- 5) SP measurement in a NaPSS solution with the same ionic strength as the preceding steps at pH $\sim 9$  (pH > I.E.P of AAO, the AAO is thus negatively charged).
- 6) SP measurement in a solution with the same ionic strength and pH as step 5 but without PE molecules,
- 7) SP measurement in a solution with the same ionic strength as step 6 but with pH  $\sim 4$ .

#### **Description of approach 2:**

- 1) SP measurement in KCl/water solution with pH  $\sim 6$ ,
- 2) SP measurement in a NaPSS solution with the same pH and ionic strength as step 1,
- 3) repeating step 1,

- 4) SP measurement in KCl/water solution with pH  $\sim$  4,
- 5) SP measurement in KCl/water solution with pH  $\sim$  9,
- 6) repeating step 4.

We have performed the Approach 1 in two different KCl concentrations (10 and 100 mM) on OA AAO membrane OA(0.3)-12. The data are shown in Figure 3-16. The numbers correspond to the different steps of the approach 1.

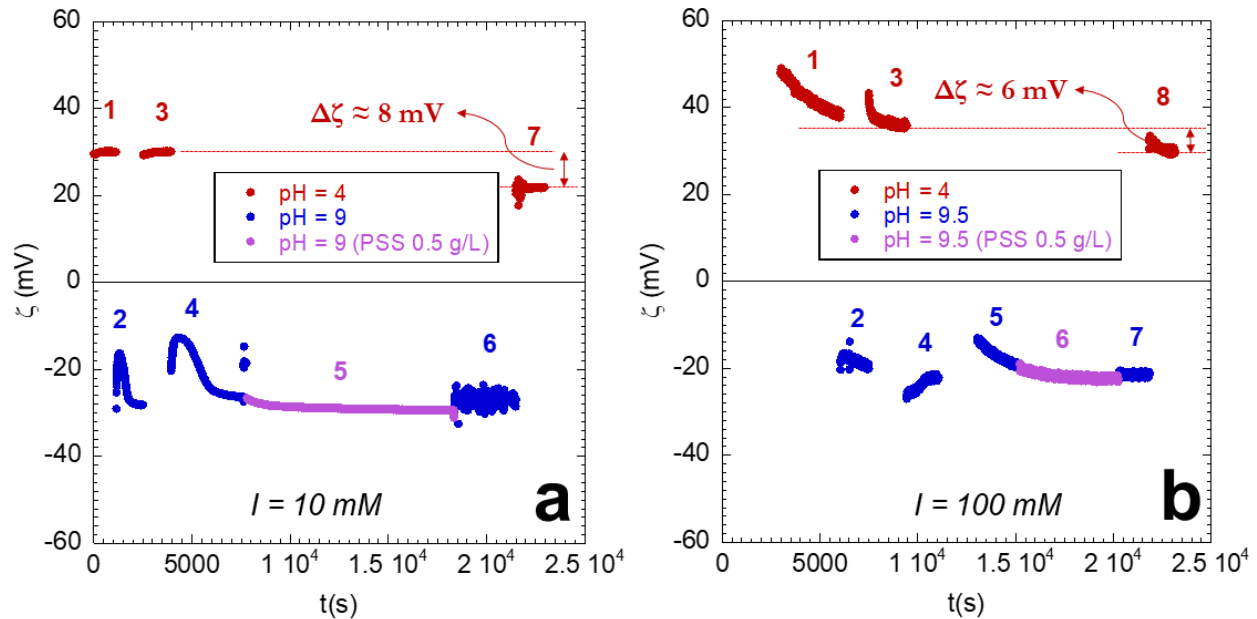


**Figure 3-16**  $\zeta$ -potential measurements by reciprocal changing the pH and contacting the membrane with the AAO in a pH higher than the IEP for the membrane OA(0.3)-12 at KCl concentration of **a)** 10 mM and **b)** 100 mM.

The steps 1-4 correspond to an alternance of acidic and basic solutions to insure the reproducibility in the switching of the AAO charge: positive at low pH and negative at high pH. In step 5 (step 6 in Figure 3-16b), the AAO membrane is then in contact with NaPSS solution at a pH higher than the IEP, for which the AAO nanochannel surface is negatively charged. The measured  $\zeta$ -potential is negative but we cannot tell if the PE is adsorbed or not. The contact with the NaPSS solution is followed by a washing step in which the  $\zeta$ -potential is measured in a solution with pH = 9 (9.5 for Figure 3-16b) but without PSS. Finally, in the last step, the AAO is immersed in an acidic solution (pH = 4) and the  $\zeta$ -potential becomes positive, as in the initial step. The slight difference can

be due to some chemical changes on the nanochannels surface because of a long immersion in basic solution. The important point is that the AAO is positive at the end of this sequence, indicating that the PE doesn't adsorb in pH=9 or the adsorption is weak and the PE chains are easily washed away. These results confirm the electrostatic interactions between the NaPSS macromolecules and the AAO nanochannels.

For confirming this assertion, we move to the second sequence (Approach 2 of section 3.3) depicted in Figure 3-17.

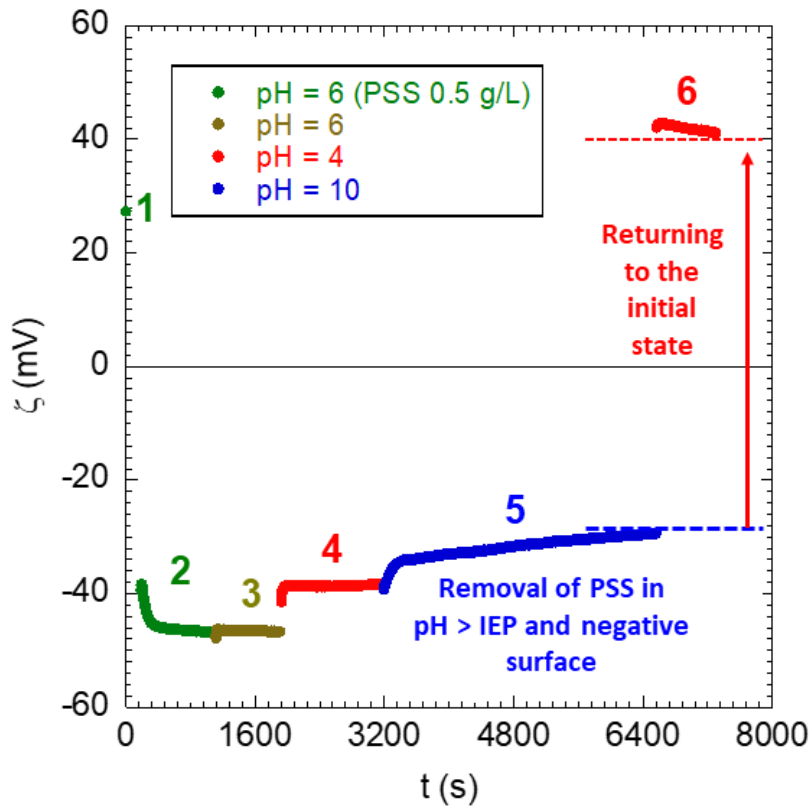


**Figure 3-17**  $\zeta$ -potential measurement sequence (approach 2) in of membrane OA(0.3)-14 at a KCl concentration of 50 mM.

At first the AAO surface is positive and the NaPSS chains adsorb reversing the surface charge to a negative value (light green points) and it remains negative after washing in pH = 6 (dark green) and pH = 4 (red). Then the AAO is immersed in pH = 10 solution for which the bare AAO surface is negative. At this step we cannot tell if the PE is still adsorbed or not. Finally, a last step is performed in pH = 4 and the  $\zeta$ -potential goes back to a positive value, indicating that the NaPSS chains have been

washed away from the surface. It shows the desorption of NaPSS macromolecules from the AAO nanochannels surface in a pH higher than IEP where the surface has a net negative charge and confirms that the electrostatic interactions are important for PE adsorption.

### 3.9 Coverage of the nanochannels with small monomers

However, even though electrostatic plays an important role, our results at high salt concentration also suggest non-electrostatic interaction or possible entropy driven adsorption. Another point that also needs to be elucidated is the origin of the charge overcompensation when PE chains adsorb. To gain more understanding on these different aspects we have done  $\zeta$ -potential measurement experiments using the NaPSS monomer (sodium styrene sulfonate) in order to study its adsorption behavior. Figure 3-18 shows the  $\zeta$ -potential evolution with time of a monomer solution at different concentration (0.5 g/L or 20.8 g/L) with different KCl concentration (50 mM and 1 mM). Figure 3-18a shows the data for a monomer concentration similar to the PE one used previously (0.5 g/L) in 50 mM KCl for comparison between monomer and PE. With the monomer no change was observed in the  $\zeta$ -potential, the AAO surface remains positive with a value similar to the bare AAO (45 mV). Thus, there is no monomer adsorption. Then, Sukhishvili et al. [154] observed that it needed more monomers to have similar adsorbed amount of analogue PE. Thus, we increased the monomer concentration up to 20.8 g/L in 50 mM KCl. This concentration was considerably higher than the NaPSS concentration from our previous solutions. But, as we can see from Figure 3-18b, although the  $\zeta$ -potential of the nanochannels surface is reduced to about 25 mV, it remains positive even if we let the solution in the cell during a long time (up to 75 min). Hence, it was concluded that, if the monomer adsorbs, the amount is not enough to overcompensate or even to compensate the surface charge of the nanochannels. Our reasoning was that the monomers should compete for adsorption with small monovalent salt ions that are present in the solution. Thus we decreased the KCl concentration to 1 mM in order to reduce the amount of species that can compete with monomers for adsorption. Figure 3-18c shows the corresponding  $\zeta$ -potential versus time curves. There is still no change observed in the sign of the AAO surface charges. At this ionic strength, the obtained magnitude of the  $\zeta$ -potential is challenging according to the fact that we use Helmholtz-Smoluchowski correlation for converting the streaming potential to the  $\zeta$ -potential and in such a low ionic strength this correlation is not valid anymore. Even the sign of the  $\zeta$ -potential shows that the adsorption of the monomers on the AAO nanochannels surface is negligible even in very low ionic strength, low salts for competition for adsorption and also higher screening length. The reason can be due to the fact that although the

monomers interact electrostatically with the charged surface, according to their low mass, they cannot provide the energy required to displace the electrical double layer adjacent to the oxide surface and adsorb. Thus, we can say that for adsorption of the oxide surface, the attraction force is required, but it is not enough. There should be sufficient energy for displacing the EDL which the macromolecules possess but the monomers do not.

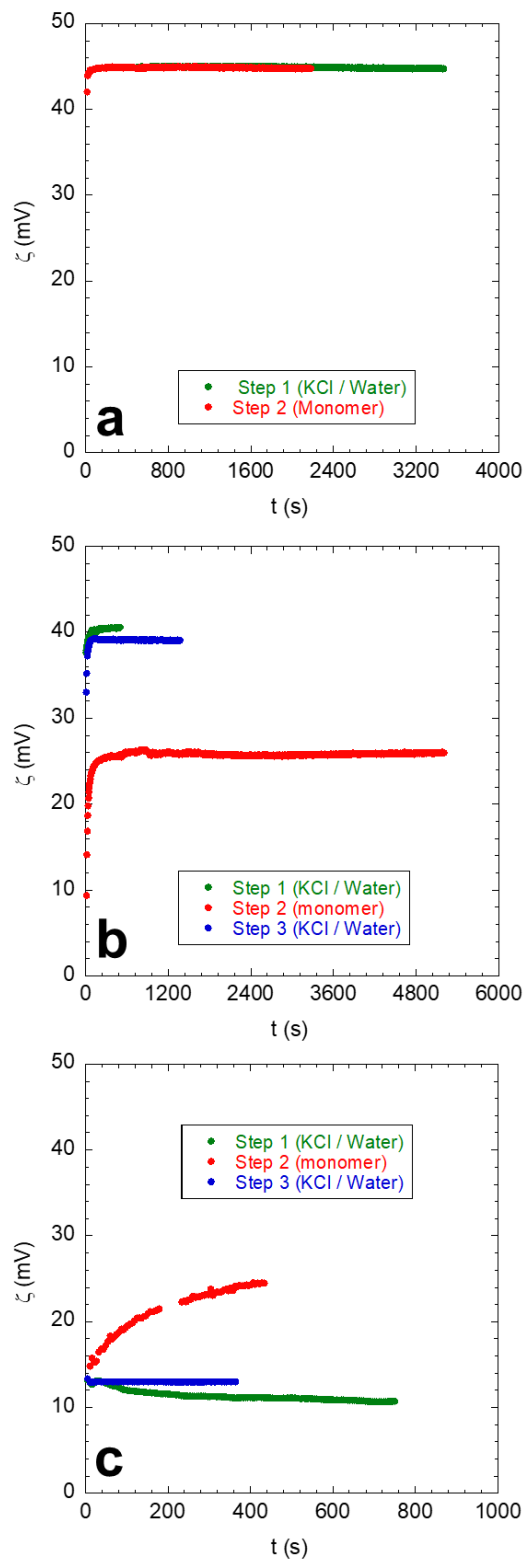


**Figure 3-18** In-situ  $\zeta$ -potential measurement of the membrane OA(0.3)-5 in contact with solution of **a)** 0.5 g/L styrene sulfonate monomer and KCl = 50 mM, **b)** 100 mM (20.8 g/L) styrene sulfonate monomer and KCl = 50 mM, **c)** 100 mM (20.8 g/L) styrene sulfonate monomer and KCl = 1 mM.

### 3.10 Conclusion

In this chapter, we presented a detailed study on the behavior of NaPSS macromolecules inside the AAO nanochannels in terms of diffusion/adsorption rate, strength of interactions and also nature of the interactions. We studied the effect of different variables on the rate of this process. We performed *in situ*  $\zeta$ -potential measurements in order to monitor the change of the AAO internal surface charge due to the adsorption of PSS. We used membranes synthesized in 0.3 M solutions of sulfuric Acid and Oxalic acid with thicknesses ranging from 49 to 10 microns. The pore densities of these membranes range from 1 to  $2.5 \cdot 10^{10}$  per  $\text{cm}^2$  as discussed in details in chapter 1. We changed the variables that were predicted to affect the rate of diffusion/adsorption process. The ionic strength ranged from 1 to 100 mM, the pH values were fixed to 4 or 6 and for maintaining pH at 4 we used either  $\text{CH}_3\text{COOH}/\text{CH}_3\text{COO}^-$  buffer or HCl solution.

It was observed that regardless of the thickness of the membranes ( $L_p$ ), in the same pH, ionic strength and NaPSS concentration the  $\zeta$ -t curves of the membranes synthesized in the same acid type and concentration (possessing the same morphological properties except the thickness) approach approximately the same equilibrium plateau value. By normalizing the  $\zeta$ -potential values with  $\zeta$ -potential of the bare AAO ( $\zeta_0$ ), we showed the charge overcompensation of the AAO nanochannels with NaPSS macromolecules. We can see that the equilibrium values at the plateau of the curves show a similar overcompensation of the nanochannels surface charge. This can be hypothesized that regardless of the thickness of the membranes, the interior surface of their nanochannels are uniformly covered by NaPSS with similar amount of absorbed PSS per unit length. The lower rate for thicker membranes is due to the higher time needed for the coverage of the higher surface.

It was also observed that in  $\text{pH} = 4$ , in case HCl has been used for maintaining the pH, the rate and the equilibrium value for a unique membrane does not change according to the fact that in  $\text{pH} = 4$  the charge density of the AAO nanochannels is same as  $\text{pH} = 6$  according to the  $\text{pH}-\zeta$  diagrams obtained for different AAO membranes in chapter 2. But, in case acetate buffer is used for maintaining the pH, the rate of the process decreases and the final equilibrium  $\zeta$ -potential value increases which shows the competition of the acetate species for adsorption with NaPSS macromolecules and occupation of a part of the charge sites of the surface by these species.

Regarding the effect of ionic strength, it was observed that the rate of the process increases with increasing the ionic strength due to more space available to the macromolecules to diffuse because of

the thinner EDL formed adjacent to the nanochannel surface. The equilibrium value of  $\zeta$ -potential showed to decrease with increasing the ionic strength due to the fact that increasing the ionic strength screens more the electrostatic interactions. Thus, repulsion between the shrunk chains decreases in high ionic strength and more chains can adsorb of the surface and consequently the charge of the surface can be more overcompensated.

Then, by doing *ex-situ*  $\zeta$ -potential measurements we proved that the main mechanism governing the transfer and adsorption of the PSS macromolecules inside the AAO nanochannels is the diffusion and the hydraulic pressure pulses that are imposed to the membrane ends in order to measure the streaming potential does not accelerate the transfer of polyelectrolytes inside the nanochannels.

Finally, it was also shown by appropriate experimental sequences that the interactions between the NaPSS macromolecules and the AAO nanochannels surface are from the electrostatic type as we observed no adsorption of PSS macromolecules on the nanochannels surface in a pH higher than the IEP where the net charge of the surface is negative. Besides, we observed that the PSS macromolecules that were adsorbed on the surface in a pH lower than IEP, were desorbed when the pH was shifted to more than IEP. At last we reasoned that the lack of adsorption of styrene sulfonate on the AAO nanochannels surface is due to the lack of sufficient energy from the monomer to displace the electrical double layer and adsorb on the surface.

## General conclusions

In this thesis, we aimed to study the morphology and surface charge properties of anodic aluminum oxide (AAO) membranes completely in order to use it as a charged nanoporous medium for studying the behavior of polyelectrolytes inside charged nanochannels. In order to have AAO membranes with different pore diameters and accordingly different curvatures for studying the polyelectrolyte macromolecules inside, we went through a complete experimental study on synthesizing the AAO through anodizing the aluminum in different acid types. Since we wanted to have through-hole AAO membranes in order to be able to characterize the internal surface of the nanochannels and also the behavior of the polyelectrolytes inside the nanochannels by means of transverse streaming potential measurement, we chose a wet etching process for detaching the AAO from the aluminum substrate surface. We characterized the membranes from cross-section along with the third layer that is formed during the wet-etching process with EDX analysis which evidenced the difficulties of detaching the sulfuric and selenic acid synthesized AAO from the aluminum surface. We realized that the sulfur contamination of the layer formed in the third anodization plays the key role in success of the detachment. Through these characterizations, we confirmed the incorporation of the anions species of the anodization acid inside the structure of the AAO. Thanks to this systematic experimental study, we succeeded to synthesize through-hole AAO membranes from three different acid types namely oxalic, sulfuric and selenic through two step anodization and wet etching. Consequently, we obtained membranes with different pore diameters and pore densities. We also characterized the bulk structure of the membranes by FTIR spectroscopy, from which the refractive index of the material can be determined. Its value depends on the compositions of the AAO membranes which is consistent with conclusions from the EDX analysis. Both characterizations confirmed the incorporation of ions inside the AAO structure, their amount increasing with the acid concentration.

As we synthesized through-hole membranes from different acid solutions, with obtained different pore density, pore geometries, and contamination levels, we speculated different surface charge properties from these different membranes. We studied the surface charge properties of the through-hole membranes synthesized in different acid types and acid concentrations by electrokinetic experiments on different surfaces of the AAO membranes. Transverse streaming potential was used for studying the internal surface of the membranes nanochannels, tangential streaming current measurement for the top and bottom outer surface, and electrophoretic mobility was used for studying the surface

charge of the particles that were made of smashing the AAO membranes samples. For all of the mentioned surfaces using the mentioned techniques, we determined the  $\zeta$ -potential of the surface on a large range of pH values in order to find the isoelectric point (I.E.P) of these surfaces. We realized that the contamination with different acid anions types and the extent of contamination in the ranges that we studied, does not affect the surface charge properties of the different membranes as we observed the same IEP for our studied membranes on their different surfaces which was around 7 for the outer surfaces of the membranes, 9 for the nanochannels surfaces and around 6 for the smashed particles. The differences between the internal surface of the nanochannels and the external surfaces were asserted to be due to the differences in the roughness of these surfaces since the roughness of the inner surface of the nanochannels are reported to be much lower than what we measured by atomic force microscope (AFM) for the outer surfaces.

By studying the surface charge properties of our AAO membranes completely, our AAO membrane were used as a charged nanoporous medium in which we studied the behavior of the sodium polystyrene sulfonate as a model strong polyanion. By using transverse streaming potential measurement, we studied the adsorption rate of PSS inside the AAO nanochannels by monitoring the change of the surface charge of the AAO nanochannels by determining  $\zeta$ -potential versus time. We discussed the rate of the process by mathematical analyzing the  $\zeta$ -t curves and comparing the characteristic times of these curves determined from exponential fits. By varying a set of variables that we expected to affect the rate of reaching to the final equilibrium state  $\zeta$ -potential, we realized that the rate of the process increases with increasing the PSS concentration in the solution, increasing the ionic strength up to a certain level (we observed an increase in changing the I from 50 to 100 mM). This was in line with the concepts presented by researchers that the process of adsorption of polyelectrolytes on the charged surfaces is a balance between attraction and repulsion forces acting on the macromolecules and between the macromolecules. Thus, above a specific ionic strength, the repulsions between the chains may be higher than the screened attraction and this is an obstacle against attraction of the PSS on the AAO nanochannel surface. The rate of the adsorption process showed to be similar in similar surface charge density disregarding the pH (we conclude similar charge density for the internal surface of the nanochannels between pH values 4 and 6 from our pH- $\zeta$  curves in chapter). Although the concentration of acetate was low, it showed to compete with the PSS macromolecules for adsorption. Thus, buffer should be avoided to set the pH in the polyelectrolyte solutions.

By doing ex-situ experiments with polyelectrolytes solution, we concluded that the process of diffusion and adsorption of PSS inside AAO nanochannels is mainly governed by diffusion rather than convective flow. The interactions between the PSS and the AAO nanochannels surfaces were observed to have pure electrostatic nature. We did not observe other sorts of interactions between the AAO nanochannels surface and the PSS macromolecules at least in the conditions that we worked in.

Thus, in this work we revealed the trend of the change of the kinetics of the adsorption of PSS on the nanochannels surface of AAO with different variables and also we showed the type of the interactions. There are some suggestions for continuing this research:

- More control on the geometry of the AAO membranes. Finding a way for accelerating dissolution of the third layer will donate membranes with higher curvature (smaller pore size) which can widen this systematic study. For this to be done, the main question that should be sought is: how to accelerate the diffusion of phosphochromic acid species through AAO nanochannels.
- Studying the behavior of positive strong polyelectrolytes inside the nanochannels in a pH higher than IEP of the AAO can reveal worthy informations about the behavior of charged macromolecules inside oppositely charged nanochannels.
- Finding a way for accurate insights to the features of the solution filling the nanochannels can give useful information about the features and conditions of the solution inside filling the nanochannels. More clearly: Measuring the exact concentration of the polyelectrolyte macromolecules inside the nanochannels. The exact conductivity of the solution will be also useful for knowing the surface conductivity inside the nanochannels before and after polyelectrolytes adsorption.
- Kinetics study can be continued by varying the variables in a wider range. It worth changing the ionic strength up to a point that the adsorption of the polyelectrolyte on the surface is vanished. This shows the point in which the electrostatic attractions and the repulsion neutralize each other.
- One of the biggest questions that is worth being answered in this field of research is the amount of the polyelectrolyte that is adsorbed on the AAO nanochannel surface. It is not clarified if the surface of the nanochannel is uniformly covered with polyelectrolyte in the final state ( $\zeta_{\text{final}}$ ). It may be feasible by doing the experiments in the length ranges comparable to the pores diameters and making efforts to widen the length.

- In case the hydrodynamic thickness of the adsorbed layer is accurately measured, it is possible to determine the  $\zeta$ -potential with an equation like Helmholtz-Smoluchowski in which there are assumptions that can give values different from the reality. It will be possible to determine the  $\zeta$ -potential on the polyelectrolyte/solution interface accurately and by comparison with the bare alumina membrane, there will be an insight to the potential distribution inside the soft layer adsorbed on the surface (Donnan potential profile).

# Appendix

**Table Appendix-1** Anodization conditions of the membranes synthesized in oxalic acid 0.3M solutions. For all of these membranes the anodization voltage in the second and third anodization is 40V

Membrane Code name	Second Anodization					Third Anodization					Detached
	Solution	<j> mA/cm <sup>2</sup>	T (°C)	t(min)	Thickness (μm)	Solution	<j> mA/cm <sup>2</sup>	T (°C)	t(min)	Thickness (μm)	
<b>OA(0.3)-1</b>	OA(0.3M)-1	5.03	18	108	14.8	SA(13M)-1	4.08	~ 0	33	6.78	YES
<b>OA(0.3)-2</b>	OA(0.3M)-1	4.95	18	184	23.8	SA(13M)-1	3.34	~ 0	41	7	YES
<b>OA(0.3)-3</b>	OA(0.3M)-1	4.81	18	308	39.5	SA(13M)-1	3.64	~ 0	40	6.35	YES
<b>OA(0.3)-4</b>	OA(0.3M)-1	4.59	18	468	59.5	SA(13M)-1	3.17	~ 0	41	6.25	YES
<b>OA(0.3)-5</b>	OA(0.3M)-2	4.78	18	389	49.1	SA(13M)-1	20.42		8	-	YES
<b>OA(0.3)-6</b>	OA(0.3M)-2	4.38	18	388	45.9	SA(13M)-1	15.53	0 to 8.4	9	-	YES
<b>OA(0.3)-7</b>	OA(0.3M)-2	4.1	18	272	29.9	SA(13M)-1	24.23	0 to 9.5	5.5	-	YES
<b>OA(0.3)-8</b>	OA(0.3M)-2	3.92	18	180	19.4	SA(13M)-1	27.75	0 to 8	4	-	YES
<b>OA(0.3)-9</b>	OA(0.3M)-1	3.78	18	344	34.1	SA(13M)-1	18.11		5	-	YES
<b>OA(0.3)-10</b>	OA(0.3M)-2	3.31	18	360	32	SA(13M)-1	23.97		5	-	YES
<b>OA(0.3)-11</b>	OA(0.3M)-2	3.21	18	245	20	SA(13M)-1	26.82	-1 to 6.8	3	-	YES
<b>OA(0.3)-12</b>	OA(0.3M)-2	2.79	18	245	18.8	SA(13M)-1	35.73	-1 to 11	2	-	YES
<b>OA(0.3)-13</b>	OA(0.3M)-3	4.53	18	78	-	SA(13M)-1	Saturated	-2.5 to 0	1	-	NO
<b>OA(0.3)-14</b>	OA(0.3M)-3	5.92	18	60	9.9	SA(13M)-2	24.52	0 to 13.6	5	-	YES
<b>OA(0.3)-15</b>	OA(0.3M)-3	4.65	18	154	20.5	SA(13M)-2	25.23	-2.2 to 10.3	6	-	YES
<b>OA(0.3)-16</b>	OA(0.3M)-3	4.66	18	154	19.5	SA(13M)-2	46.65	-2 to 11	6	-	YES

**Table Appendix-2** Anodization conditions of the membranes synthesized in sulfuric acid 0.3M solution. For all of these membranes the anodization voltage in the second anodization is 25V.

Membrane		Second Anodization				Third Anodization						Detached
Code	Solution	<j>	T (°C)	t(min)	Thickness	Solution	U (V)	<j>	T (°C)	t(min)	Thickness	
name		mA/cm <sup>2</sup>			(μm)			mA/cm <sup>2</sup>			(μm)	
<b>SA(0.3)-1</b>	SA(0.3M)-N	6.42	18	132	15.2	SA(13M)-1	25	1.18	~ 0	119	4.64	YES
<b>SA(0.3)-2</b>	SA(0.3M)-N	5.24	18	234	25.2	SA(13M)-1	25	1.67	~ 0	119	4.93	YES
<b>SA(0.3)-3</b>	SA(0.3M)-N	5.10	18	390	46.2	SA(13M)-1	25	2.36	~ 0	100	4.23	NO
<b>SA(0.3)-4</b>	SA(0.3M)-N	5.56	18	564	64.2	SA(13M)-1	25	2.16	~ 0	100	2.95	NO
<b>SA(0.3)-5</b>	SA(0.3M)-1	8.29	18	235	41.5	SA(13M)-1	25	1.54	~ 0	40	2.13	YES
<b>SA(0.3)-6</b>	SA(0.3M)-1	7.85	18	245	44.8	SA(13M)-1	40	4.06	0 to 2.3	20	4.46	NO
<b>SA(0.3)-7</b>	SA(0.3M)-1	7.44	18	227	43.3	SA(13M)-1	25	2.25	~ 0	40	3.68	YES
<b>SA(0.3)-8</b>	SA(0.3M)-1	5.81	18	259	40.3	SA(13M)-1	45	7.59	0 to 4.2	8	3.14	NO
<b>SA(0.3)-9</b>	SA(0.3M)-1	4.7	18	360	46.3	SA(13M)-1	25	4.35	0 to 1.1	35	-	YES
<b>SA(0.3)-10</b>	SA(0.3M)-1	4	18	364	38.3	SA(13M)-1	25	4.38	0 to 1.2	35	-	YES
<b>SA(0.3)-11</b>	SA(0.3M)-1	3.47	18	260	24.5	SA(13M)-1	25	5.45	0 to 1.6	25	-	YES
<b>SA(0.3)-12</b>	SA(0.3M)-1	3.07	18	255	21	SA(13M)-1	25	6.11	-	19	-	YES

**Table Appendix-3** Anodization conditions of the membranes synthesized in selenic acid 0.3M solution. For all of these membranes the anodization voltage in the second and third anodization is 45V.

Membrane Code name	Second Anodization					Third Anodization					Detached
	Solution	<j> mA/cm <sup>2</sup>	T (°C)	t(min)	Thickness (μm)	Solution	<j> mA/cm <sup>2</sup>	T (°C)	t(min)	Thickness (μm)	
<b>SeA(0.3)-1</b>	SeA(0.3M)-1	1.52	9	243	9.5	SA(13M)-1	Saturated	-1 to 17	3.5	-	YES
<b>SeA(0.3)-2</b>	SeA(0.3M)-1	1.48	9	540	-	SA(13M)-1	10.3	-1 to 7.2	20	-	NO
<b>SeA(0.3)-3</b>	SeA(0.3M)-1	0.9	0	439	8	SA(13M)-1	Saturated	-1 to 17	2	10.6	NO
<b>SeA(0.3)-4</b>	SeA(0.3M)-1	0.84	0	758	11.1	SA(13M)-1	Saturated		3.5	8.8	NO
<b>SeA(0.3)-5</b>	SeA(0.3M)-1	0.93	0 to 2.5	1238	23.4	SA(13M)-1	20.93	0 to 9	13	11.4	YES*
<b>SeA(0.3)-6</b>	SeA(0.3M)-1	1.14	0 to 1.7	1312	20.2	SA(13M)-1	20.19	0 to 3.2	3	2.65	YES

**Table Appendix-4** Anodization conditions of the membranes synthesized in oxalic acid solutions of 0.05 and 0.8M. For all of these membranes the anodization voltage in the second and third anodization is 40V

Membrane Code name	Second Anodization					Third Anodization					Detached
	Solution	<j> mA/cm <sup>2</sup>	T (°C)	t(min)	Thickness (μm)	Solution	<j> mA/cm <sup>2</sup>	T (°C)	t(min)	Thickness (μm)	
<b>OA(0.05)-1</b>	OA(0.05M)-1	1.79	18	400	16	SA(13M)-1	Saturated	0 to 6.6	1.5	-	YES
<b>OA(0.8)-1</b>	OA(0.8M)-1	7.32	18	110	23.4	SA(13M)-1	Saturated	0 to 7	1.5	-	YES
<b>OA(0.8)-2</b>	OA(0.8M)-1	7.17	18	120	-	SA(13M)-2	50.21	-3.2 to -0.6	4	-	YES

**Table Appendix-5** Morphological properties of the membranes synthesized in oxalic acid 0.3M solution.

<b>Code name</b>	<b>Side</b>	<b>Average pores diameter (nm)</b>	<b>Pores density (cm<sup>-2</sup>)</b>	<b>Porosity (%)</b>
<b>OA(0.3)-1</b>	Top	56 ± 3	1.0 × 10 <sup>10</sup>	25
	Bottom	49 ± 3	9.38 × 10 <sup>9</sup>	18
<b>OA(0.3)-2</b>	Top	52 ± 4	1.05 × 10 <sup>10</sup>	22
	Bottom	45 ± 2	1.02 × 10 <sup>10</sup>	16
<b>OA(0.3)-3</b>	Top	58 ± 6	1.07 × 10 <sup>10</sup>	29
	Bottom	46 ± 2	9.87 × 10 <sup>9</sup>	16
<b>OA(0.3)-4</b>	Top	62 ± 2	9.7 × 10 <sup>9</sup>	30
	Bottom	-	-	-
<b>OA(0.3)-5</b>	Top	59 ± 5	1.08 × 10 <sup>10</sup>	30
	Bottom	41 ± 2	1.19 × 10 <sup>10</sup>	15
<b>OA(0.3)-6</b>	Top	61 ± 7	1.08 × 10 <sup>10</sup>	33
	Bottom	43 ± 3	1.14 × 10 <sup>10</sup>	16
<b>OA(0.3)-7</b>	Top	54 ± 4	1.06 × 10 <sup>10</sup>	24
	Bottom	42 ± 3	1.03 × 10 <sup>10</sup>	14
<b>OA(0.3)-8</b>	Top	46 ± 3	1.08 × 10 <sup>10</sup>	17
	Bottom	44 ± 3	1.10 × 10 <sup>10</sup>	17
<b>OA(0.3)-9</b>	Top	47 ± 5	1.10 × 10 <sup>10</sup>	22
	Bottom	46 ± 7	1.08 × 10 <sup>10</sup>	15
<b>OA(0.3)-10</b>	Top	52 ± 2	9.76 × 10 <sup>9</sup>	20
	Bottom	43 ± 2	9.48 × 10 <sup>9</sup>	13
<b>OA(0.3)-11</b>	Top	43 ± 3	1.02 × 10 <sup>10</sup>	14
	Bottom	40 ± 6	9.74 × 10 <sup>9</sup>	11
<b>OA(0.3)-12</b>	Top	48 ± 3	1.02 × 10 <sup>10</sup>	18
	Bottom	42 ± 2	1.00 × 10 <sup>10</sup>	15
<b>OA(0.3)-14</b>	Top	48 ± 3	1.02 × 10 <sup>10</sup>	19
	Bottom	45 ± 2	9.91 × 10 <sup>9</sup>	15
<b>OA(0.3)-15</b>	Top	47 ± 4	1.08 × 10 <sup>10</sup>	19
	Bottom	45 ± 3	1.03 × 10 <sup>10</sup>	16
<b>OA(0.3)-16</b>	Top	53 ± 6	1.18 × 10 <sup>10</sup>	26
	Bottom	46 ± 4	1.08 × 10 <sup>10</sup>	18

**Table Appendix-6** Morphological properties of the membranes synthesized in sulfuric acid 0.3M solution.

<b>Code name</b>	<b>Side</b>	<b>Average pores diameter (nm)</b>	<b>Pores density (cm<sup>-2</sup>)</b>	<b>Porosity (%)</b>
<b>SA(0.3)-1</b>	Top	42 ± 4	2.46 × 10 <sup>10</sup>	24
	Bottom	38 ± 2	2.41 × 10 <sup>10</sup>	27
<b>SA(0.3)-2</b>	Top	46 ± 4	2.43 × 10 <sup>10</sup>	41
	Bottom	34 ± 2	2.58 × 10 <sup>10</sup>	23
<b>SA(0.3)-5</b>	Top	45 ± 2	2.43 × 10 <sup>10</sup>	33
	Bottom	32 ± 1	2.69 × 10 <sup>10</sup>	19
<b>SA(0.3)-6</b>	Top	43 ± 3	2.67 × 10 <sup>10</sup>	33
	Bottom	27 ± 2	2.4 × 10 <sup>10</sup>	13
<b>SA(0.3)-7</b>	Top	40 ± 2	2.63 × 10 <sup>10</sup>	29
	Bottom	41 ± 2	2.7 × 10 <sup>10</sup>	17
<b>SA(0.3)-8</b>	Top	26 ± 5	2.65 × 10 <sup>10</sup>	33
	Bottom	31 ± 1	2.03 × 10 <sup>10</sup>	12
<b>SA(0.3)-9</b>	Top	47 ± 3	2.56 × 10 <sup>10</sup>	48
	Bottom	27 ± 4	2.55 × 10 <sup>10</sup>	13
<b>SA(0.3)-10</b>	Top	48 ± 3	2.50 × 10 <sup>10</sup>	45
	Bottom	31 ± 2	2.44 × 10 <sup>10</sup>	18
<b>SA(0.3)-11</b>	Top	39 ± 2	2.55 × 10 <sup>10</sup>	29
	Bottom	27 ± 4	2.47 × 10 <sup>10</sup>	14
<b>SA(0.3)-12</b>	Top	39 ± 4	2.59 × 10 <sup>10</sup>	31
	Bottom	30 ± 3	2.54 × 10 <sup>10</sup>	22

**Table Appendix-7** Morphological properties of the membranes synthesized in other oxalic acid concentrations

<b>Code name</b>	<b>Side</b>	<b>Average pores diameter (nm)</b>	<b>Pores density (cm<sup>-2</sup>)</b>	<b>Porosity (%)</b>
<b>OA(0.05)-1</b>	Top	62 ± 8	8.68 × 10 <sup>9</sup>	26
	Bottom	53 ± 8	9.88 × 10 <sup>9</sup>	23
<b>OA(0.8)-1</b>	Top	70 ± 7	1.17 × 10 <sup>10</sup>	48
	Bottom	53 ± 3	1.16 × 10 <sup>10</sup>	26
<b>OA(0.8)-2</b>	Top	56 ± 5	1.21 × 10 <sup>10</sup>	31
	Bottom	48 ± 3	1.10 × 10 <sup>10</sup>	21

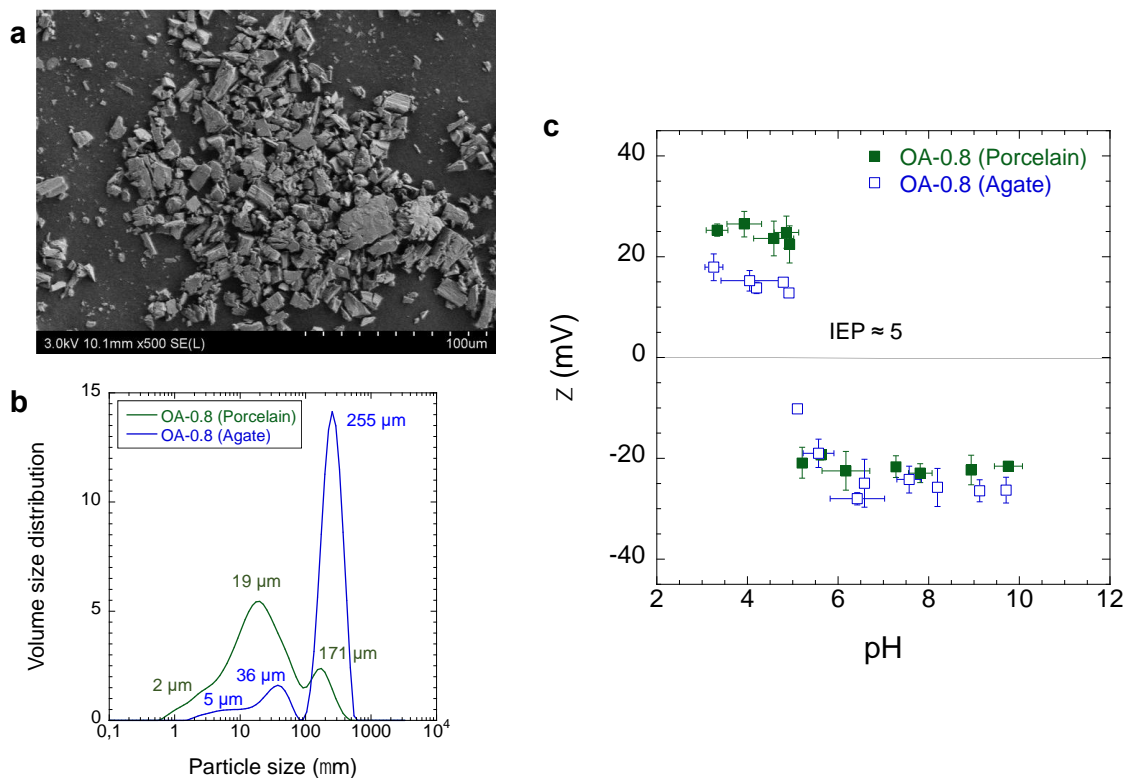


**Figure Appendix 1** (a) SEM images of OA-0.8 AAO membrane manually ground with an Agate mortar and pillar. (b) Volume size distribution as a function of particle diameter obtained by laser granulometry for OA-0.8 AAO ground in porcelain (green line) or Agate (blue line) mortar. The volume size distribution is an average of 5 runs of measurements. (c)  $\zeta$ -potential of OA-0.8 membranes measured by electrophoretic mobility (EM) of the AAO membrane ground in porcelain (full green squares) or Agate (open blue squares) mortar.

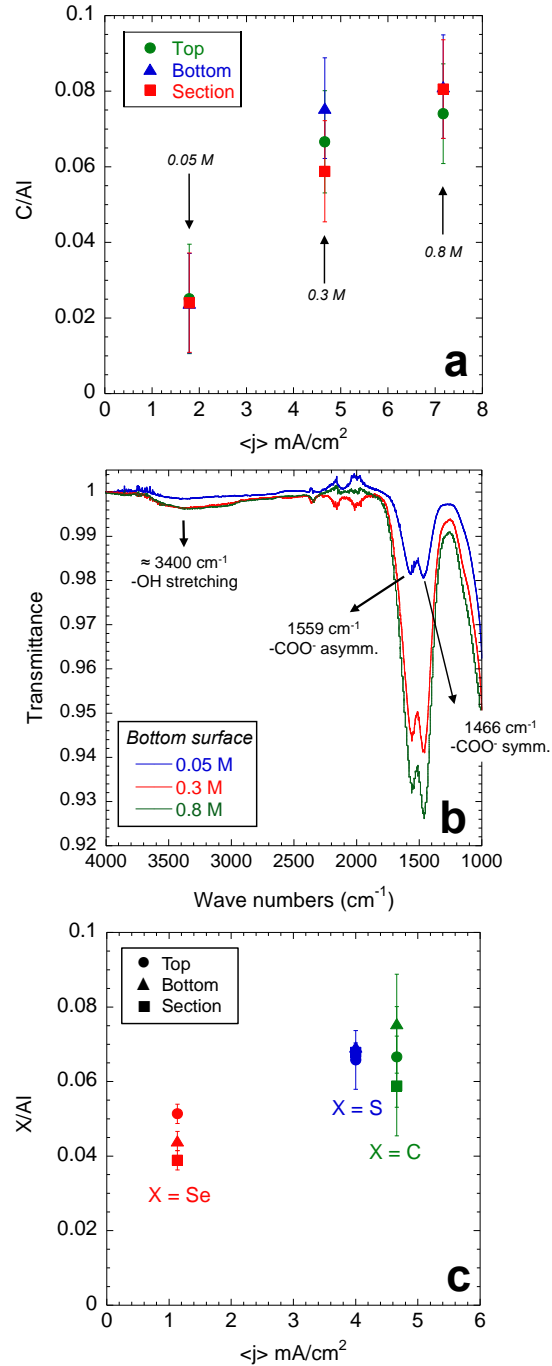


**Figure Appendix 2** **a)** Atomic ratio C / Al obtained from EDS as a function of average anodization current density ( $\langle j \rangle$  in mA/cm<sup>2</sup>) of AAO membranes synthesized with different OA concentrations (0.05 M, 0.3 M and 0.8 M) for top (circle), bottom (triangle) and section (square) surfaces. **b)** Infrared spectra in ATR mode made on the bottom surface of OA AAO membranes (0.05 M, 0.3 M and 0.8 M). **c)** X over Al ratio for OA-0.3 (green), Sul-0.3 (blue) and Sel-0.3 (red) AAO membranes: top (circle), bottom (triangle) and section (square) surfaces.

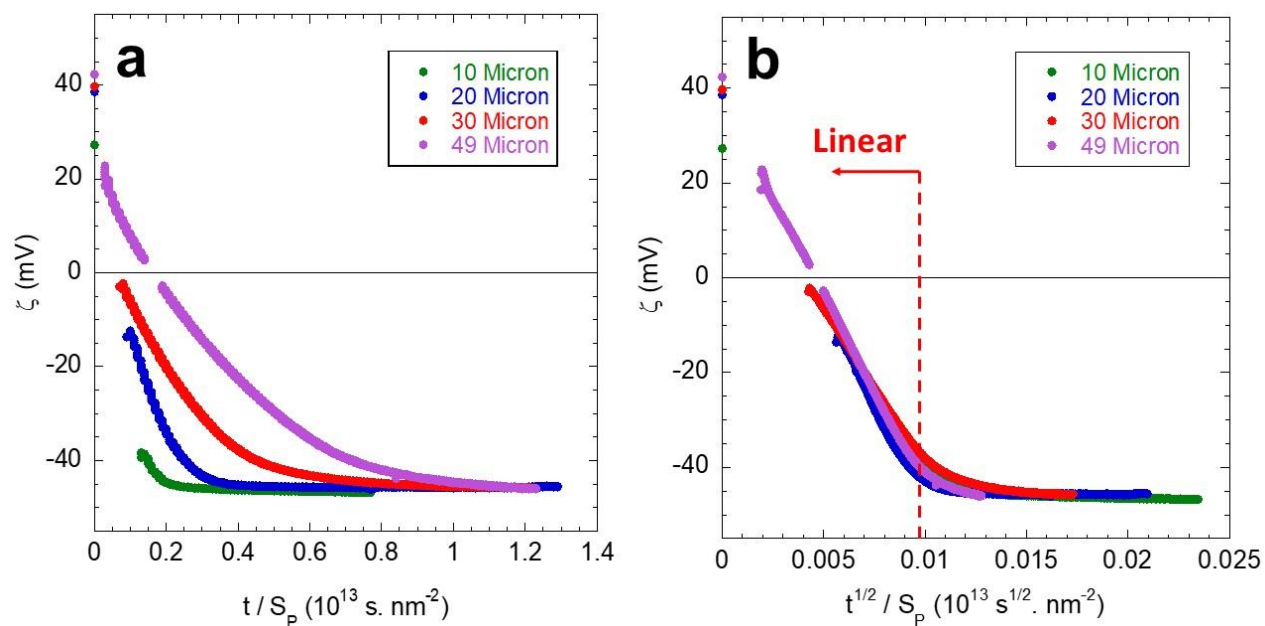


**Figure Appendix 3** The  $\zeta$ -potential data points of oxalic acid synthesized membranes (Figure 3-4 e) versus **a)** time normalized by the surface of the nanochannels and **b)** square root of the time normalized by the surface of the nanochannels. The linear segment of Figure b proves the domination of diffusion mechanism on the transfer of the PSS macromolecules inside the AAO nanochannels.

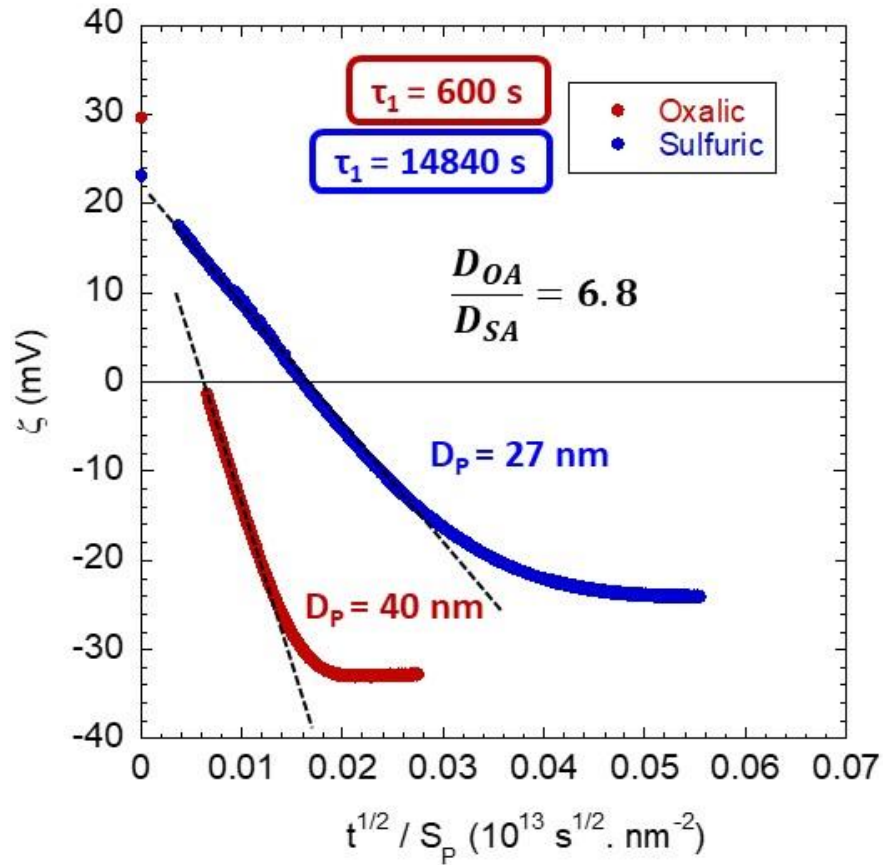


**Figure Appendix 4** The  $\zeta$ -potential data points of oxalic acid synthesized membranes (Figure 3-9 c) plotted versus square root of the time normalized by the surface of the nanochannels. From the ratio of the slopes of the linear segments, the ratio of the diffusion coefficients inside the nanochannels of oxalic acid synthesized membranes ( $D_{OA}$ ) to that inside the nanochannels of sulfuric acid synthesized membranes ( $D_{SA}$ ) is obtained.

## References

- [1] A. Santos, T. Kumeria, and D. Losic, “Nanoporous anodic aluminum oxide for chemical sensing and biosensors,” *TrAC Trends in Analytical Chemistry*, vol. 44, pp. 25–38, Mar. **2013**, doi: 10.1016/j.trac.2012.11.007.
- [2] B. Kang, U. Yeo, and K.-H. Yoo, “Anodized aluminum oxide-based capacitance sensors for the direct detection of DNA hybridization,” *Biosensors and Bioelectronics*, vol. 25, no. 7, pp. 1592–1596, Mar. **2010**, doi: 10.1016/j.bios.2009.11.017.
- [3] H.-J. Kang, D. J. Kim, S.-J. Park, J.-B. Yoo, and Y. S. Ryu, “Controlled drug release using nanoporous anodic aluminum oxide on stent,” *Thin Solid Films*, vol. 515, no. 12, pp. 5184–5187, Apr. **2007**, doi: 10.1016/j.tsf.2006.10.029.
- [4] D.-H. Kwak, J.-B. Yoo, and D. J. Kim, “Drug Release Behavior from Nanoporous Anodic Aluminum Oxide,” *J. Nanosci. Nanotech.*, vol. 10, no. 1, pp. 345–348, Jan. **2010**, doi: 10.1166/jnn.2010.1531.
- [5] K. Noh, K. S. Brammer, C. Choi, S. H. Kim, C. J. Frandsen, and S. Jin, “A New Nano-Platform for Drug Release via Nanotubular Aluminum Oxide,” *JBNB*, vol. 02, no. 03, pp. 226–233, **2011**, doi: 10.4236/jbnb.2011.23028.
- [6] C. Hong, T.-T. Tang, C.-Y. Hung, R.-P. Pan, and W. Fang, “Liquid crystal alignment in nanoporous anodic aluminum oxide layer for LCD panel applications,” *Nanotechnology*, vol. 21, no. 28, p. 285201, Jul. **2010**, doi: 10.1088/0957-4484/21/28/285201.
- [7] H. J. Fang *et al.*, “Anodic aluminum oxide–epoxy composite acoustic matching layers for ultrasonic transducer application,” *Ultrasonics*, vol. 70, pp. 29–33, Aug. **2016**, doi: 10.1016/j.ultras.2016.04.003.
- [8] M. Saeedikhani, M. Javidi, and A. Yazdani, “Anodizing of 2024-T3 aluminum alloy in sulfuric-boric-phosphoric acids and its corrosion behavior,” *Transactions of Nonferrous Metals Society of China*, vol. 23, no. 9, pp. 2551–2559, Sep. **2013**, doi: 10.1016/S1003-6326(13)62767-3.
- [9] A. Bai, C.-C. Hu, Y.-F. Yang, and C.-C. Lin, “Pore diameter control of anodic aluminum oxide with ordered array of nanopores,” *Electrochimica Acta*, vol. 53, no. 5, pp. 2258–2264, Jan. **2008**, doi: 10.1016/j.electacta.2007.09.039.

- [10] S. J. Garcia-Vergara, P. Skeldon, G. E. Thompson, and H. Habazaki, "Stress generated porosity in anodic alumina formed in sulphuric acid electrolyte," *Corrosion Science*, vol. 49, no. 10, pp. 3772–3782, Oct. **2007**, doi: 10.1016/j.corsci.2007.03.036.
- [11] O. Jessensky, F. Müller, and U. Gösele, "Self-organized formation of hexagonal pore arrays in anodic alumina," *Appl. Phys. Lett.*, vol. 72, no. 10, pp. 1173–1175, Mar. **1998**, doi: 10.1063/1.121004.
- [12] O. Nishinaga, T. Kikuchi, S. Natsui, and R. O. Suzuki, "Rapid fabrication of self-ordered porous alumina with 10-/sub-10-nm-scale nanostructures by selenic acid anodizing," *Sci Rep*, vol. 3, no. 1, p. 2748, Sep. **2013**, doi: 10.1038/srep02748.
- [13] T. Kikuchi, O. Nishinaga, S. Natsui, and R. O. Suzuki, "Self-Ordering Behavior of Anodic Porous Alumina via Selenic Acid Anodizing," *Electrochimica Acta*, vol. 137, pp. 728–735, Aug. **2014**, doi: 10.1016/j.electacta.2014.06.078.
- [14] S. Akiya, T. Kikuchi, S. Natsui, and R. O. Suzuki, "Optimum Exploration for the Self-Ordering of Anodic Porous Alumina Formed via Selenic Acid Anodizing," *J. Electrochem. Soc.*, vol. 162, no. 10, pp. E244–E250, **2015**, doi: 10.1149/2.0391510jes.
- [15] M. P. Proenca, C. T. Sousa, D. C. Leitao, J. Ventura, J. B. Sousa, and J. P. Araujo, "Nanopore formation and growth in phosphoric acid Al anodization," *Journal of Non-Crystalline Solids*, vol. 354, no. 47–51, pp. 5238–5240, Dec. **2008**, doi: 10.1016/j.jnoncrysol.2008.04.055.
- [16] S. Akiya, T. Kikuchi, S. Natsui, N. Sakaguchi, and R. O. Suzuki, "Self-ordered Porous Alumina Fabricated via Phosphonic Acid Anodizing," *Electrochimica Acta*, vol. 190, pp. 471–479, Feb. **2016**, doi: 10.1016/j.electacta.2015.12.162.
- [17] H. Masuda and K. Fukuda, "Ordered Metal Nanohole Arrays Made by a Two-Step Replication of Honeycomb Structures of Anodic Alumina," *Science*, vol. 268, no. 5216, pp. 1466–1468, Jun. **1995**, doi: 10.1126/science.268.5216.1466.
- [18] H. M. Hideki Masuda and M. S. Masahiro Satoh, "Fabrication of Gold Nanodot Array Using Anodic Porous Alumina as an Evaporation Mask," *Jpn. J. Appl. Phys.*, vol. 35, no. 1B, p. L126, Jan. **1996**, doi: 10.1143/JJAP.35.L126.
- [19] S.-K. Hwang, S.-H. Jeong, H.-Y. Hwang, O.-J. Lee, and K.-H. Lee, "Fabrication of highly ordered pore array in anodic aluminum oxide," *Korean J. Chem. Eng.*, vol. 19, no. 3, pp. 467–473, May **2002**, doi: 10.1007/BF02697158.

- [20] W. Lee, R. Ji, U. Gösele, and K. Nielsch, “Fast fabrication of long-range ordered porous alumina membranes by hard anodization,” *Nature Mater.*, vol. 5, no. 9, pp. 741–747, Sep. **2006**, doi: 10.1038/nmat1717.
- [21] A. Belwalkar, E. Grasing, W. Vangeertruyden, Z. Huang, and W. Misiolek, “Effect of processing parameters on pore structure and thickness of anodic aluminum oxide (AAO) tubular membranes,” *Journal of Membrane Science*, vol. 319, no. 1–2, pp. 192–198, Jul. **2008**, doi: 10.1016/j.memsci.2008.03.044.
- [22] W. J. Stępniewski and Z. Bojar, “Synthesis of anodic aluminum oxide (AAO) at relatively high temperatures. Study of the influence of anodization conditions on the alumina structural features,” *Surface and Coatings Technology*, vol. 206, no. 2–3, pp. 265–272, Oct. **2011**, doi: 10.1016/j.surfcoat.2011.07.020.
- [23] K. Chernyakova, B. Tzaneva, I. Vrublevsky, and V. Videkov, “Effect of Aluminum Anode Temperature on Growth Rate and Structure of Nanoporous Anodic Alumina,” *J. Electrochem. Soc.*, vol. 167, no. 10, p. 103506, Jan. **2020**, doi: 10.1149/1945-7111/ab9d65.
- [24] K. Nielsch, J. Choi, K. Schwirn, R. B. Wehrspohn, and U. Gösele, “Self-ordering Regimes of Porous Alumina: The 10 Porosity Rule,” *Nano Lett.*, vol. 2, no. 7, pp. 677–680, Jul. **2002**, doi: 10.1021/nl025537k.
- [25] W. J. Stępniewski, M. Norek, M. Michalska-Domańska, and Z. Bojar, “Ultra-small nanopores obtained by self-organized anodization of aluminum in oxalic acid at low voltages,” *Materials Letters*, vol. 111, pp. 20–23, Nov. **2013**, doi: 10.1016/j.matlet.2013.08.059.
- [26] X. Wang and G.-R. Han, “Fabrication and characterization of anodic aluminum oxide template,” *Microelectronic Engineering*, vol. 66, no. 1–4, pp. 166–170, Apr. **2003**, doi: 10.1016/S0167-9317(03)00042-X.
- [27] Y. Zhang, S. J. Son, and H. Ju, “Anodized aluminum oxide membranes of tunable porosity with platinum nanoscale-coating for photonic application,” *Current Applied Physics*, vol. 12, no. 6, pp. 1561–1565, Nov. **2012**, doi: 10.1016/j.cap.2012.04.036.
- [28] C. V. Manzano, D. Ramos, L. Pethö, G. Bürki, J. Michler, and L. Philippe, “Controlling the Color and Effective Refractive Index of Metal-Anodic Aluminum Oxide (AAO)–Al Nanostructures: Morphology of AAO,” *J. Phys. Chem. C*, vol. 122, no. 1, pp. 957–963, Jan. **2018**, doi: 10.1021/acs.jpcc.7b11131.
- [29] A. A. Noyan and K. S. Napolskii, “Birefringence in anodic aluminum oxide: an optical method for measuring porosity,” *Mater. Adv.*, vol. 3, no. 8, pp. 3642–3648, **2022**, doi: 10.1039/D2MA00111J.

- [30] V. A. Yakovlev, E. A. Vinogradov, N. N. Novikova, G. Mattei, and M. Delpiancke-Ogletree, “Infrared reflectivity spectra of thin porous aluminum oxide films,” *Phys. Status Solidi (c)*, vol. 6, no. 7, pp. 1697–1699, Jul. **2009**, doi: 10.1002/pssc.200881011.
- [31] X. Qin *et al.*, “Preparation and analysis of anodic aluminum oxide films with continuously tunable interpore distances,” *Applied Surface Science*, vol. 328, pp. 459–465, Feb. **2015**, doi: 10.1016/j.apsusc.2014.12.048.
- [32] M. A. Kashi, A. Ramazani, M. Raoufi, and A. Karimzadeh, “Self-ordering of anodic nanoporous alumina fabricated by accelerated mild anodization method,” *Thin Solid Films*, vol. 518, no. 23, pp. 6767–6772, Sep. **2010**, doi: 10.1016/j.tsf.2010.06.020.
- [33] H. Masuda, K. Yada, and A. Osaka, “Self-Ordering of Cell Configuration of Anodic Porous Alumina with Large-Size Pores in Phosphoric Acid Solution,” *Jpn. J. Appl. Phys.*, vol. 37, no. 11A, p. L1340, Nov. **1998**, doi: 10.1143/JJAP.37.L1340.
- [34] W. J. Stepniowski, D. Forbot, M. Norek, M. Michalska-Domańska, and A. Król, “The impact of viscosity of the electrolyte on the formation of nanoporous anodic aluminum oxide,” *Electrochimica Acta*, vol. 133, pp. 57–64, Jul. **2014**, doi: 10.1016/j.electacta.2014.04.039.
- [35] W. Lee and S.-J. Park, “Porous Anodic Aluminum Oxide: Anodization and Templated Synthesis of Functional Nanostructures,” *Chem. Rev.*, vol. 114, no. 15, pp. 7487–7556, Aug. **2014**, doi: 10.1021/cr500002z.
- [36] D. Losic and A. Santos, Eds., *Nanoporous Alumina: Fabrication, Structure, Properties and Applications*, vol. 219. in Springer Series in Materials Science, vol. 219. Cham: Springer International Publishing, **2015**. doi: 10.1007/978-3-319-20334-8.
- [37] G. D. Sulka, *Nanostructured Anodic Metal Oxides: Synthesis and Applications*. Elsevier, **2020**.
- [38] C. Cheng and A. H. W. Ngan, “Modelling and simulation of self-ordering in anodic porous alumina,” *Electrochimica Acta*, vol. 56, no. 27, pp. 9998–10008, Nov. **2011**, doi: 10.1016/j.electacta.2011.08.090.
- [39] L. Yi, L. Zhiyuan, H. Xing, L. Yisen, and C. Yi, “Investigation of intrinsic mechanisms of aluminium anodization processes by analyzing the current density,” *RSC Adv.*, vol. 2, no. 12, p. 5164, **2012**, doi: 10.1039/c2ra01050j.
- [40] X.-F. Zhu *et al.*, “Electronic currents and the formation of nanopores in porous anodic alumina,” *Nanotechnology*, vol. 20, no. 47, p. 475303, Nov. **2009**, doi: 10.1088/0957-4484/20/47/475303.

- [41] F. Li, L. Zhang, and R. M. Metzger, “On the Growth of Highly Ordered Pores in Anodized Aluminum Oxide,” *Chem. Mater.*, vol. 10, no. 9, pp. 2470–2480, Sep. **1998**, doi: 10.1021/cm980163a.
- [42] J. Siejka and C. Ortega, “An O18 Study of Field-Assisted Pore Formation in Compact Anodic Oxide Films on Aluminum,” **1977**.
- [43] P. Mishra and K. R. Hebert, “Self-organization of anodic aluminum oxide layers by a flow mechanism,” *Electrochimica Acta*, vol. 340, p. 135879, Apr. **2020**, doi: 10.1016/j.electacta.2020.135879.
- [44] X. Zhu *et al.*, “Oxygen evolution and porous anodic alumina formation,” *Materials Letters*, vol. 62, no. 24, pp. 4038–4040, Sep. **2008**, doi: 10.1016/j.matlet.2008.05.062.
- [45] M. Pashchanka and J. J. Schneider, “Self-Ordering Regimes of Porous Anodic Alumina Layers Formed in Highly Diluted Sulfuric Acid Electrolytes,” *J. Phys. Chem. C*, vol. 120, no. 27, pp. 14590–14596, Jul. **2016**, doi: 10.1021/acs.jpcc.5b11801.
- [46] M. Pashchanka and J. J. Schneider, “Formation of Porous Anodic Alumina under Unstable Electroconvection Flow Regimes: A Case Study of Tartaric Acid Electrolyte,” *J. Phys. Chem. C*, vol. 121, no. 42, pp. 23683–23692, Oct. **2017**, doi: 10.1021/acs.jpcc.7b06157.
- [47] C. Cherki and J. Siejka, “Study by Nuclear Microanalysis and O18 Tracer Techniques of the Oxygen Transport Processes and the Growth Laws for Porous Anodic Oxide Layers on Aluminum,” vol. 120, no. 6, **1973**.
- [48] J. E. Houser and K. R. Hebert, “The role of viscous flow of oxide in the growth of self-ordered porous anodic alumina films,” *Nature Mater*, vol. 8, no. 5, pp. 415–420, May **2009**, doi: 10.1038/nmat2423.
- [49] A. M. Brudzisz, D. Giziński, and W. J. Stępniewski, “Incorporation of Ions into Nanostructured Anodic Oxides—Mechanism and Functionalities,” *Molecules*, vol. 26, no. 21, p. 6378, Oct. **2021**, doi: 10.3390/molecules26216378.
- [50] J. Choi, Y. Luo, R. B. Wehrspohn, R. Hillebrand, J. Schilling, and U. Gösele, “Perfect two-dimensional porous alumina photonic crystals with duplex oxide layers,” *J. Appl. Phys.*, vol. 94, no. 8, p. 4757, **2003**, doi: 10.1063/1.1609033.
- [51] W. L. Xu, H. Chen, M. J. Zheng, G. Q. Ding, and W. Z. Shen, “Optical transmission spectra of ordered porous alumina membranes with different thicknesses and porosities,” *Optical Materials*, vol. 28, no. 10, pp. 1160–1165, Jul. **2006**, doi: 10.1016/j.optmat.2005.07.003.

- [52] I. Mínguez-Bacho, S. Rodríguez-López, A. Climent-Font, D. Fichou, M. Vázquez, and M. Hernández-Vélez, "Variation of the refractive index by means of sulfate anion incorporation into nanoporous anodic aluminum oxide films," *Microporous and Mesoporous Materials*, vol. 225, pp. 192–197, May **2016**, doi: 10.1016/j.micromeso.2015.12.011.
- [53] R. A. Mirzoev, A. D. Davydov, E. S. Zarubenko, S. I. Vystupov, and E. S. Pantelev, "Analytical 3D migration model of steady-state metal anodizing: the velocity fields and trajectories of inert tracers, metal and oxygen ions," *Electrochimica Acta*, vol. 218, pp. 74–83, Nov. **2016**, doi: 10.1016/j.electacta.2016.09.115.
- [54] R. A. Mirzoev, A. D. Davydov, S. I. Vystupov, E. S. Zarubenko, T. B. Kabanova, and A. V. Popkovich, "ANALYTICAL 3D MIGRATION MODEL OF STEADY-STATE METAL ANODIZING: THE VELOCITY FIELDS AND TRAJECTORIES OF MIGRATING TRACERS," *Electrochimica Acta*, vol. 243, pp. 270–281, Jul. **2017**, doi: 10.1016/j.electacta.2017.05.025.
- [55] D. H. Fan, G. Q. Ding, W. Z. Shen, and M. J. Zheng, "Anion impurities in porous alumina membranes: Existence and functionality," *Microporous and Mesoporous Materials*, vol. 100, no. 1–3, pp. 154–159, Mar. **2007**, doi: 10.1016/j.micromeso.2006.10.025.
- [56] P. Pendyala, M. S. Bobji, and G. Madras, "Evolution of Surface Roughness During Electropolishing," *Tribol Lett*, vol. 55, no. 1, pp. 93–101, Jul. **2014**, doi: 10.1007/s11249-014-0336-x.
- [57] W. Han and F. Fang, "Fundamental aspects and recent developments in electropolishing," *International Journal of Machine Tools and Manufacture*, vol. 139, pp. 1–23, Apr. **2019**, doi: 10.1016/j.ijmachtools.2019.01.001.
- [58] B. Krishna and R. Wuthrich, "Investigation of the Effect of Bath Ageing on Electropolishing Efficiency," *ECS Trans.*, vol. 97, no. 7, pp. 505–514, Jun. **2020**, doi: 10.1149/09707.0505ecst.
- [59] T. Yanagishita and H. Masuda, "High-Throughput Fabrication Process for Highly Ordered Through-Hole Porous Alumina Membranes Using Two-Layer Anodization," *Electrochimica Acta*, vol. 184, pp. 80–85, Dec. **2015**, doi: 10.1016/j.electacta.2015.10.019.
- [60] T. Yanagishita, A. Kato, and H. Masuda, "Preparation of ideally ordered through-hole anodic porous alumina membranes by two-layer anodization," *Jpn. J. Appl. Phys.*, vol. 56, no. 3, p. 035202, Mar. **2017**, doi: 10.7567/JJAP.56.035202.
- [61] Y. Zhao, M. Chen, Y. Zhang, T. Xu, and W. Liu, "A facile approach to formation of through-hole porous anodic aluminum oxide film," *Materials Letters*, vol. 59, no. 1, pp. 40–43, Jan. **2005**, doi: 10.1016/j.matlet.2004.09.018.

- [62] J. H. Yuan, W. Chen, R. J. Hui, Y. L. Hu, and X. H. Xia, "Mechanism of one-step voltage pulse detachment of porous anodic alumina membranes," *Electrochimica Acta*, vol. 51, no. 22, pp. 4589–4595, Jun. **2006**, doi: 10.1016/j.electacta.2005.12.044.
- [63] M. Iwai and T. Kikuchi, "Chemical stability of porous anodic aluminum oxide in both acidic and alkaline solutions," *Thin Solid Films*, vol. 771, p. 139784, Apr. **2023**, doi: 10.1016/j.tsf.2023.139784.
- [64] T. Kikuchi, Y. Suzuki, M. Iwai, and R. O. Suzuki, "Anodizing Aluminum and Its Alloys in Etidronic Acid to Enhance Their Corrosion Resistance in a Sodium Chloride Solution," *J. Electrochem. Soc.*, vol. 167, no. 12, p. 121502, Jan. **2020**, doi: 10.1149/1945-7111/abaa6b.
- [65] S. A. Naayi, A. I. Hassan, and E. T. Salim, "In Press, Accepted Manuscript – Note to users".
- [66] R. A. Youness, M. A. Taha, A. A. El-Kheshen, and M. Ibrahim, "Influence of the addition of carbonated hydroxyapatite and selenium dioxide on mechanical properties and in vitro bioactivity of borosilicate inert glass," *Ceramics International*, vol. 44, no. 17, pp. 20677–20685, Dec. 2018, doi: 10.1016/j.ceramint.2018.08.061.
- [67] D. Peak, R. G. Ford, and D. L. Sparks, "An in Situ ATR-FTIR Investigation of Sulfate Bonding Mechanisms on Goethite," *Journal of Colloid and Interface Science*, vol. 218, no. 1, pp. 289–299, Oct. **1999**, doi: 10.1006/jcis.1999.6405.
- [68] D. Zhang, H. Zhang, and Y. He, "In-situ thickness measurement of porous alumina by atomic force microscopy and the reflectance wavelength measurement from 400–1000 nm," *Microsc. Res. Tech.*, vol. 69, no. 4, pp. 267–270, Apr. **2006**, doi: 10.1002/jemt.20311.
- [69] D. C. Harris *et al.*, "Refractive index of infrared-transparent polycrystalline alumina," *Opt. Eng.*, vol. 56, no. 7, p. 077103, Jul. **2017**, doi: 10.1117/1.OE.56.7.077103.
- [70] S. G. Yang *et al.*, "Stability of anodic aluminum oxide membranes with nanopores," *Physics Letters A*, vol. 318, no. 4–5, pp. 440–444, Nov. **2003**, doi: 10.1016/j.physleta.2003.09.051.
- [71] K. S. Choudhari, P. Sudheendra, and N. K. Udayashankar, "Fabrication and high-temperature structural characterization study of porous anodic alumina membranes," *J Porous Mater*, vol. 19, no. 6, pp. 1053–1062, Dec. **2012**, doi: 10.1007/s10934-012-9568-z.
- [72] G. Rajeev, B. Prieto Simon, L. F. Marsal, and N. H. Voelcker, "Advances in Nanoporous Anodic Alumina-Based Biosensors to Detect Biomarkers of Clinical Significance: A Review," *Adv. Healthcare Mater.*, vol. 7, no. 5, p. 1700904, Mar. **2018**, doi: 10.1002/adhm.201700904.

- [73] I. Sadeghi, P. Kaner, and A. Asatekin, “Controlling and Expanding the Selectivity of Filtration Membranes,” *Chem. Mater.*, vol. 30, no. 21, pp. 7328–7354, Nov. **2018**, doi: 10.1021/acs.chemmater.8b03334.
- [74] C. T. Sousa, D. C. Leitao, M. P. Proenca, J. Ventura, A. M. Pereira, and J. P. Araujo, “Nanoporous alumina as templates for multifunctional applications,” *Applied Physics Reviews*, vol. 1, no. 3, p. 031102, Sep. **2014**, doi: 10.1063/1.4893546.
- [75] M. Szuwarzyński, L. Zaraska, G. D. Sulka, and S. Zapotoczny, “Pulsatile Releasing Platform of Nanocontainers Equipped with Thermally Responsive Polymeric Nanovalves,” *Chem. Mater.*, vol. 25, no. 3, pp. 514–520, Feb. **2013**, doi: 10.1021/cm303930y.
- [76] D. M. Dotzauer, J. Dai, L. Sun, and M. L. Bruening, “Catalytic Membranes Prepared Using Layer-by-Layer Adsorption of Polyelectrolyte/Metal Nanoparticle Films in Porous Supports,” *Nano Lett.*, vol. 6, no. 10, pp. 2268–2272, Oct. **2006**, doi: 10.1021/nl061700q.
- [77] P. Banerjee, I. Perez, L. Henn-Lecordier, S. B. Lee, and G. W. Rubloff, “Nanotubular metal–insulator–metal capacitor arrays for energy storage,” *NATURE NANOTECHNOLOGY*, vol. 4, **2009**.
- [78] A. Busnaina, K. Bakhtari, and J.-G. Park, *Handbook of Silicon Wafer Cleaning Technology*, 2nd ed. William Andrew, Applied Science Publishers, **2008**.
- [79] J. Lyklema, *Fundamentals of Interface and Colloid Science: Part II Solid-Fluid Interfaces*. London: Academic Press, **1995**.
- [80] M. Zembala, “Electrokinetics of heterogeneous interfaces,” *Advances in Colloid and Interface Science*, vol. 112, no. 1–3, pp. 59–92, Dec. **2004**, doi: 10.1016/j.cis.2004.08.001.
- [81] A. V. Delgado, F. González-Caballero, R. J. Hunter, L. K. Koopal, and J. Lyklema, “Measurement and interpretation of electrokinetic phenomena,” *Journal of Colloid and Interface Science*, vol. 309, no. 2, pp. 194–224, May 2007, doi: 10.1016/j.jcis.2006.12.075.
- [82] A. Ruiz-Clavijo, O. Caballero-Calero, and M. Martín-González, “Revisiting anodic alumina templates: from fabrication to applications,” *Nanoscale*, vol. 13, no. 4, pp. 2227–2265, **2021**, doi: 10.1039/D0NR07582E.
- [83] H. Masuda and K. Fukuda, “Ordered Metal Nanohole Arrays Made by a Two-Step Replication of Honeycomb Structures of Anodic Alumina,” *Science*, vol. 268, no. 5216, pp. 1466–1468, Jun. **1995**, doi: 10.1126/science.268.5216.1466.

- [84] A. Yaroshchuk and V. Ribitsch, "Role of Channel Wall Conductance in the Determination of  $\zeta$ -Potential from Electrokinetic Measurements," *Langmuir*, vol. 18, no. 6, pp. 2036–2038, Mar. **2002**, doi: 10.1021/la015557m.
- [85] B. J. Pedimonte *et al.*, "Morphological zeta-potential variation of nanoporous anodic alumina layers and cell adherence," *Acta Biomaterialia*, vol. 10, no. 2, pp. 968–974, Feb. **2014**, doi: 10.1016/j.actbio.2013.09.023.
- [86] A. Szymczyk, P. Fievet, B. Aoubiza, C. Simon, and J. Pagetti, "An application of the space charge model to the electrolyte conductivity inside a charged microporous membrane," *Journal of Membrane Science*, vol. 161, no. 1–2, pp. 275–285, Aug. **1999**, doi: 10.1016/S0376-7388(99)00118-0.
- [87] B. Winkler, "Modification of the surface characteristics of anodic alumina membranes using sol–gel precursor chemistry," *Journal of Membrane Science*, vol. 226, no. 1–2, pp. 75–84, Dec. **2003**, doi: 10.1016/j.memsci.2003.07.015.
- [88] A. Christoulaki, D. Lairez, E. Dubois, and N. Jouault, "Probing polyelectrolyte adsorption in charged nanochannels by streaming potential measurements," *ACS Macro Letters*, vol. 9, no. 6, pp. 794–798, **2020**.
- [89] J. Wang *et al.*, "Structural Engineering of the Barrier Oxide Layer of Nanoporous Anodic Alumina for Iontronic Sensing," *ACS Appl. Mater. Interfaces*, vol. 14, no. 18, pp. 21181–21197, May **2022**, doi: 10.1021/acsami.2c02369.
- [90] E. G. Kovaleva *et al.*, "Acid–Base Properties of Nanoconfined Volumes of Anodic Aluminum Oxide Pores by EPR of pH-Sensitive Spin Probes," *J. Phys. Chem. C*, vol. 120, no. 5, pp. 2703–2711, Feb. **2016**, doi: 10.1021/acs.jpcc.5b10241.
- [91] E. G. Kovaleva *et al.*, "Electrostatic properties of inner nanopore surfaces of anodic aluminum oxide membranes upon high temperature annealing revealed by EPR of pH-sensitive spin probes and labels," *Journal of Membrane Science*, vol. 604, p. 118084, Jun. **2020**, doi: 10.1016/j.memsci.2020.118084.
- [92] M. Kosmulski, "Isoelectric points and points of zero charge of metal (hydr)oxides: 50years after Parks' review," *Advances in Colloid and Interface Science*, vol. 238, pp. 1–61, Dec. **2016**, doi: 10.1016/j.cis.2016.10.005.
- [93] F. Borghi, V. Vyas, A. Podestà, and P. Milani, "Nanoscale Roughness and Morphology Affect the Isoelectric Point of Titania Surfaces," *PLoS ONE*, vol. 8, no. 7, p. e68655, Jul. **2013**, doi: 10.1371/journal.pone.0068655.

- [94] L. Saravanan and S. Subramanian, "Surface chemical studies on the competitive adsorption of poly(ethylene glycol) and ammonium poly(methacrylate) onto alumina," *Journal of Colloid and Interface Science*, vol. 284, no. 2, pp. 363–377, Apr. **2005**, doi: 10.1016/j.jcis.2004.08.188.
- [95] T. D. Pham *et al.*, "Adsorptive removal of ammonium ion from aqueous solution using surfactant-modified alumina," *Environ. Chem.*, vol. 14, no. 5, p. 327, **2017**, doi: 10.1071/EN17102.
- [96] M. Baca, X. Carrier, and J. Blanchard, "Confinement in Nanopores at the Oxide/Water Interface: Modification of Alumina Adsorption Properties," *Chem. Eur. J.*, vol. 14, no. 20, pp. 6142–6148, Jul. **2008**, doi: 10.1002/chem.200800032.
- [97] G. Lefèvre, M. Duc, P. Lepeut, R. Caplain, and M. Fédoroff, "Hydration of  $\gamma$ -Alumina in Water and Its Effects on Surface Reactivity," *Langmuir*, vol. 18, no. 20, pp. 7530–7537, Oct. **2002**, doi: 10.1021/la025651i.
- [98] M. Engel, B. Stühn, J. J. Schneider, T. Cornelius, and M. Naumann, "Small-angle X-ray scattering (SAXS) off parallel, cylindrical, well-defined nanopores: from random pore distribution to highly ordered samples," *Appl. Phys. A*, vol. 97, no. 1, pp. 99–108, Oct. **2009**, doi: 10.1007/s00339-009-5346-4.
- [99] M. L. Machesky and P. F. Jacobs, "Titration calorimetry of aqueous alumina suspensions part II. Discussion of enthalpy changes with pH and ionic strength," *Colloids and Surfaces*, vol. 53, no. 2, pp. 315–328, Jan. **1991**, doi: 10.1016/0166-6622(91)80144-D.
- [100] H. Hashimoto, K. Yazawa, H. Asoh, and S. Ono, "NMR Spectroscopic Analysis of the Local Structure of Porous-Type Amorphous Alumina Prepared by Anodization," *J. Phys. Chem. C*, vol. 121, no. 22, pp. 12300–12307, Jun. **2017**, doi: 10.1021/acs.jpcc.7b03629.
- [101] T. Iijima *et al.*, "Structure of Duplex Oxide Layer in Porous Alumina Studied by  $^{27}\text{Al}$  MAS and MQMAS NMR," *Chem. Lett.*, vol. 34, no. 9, pp. 1286–1287, Sep. **2005**, doi: 10.1246/cl.2005.1286.
- [102] T. C. Prathna and A. M. Raichur, "Fluoride Removal from Aqueous Solutions Using Poly(Styrene Sulfonate)/Nanoalumina Multilayer Thin Films," *Global Challenges*, vol. 2, no. 2, p. 1700064, Feb. **2018**, doi: 10.1002/gch2.201700064.
- [103] I. Morosanu, C. Paduraru, F. Bucatariu, D. Fighir, M. Mihai, and C. Teodosiu, "Shaping polyelectrolyte composites for heavy metals adsorption from wastewater: Experimental assessment and equilibrium studies," *Journal of Environmental Management*, vol. 321, p. 115999, Nov. **2022**, doi: 10.1016/j.jenvman.2022.115999.

- [104] N. I. Kovtyukhova, B. R. Martin, J. K. N. Mbindyo, T. E. Mallouk, M. Cabassi, and T. S. Mayer, “Layer-by-layer self-assembly strategy for template synthesis of nanoscale devices,” *Materials Science and Engineering: C*, vol. 19, no. 1–2, pp. 255–262, Jan. **2002**, doi: 10.1016/S0928-4931(01)00395-2.
- [105] P. Kapruwan, J. Ferré-Borrull, and L. F. Marsal, “Nanoporous Anodic Alumina Platforms for Drug Delivery Applications: Recent Advances and Perspective,” *Adv. Mater. Interfaces*, vol. 7, no. 22, p. 2001133, Nov. **2020**, doi: 10.1002/admi.202001133.
- [106] N. G. Hoogeveen, M. A. C. Stuart, and G. J. Fleer, “Polyelectrolyte Adsorption on Oxides: Kinetics and adsorbed amounts. J. Colloids and interfaces science, **1996**
- [107] N. G. Hoogeveen, M. A. C. Stuart, and G. J. Fleer, “Polyelectrolyte Adsorption on Oxides: II. Reversibility and Exchange”. J. Colloids and interfaces science, **1996**
- [108] P. M. Claesson, O. E. H. Paulson, E. Blomberg, and N. L. Burns, “Surface properties of poly(ethylene imine)-coated mica surfaces—salt and pH effects,” *Colloids and Surfaces A: Physicochemical and Engineering Aspects*, vol. 123–124, pp. 341–353, May **1997**, doi: 10.1016/S0927-7757(96)03807-1.
- [109] M. Morga and Z. Adamczyk, “Monolayers of cationic polyelectrolytes on mica – Electrokinetic studies,” *Journal of Colloid and Interface Science*, vol. 407, pp. 196–204, Oct. **2013**, doi: 10.1016/j.jcis.2013.05.069.
- [110] Z. Adamczyk, M. Zembala, P. Warszyński, and B. Jachimska, “Characterization of Polyelectrolyte Multilayers by the Streaming Potential Method,” *Langmuir*, vol. 20, no. 24, pp. 10517–10525, Nov. **2004**, doi: 10.1021/la040064d.
- [111] Z. Adamczyk, M. Zembala, and A. Michna, “Polyelectrolyte adsorption layers studied by streaming potential and particle deposition,” *Journal of Colloid and Interface Science*, vol. 303, no. 2, pp. 353–364, Nov. **2006**, doi: 10.1016/j.jcis.2006.07.083.
- [112] E. Blomberg, E. Poptoshev, and F. Caruso, “Surface Interactions during Polyelectrolyte Multilayer Build-Up. 2. The Effect of Ionic Strength on the Structure of Preformed Multilayers,” *Langmuir*, vol. 22, no. 9, pp. 4153–4157, Apr. **2006**, doi: 10.1021/la052946y.
- [113] K. Büscher, K. Graf, H. Ahrens, and C. A. Helm, “Influence of Adsorption Conditions on the Structure of Polyelectrolyte Multilayers,” *Langmuir*, vol. 18, no. 9, pp. 3585–3591, Apr. **2002**, doi: 10.1021/la011682m.

- [114] T. D. Pham, M. Kobayashi, and Y. Adachi, “Adsorption of Polyanion onto Large Alpha Alumina Beads with Variably Charged Surface,” *Advances in Physical Chemistry*, vol. **2014**, pp. 1–9, Dec. 2014, doi: 10.1155/2014/460942.
- [115] T. Sennerfors, D. Solberg, and F. Tiberg, “Adsorption of Polyelectrolyte–Nanoparticle Systems on Silica: Influence of Ionic Strength,” *Journal of Colloid and Interface Science*, vol. 254, no. 2, pp. 222–226, Oct. **2002**, doi: 10.1006/jcis.2002.8582.
- [116] S.-C. Liufu, H.-N. Xiao, and Y.-P. Li, “Adsorption of cationic polyelectrolyte at the solid/liquid interface and dispersion of nanosized silica in water,” *Journal of Colloid and Interface Science*, vol. 285, no. 1, pp. 33–40, May 2005, doi: 10.1016/j.jcis.2004.11.012.
- [117] T. H. Dao *et al.*, “Adsorption Behavior of Polyelectrolyte onto Alumina and Application in Ciprofloxacin Removal,” *Polymers*, vol. 12, no. 7, p. 1554, Jul. **2020**, doi: 10.3390/polym12071554.
- [118] J. Martín and C. Mijangos, “Tailored Polymer-Based Nanofibers and Nanotubes by Means of Different Infiltration Methods into Alumina Nanopores,” *Langmuir*, vol. 25, no. 2, pp. 1181–1187, Jan. **2009**, doi: 10.1021/la803127w.
- [119] J. Martín, J. Maiz, J. Sacristan, and C. Mijangos, “Tailored polymer-based nanorods and nanotubes by ‘template synthesis’: From preparation to applications,” *Polymer*, vol. 53, no. 6, pp. 1149–1166, Mar. **2012**, doi: 10.1016/j.polymer.2012.01.028.
- [120] Y. Cho, W. Lee, Y. K. Jhon, J. Genzer, and K. Char, “Polymer Nanotubules Obtained by Layer-by-Layer Deposition within AAO-Membrane Templates with Sub-100-nm Pore Diameters,” *Small*, vol. 6, no. 23, pp. 2683–2689, Dec. **2010**, doi: 10.1002/sml.201001212.
- [121] C. J. Roy, C. Dupont-Gillain, S. Demoustier-Champagne, A. M. Jonas, and J. Landoulsi, “Growth Mechanism of Confined Polyelectrolyte Multilayers in Nanoporous Templates,” *Langmuir*, vol. 26, no. 5, pp. 3350–3355, Mar. **2010**, doi: 10.1021/la903121e.
- [122] Y. Cho, J. Lim, and K. Char, “Layer-by-layer assembled stimuli-responsive nanoporous membranes,” *Soft Matter*, vol. 8, no. 40, p. 10271, **2012**, doi: 10.1039/c2sm26562a.
- [123] T. D. Lazzara, K. H. A. Lau, W. Knoll, A. Janshoff, and C. Steinem, “Macromolecular shape and interactions in layer-by-layer assemblies within cylindrical nanopores,” *Beilstein J. Nanotechnol.*, vol. 3, pp. 475–484, Jun. **2012**, doi: 10.3762/bjnano.3.54.
- [124] M. Raoufi, D. Tranchida, and H. Schönherr, “Pushing the Size Limits in the Replication of Nanopores in Anodized Aluminum Oxide via the Layer-by-Layer Deposition of Polyelectrolytes,” *Langmuir*, vol. 28, no. 26, pp. 10091–10096, Jul. **2012**, doi: 10.1021/la3017062.

- [125] Y. Cho, C. Lee, and J. Hong, “Pore size effect on the formation of polymer nanotubular structures within nanoporous templates,” *Colloids and Surfaces A: Physicochemical and Engineering Aspects*, vol. 443, pp. 195–200, Feb. **2014**, doi: 10.1016/j.colsurfa.2013.11.013.
- [126] F. S. H. Krismastuti, H. Bayat, N. H. Voelcker, and H. Schönherr, “Real Time Monitoring of Layer-by-Layer Polyelectrolyte Deposition and Bacterial Enzyme Detection in Nanoporous Anodized Aluminum Oxide,” *Anal. Chem.*, vol. 87, no. 7, pp. 3856–3863, Apr. **2015**, doi: 10.1021/ac504626m.
- [127] M. Muthukumar, “Adsorption of a polyelectrolyte chain to a charged surface,” *The Journal of Chemical Physics*, vol. 86, no. 12, pp. 7230–7235, Jun. **1987**, doi: 10.1063/1.452763.
- [128] M. A. G. Dahlgren, “Effect of Counterion Valency and Ionic Strength on Polyelectrolyte Adsorption,” *Langmuir*, vol. 10, no. 5, pp. 1580–1583, May **1994**, doi: 10.1021/la00017a042.
- [129] C. W. Frank, Ed., *Organic Thin Films: Structure and Applications*, vol. 695. in ACS Symposium Series, vol. 695. Washington, DC: American Chemical Society, **1998**. doi: 10.1021/bk-1998-0695.
- [130] S. T. Dubas and J. B. Schlenoff, “Factors Controlling the Growth of Polyelectrolyte Multilayers,” *Macromolecules*, vol. 32, no. 24, pp. 8153–8160, Nov. **1999**, doi: 10.1021/ma981927a.
- [131] H. G. M. Van de Steeg, M. A. Cohen Stuart, A. De Keizer, and B. H. Bijsterbosch, “Polyelectrolyte adsorption: a subtle balance of forces,” *Langmuir*, vol. 8, no. 10, pp. 2538–2546, Oct. **1992**, doi: 10.1021/la00046a030.
- [132] J. F. L. Duval, D. Küttner, M. Nitschke, C. Werner, and R. Zimmermann, “Interrelations between charging, structure and electrokinetics of nanometric polyelectrolyte films,” *Journal of Colloid and Interface Science*, vol. 362, no. 2, pp. 439–449, Oct. **2011**, doi: 10.1016/j.jcis.2011.06.063.
- [133] R. Zimmermann, S. S. Dukhin, C. Werner, and J. F. L. Duval, “On the use of electrokinetics for unraveling charging and structure of soft planar polymer films,” *Current Opinion in Colloid & Interface Science*, vol. 18, no. 2, pp. 83–92, Apr. **2013**, doi: 10.1016/j.cocis.2013.02.001.
- [134] R. Zimmermann, C. Werner, and J. Duval, “Recent Progress and Perspectives in the Electrokinetic Characterization of Polyelectrolyte Films,” *Polymers*, vol. 8, no. 1, p. 7, Dec. **2015**, doi: 10.3390/polym8010007.
- [135] J. F. L. Duval and H. P. van Leeuwen, “Electrokinetics of Diffuse Soft Interfaces. 1. Limit of Low Donnan Potentials,” *Langmuir*, vol. 20, no. 23, pp. 10324–10336, Nov. **2004**, doi: 10.1021/la0400508.

- [136] J. F. L. Duval, “Electrokinetics of Diffuse Soft Interfaces. 2. Analysis Based on the Nonlinear Poisson–Boltzmann Equation,” *Langmuir*, vol. 21, no. 8, pp. 3247–3258, Apr. **2005**, doi: 10.1021/la040108i.
- [137] S. Chanda, S. Sinha, and S. Das, “Streaming potential and electroviscous effects in soft nanochannels: towards designing more efficient nanofluidic electrochemomechanical energy converters,” *Soft Matter*, vol. 10, no. 38, pp. 7558–7568, Jul. **2014**, doi: 10.1039/C4SM01490A.
- [138] G. Chen and S. Das, “Streaming potential and electroviscous effects in soft nanochannels beyond Debye–Hückel linearization,” *Journal of Colloid and Interface Science*, vol. 445, pp. 357–363, May **2015**, doi: 10.1016/j.jcis.2014.12.088.
- [139] N. Lesniewska, A. Beaussart, and J. F. L. Duval, “Conditional existence of Donnan potential in soft particles and surfaces: dependence on steric effects mediated by electrolyte ions and structural charges,” *Journal of Molecular Liquids*, p. 122643, Jul. **2023**, doi: 10.1016/j.molliq.2023.122643.
- [140] F. von Goeler and M. Muthukumar, “Adsorption of polyelectrolytes onto curved surfaces,” *The Journal of Chemical Physics*, vol. 100, no. 10, pp. 7796–7803, May **1994**, doi: 10.1063/1.466822.
- [141] A. G. Cherstvy and R. G. Winkler, “Polyelectrolyte adsorption onto oppositely charged interfaces: unified approach for plane, cylinder, and sphere,” *Phys. Chem. Chem. Phys.*, vol. 13, no. 24, p. 11686, **2011**, doi: 10.1039/c1cp20749k.
- [142] Y. G. Mishael, P. L. Dubin, R. de Vries, and A. B. Kayitmazer, “Effect of Pore Size on Adsorption of a Polyelectrolyte to Porous Glass,” *Langmuir*, vol. 23, no. 5, pp. 2510–2516, Feb. **2007**, doi: 10.1021/la062314r.
- [143] I. Zamrik, H. Bayat, Q. Alhusaini, M. Raoufi, and H. Schönherr, “In Situ Study of Layer-by-Layer Polyelectrolyte Deposition in Nanopores of Anodic Aluminum Oxide by Reflectometric Interference Spectroscopy,” *Langmuir*, vol. 36, no. 8, pp. 1907–1915, Mar. **2020**, doi: 10.1021/acs.langmuir.9b03769.
- [144] H. Alem, F. Blondeau, K. Glinel, S. Demoustier-Champagne, and A. M. Jonas, “Layer-by-Layer Assembly of Polyelectrolytes in Nanopores,” *Macromolecules*, vol. 40, no. 9, pp. 3366–3372, May **2007**, doi: 10.1021/ma0703251.
- [145] J. Li and D. Li, “Polyelectrolyte adsorption in single small nanochannel by layer-by-layer method,” *Journal of Colloid and Interface Science*, vol. 561, pp. 1–10, Mar. 2020, doi: 10.1016/j.jcis.2019.11.116.

- [146] R. Zimmermann *et al.*, “Electrokinetics as an alternative to neutron reflectivity for evaluation of segment density distribution in PEO brushes,” *Soft Matter*, vol. 10, no. 39, pp. 7804–7809, Aug. **2014**, doi: 10.1039/C4SM01315H.
- [147] M. Drifford and J.-P. Dalbiez, “Effect of salt on sodium polystyrene sulfonate measured by light scattering,” *Biopolymers*, vol. 24, no. 8, pp. 1501–1514, Aug. **1985**, doi: 10.1002/bip.360240807.
- [148] V. Degiorgio, F. Mantegazza, and R. Piazza, “Transient Electric Birefringence Measurement of the Persistence Length of Sodium Polystyrene Sulfonate,” *Europhys. Lett.*, vol. 15, no. 1, pp. 75–80, May **1991**, doi: 10.1209/0295-5075/15/1/013.
- [149] J. Yashiro and T. Norisuye, “Excluded-volume effects on the chain dimensions and transport coefficients of sodium poly(styrene sulfonate) in aqueous sodium chloride,” *J. Polym. Sci. B Polym. Phys.*, vol. 40, no. 23, pp. 2728–2735, Dec. **2002**, doi: 10.1002/polb.10324.
- [150] Q. Chang, *Colloid and Interface Chemistry for Water Quality Control*. Elsevier Science, 2016. Accessed: Jul. 20, **2023**. [Online]. Available: <http://univ.scholarvox.com/catalog/book/docid/88833309>
- [151] E. Seyrek, J. Hierrezuelo, A. Sadeghpour, I. Szilagy, and M. Borkovec, “Molecular mass dependence of adsorbed amount and hydrodynamic thickness of polyelectrolyte layers,” *Phys. Chem. Chem. Phys.*, vol. 13, no. 28, p. 12716, **2011**, doi: 10.1039/c1cp20654k.
- [152] M. Raposo, L. H. C. Mattoso, and O. N. Oliveira, “Adsorption isotherms of poly(o-methoxyaniline),” *Thin Solid Films*, vol. 327–329, pp. 739–742, Aug. **1998**, doi: 10.1016/S0040-6090(98)00754-8.
- [153] C. F. Narambuena, D. M. Beltramo, and E. P. M. Leiva, “Polyelectrolyte Adsorption on a Charged Surface. A Study by Monte Carlo Simulations,” *Macromolecules*, vol. 40, no. 20, pp. 7336–7342, Oct. **2007**, doi: 10.1021/ma0705568.
- [154] S. A. Sukhishvili and S. Granick, “Polyelectrolyte adsorption onto an initially-bare solid surface of opposite electrical charge,” *The Journal of Chemical Physics*, vol. 109, no. 16, pp. 6861–6868, Oct. **1998**, doi: 10.1063/1.477253.
- [155] Christoulaki, Anastasia. Experimental approaches in studying polyelectrolytes inside a porous matrix: the case of nanoporous alumina membranes. Doctoral Dissertation. Sorbonne Université, **2018**.